Seismic Oceanography

A New Tool to Characterize Physical Oceanographic Structures and Processes

Grant George Buffett

Estructura i Dinàmica de la Terra
Institut de Ciències de la Terra "Jaume Almera"
Consejo Superior de Investigaciones Científicas (CSIC)

Departament de Geodinàmica i Geofísica
Universitat de Barcelona

Seismic Oceanography

A New Tool to Characterize Physical Oceanographic Structures and Processes

Memòria presentada per Grant George Buffett per optar al Títol de Doctor en Geologia

Aquesta tesi ha estat realitzada dins el Programa de Doctorat Exploració, Anàlisi i modelització de conques i sistemes orogènics bienni 2006-2008, de la Universitat de Barcelona.

Director:

Prof. Dr. Ramón Carbonell i Bertrán

Tutor:

Dra. Pilar Queralt i Capdevila

Grant George Buffett

Barcelona, Novembre de 2010

PART I.

Research Contributions to Seismic Oceanography

CHAPTER 1

Seismic Reflection Along the Path of the Mediterranean Undercurrent

Out there, just at the edge of the where-we-couldn't-see, big waves were thundering in, dimly seen white shapes that boomed and shouted and threw great handfuls of froth at us. Together we laughed for pure joy - he a baby meeting for the first time the wild tumult of Oceanus, I with the salt of half a lifetime of sea love in me. But I think we felt the same spine-tingling response to the vast, roaring ocean and the wild night around us.

-- Rachel Carson

Continental Shelf Research 29 (2009) 1848–1860

Contents lists available at ScienceDirect

Continental Shelf Research

journal homepage: www.elsevier.com/locate/csr

Seismic reflection along the path of the Mediterranean Undercurrent

G.G. Buffett [a,*], B. Biescas [b], J.L. Pelegrí [c], F. Machín [c], V. Sallarès [b], R. Carbonell [a], D. Klaeschen [d], R. Hobbs [e]

[a] Institut de Ciències de la Terra "Jaume Almera", C. Lluís Solé i Sabarís s/n, 08028 Barcelona, Spain
[b] Unitat de Tecnología Marina, CSIC, Passeig Marítim de la Barceloneta 37-49, 08003 Barcelona, Spain
[c] Institut de Ciències del Mar, CSIC, Passeig Marítim de la Barceloneta 37-49, 08003 Barcelona, Spain
[d] Leibniz-Institute of Marine Sciences, IFM-GEOMAR, Duesternbrooker Weg 20, D-24105 Kiel, Germany
[e] Department of Earth Sciences, Durham University, Durham, DH1 3LE, UK

ARTICLE INFO

Article history:
Received 31 October 2008
Received in revised form
25 May 2009
Accepted 29 May 2009
Available online 10 July 2009

Keywords:
Seismic oceanography
Mediterranean Undercurrent
Thermohaline fine structure
Mixing
Entrainment
Temperature
Salinity
Amplitude

ABSTRACT

Seismic reflection profiling is applied to the study of large scale physical oceanographic processes in the Gulf of Cádiz and western Iberian coast, coinciding with the path of the Mediterranean Undercurrent. The multi-channel seismic reflection method provides clear images of thermohaline fine structure with a horizontal resolution approximately two orders of magnitude higher than CTD casting. The seismic data are compared with co-located historical oceanographic data. Three seismic reflectivity zones are identified: North Atlantic Central Water, Mediterranean Water and North Atlantic Deep Water. Seismic evidence for the path of the Mediterranean Undercurrent is found in the near-slope reflectivity patterns, with rising reflectors between about 500 and 1500 m. However, the core of the undercurrent is largely transparent. Seismic images show that central and, particularly, intermediate Mediterranean Waters have fine structure coherent over horizontal distances of several tens of kilometers. However, the intensity of the reflectors, and their horizontal coherence, decreases downstream. This change in seismic reflectivity is probably the result of diminished vertical thermohaline contrasts between adjacent water masses, so that double-diffusion processes become unable to sustain temperature and salinity staircases. Comparison of root-mean-square seismic amplitudes with temperature and salinity differences between the Mediterranean Undercurrent and the overlying central waters suggests a causal relationship between observed thermohaline fine structure and true seismic amplitudes. We estimate that, within this intermediate water stratum, impedance contrasts are mainly controlled by sound speed contrasts (a factor between 3.5 and 10 times larger than density contrasts), which are mainly controlled by temperature contrasts (a factor between 1.5 and 5 times larger than salinity contrasts).

1. Introduction

Seismic reflection profiling is unique in its application to oceanography because of its method of implementation. Its low acoustic frequency, yet high level of lateral sampling allows oceanographers to create a quasi 'snapshot' of the ocean to visualize rapid changes in density and/or sound speed, which results in the identification of constant-property surfaces and their coherence over large horizontal distances. The multi-channel seismic reflection method (MCS) has been shown to be well suited to analyze the nature of thermohaline fine structure for many processes, from internal waves to frontal regions, with a lateral resolution of approximately two orders of magnitude greater than conventional oceanographic data (Ruddick, 2003; Thorpe, 2005).

Although acoustic probing of the ocean in various ways has been commonplace for decades, the first applications of seismic reflection profiling to the ocean were done by Gonella and Michon (1988) and Phillips and Dean (1991). These works, followed by the influential work of Holbrook et al. (2003) and subsequent studies (Biescas et al., 2008; Holbrook and Fer, 2005; Nakamura et al., 2006; Nandi et al., 2004; Páramo and Holbrook, 2005; Tsuji et al., 2005; Wood et al., 2008), have refined the seismic reflection 'common mid-point' (CMP) method to remotely image the ocean on a large scale—to full ocean depths and horizontally on the order of hundreds of kilometers.

Mediterranean Water (MW) enters the Atlantic Ocean through the Strait of Gibraltar as a result of the overflow of dense, saline water from the Mediterranean Sea, in the so-called Mediterranean Undercurrent (MU) (Bower et al., 2002). Guided by buoyancy and seafloor bathymetry the MU cascades down into the Gulf of Cádiz and mixes with North Atlantic Central Water (NACW) (Johnson et al., 1994) until it equilibrates at depths between 500 and 1500 m (Richardson et al., 2000), confined between the NACW and

* Corresponding author. Tel.: +34 93 409 5410; fax: +34 93 411 0012.
E-mail addresses: gbuffett@ija.csic.es, gbuffett@gmail.com (G.G. Buffett).

0278-4343/$ - see front matter © 2009 Elsevier Ltd. All rights reserved.
doi:10.1016/j.csr.2009.05.017

the North Atlantic Deep Water (NADW). Due to the Coriolis effect, the MU flows attached to the western continental slope of Iberia (Ambar et al., 1999) all the way into the Bay of Biscay and along the Porcupine Banks. Ochoa and Bray (1991) applied inverse methods to several sections in the Gulf of Cádiz to determine the existence of intense two-way mixing and one-way entrainment. Mixing, however, does not stop there because MW is progressively diluted along its path (Iorga and Lozier, 1999).

Near the Strait of Gibraltar the MU has a high thermohaline contrast and mixing may result from shear mixing (Price et al., 1993), while further downstream mixing may be the result of double-diffusive processes (Ruddick, 1992; Schmitt, 1994). The background upper-thermocline NACW becomes layered as a result of double-diffusion salt-fingering (St. Laurent and Schmitt, 1999). The MU intrusion causes salt fingering to be enhanced at the base of the MW, especially in the form of lateral intrusions (Ruddick, 1992; Ruddick and Kerr, 2003). MU intrusions also bring about the possibility of a diffusive regime on top of the MW intrusion (Ruddick and Gargett, 2003; Schmitt, 1994). We expect that these processes act all together and with different intensities resulting in a variety of thermohaline structures that change along the MU path.

Here we analyze seismic data for several normal-to-shore sections situated along the path of the MU, in order to investigate how inner-ocean reflectors evolve with distance from the source of MW, in the Strait of Gibraltar. These sections are examined in combination with historical, co-located CTD data, to appreciate how changes in these reflectors may respond to progressive mixing of MW in the North Atlantic Ocean.

2. Methodology

Since Obukhov (1941) there have been numerous treatises on acoustic methods to measure ocean fluid dynamic properties (Batchelor, 1957; Brandt, 1975; Chernov, 1957; Goodman, 1990; Munk and Garrett, 1973; Ottersten, 1969; Tatarski, 1971). Brandt (1975) studied high-frequency sound scattering from density variations of a turbulent saline jet in the laboratory. He concluded that the observed scattering was a result of acoustic impedance fluctuations produced by the jet and hence, that acoustic imaging techniques could be used to study oceanic diffusion processes and thermohaline structures. Orr and Hess (1978) acquired a joint physical oceanography/multifrequency (high-frequency) acoustic backscatter dataset. They observed that the intensity of back scatter was higher where the temperature gradient was maximum. They therefore suggested that oceanic microstructure played a role. Following this work, Haury et al. (1983) provided further constraints on the relationship between oceanic microstructure and acoustic backscatter. By combining the methods of Orr and Hess with plankton measurement constraints, they were able to produce an acoustic snapshot of an ostensibly breaking internal wave, thereby identifying thermohaline fine structure as the source of the backscatter. Munk and Wunsch (1979) first used travel-time ocean acoustic tomography by adapting a technique used in seismology to image the interior of the earth to represent very large scale ocean structures.

2.1. Seismic acquisition

The seismic acquisition survey was carried out in August and September 1993 to study the Iberian–Atlantic Margin (IAM) tectonic plate boundary (González et al., 1996). It proceeded by towing an impulsive source and a streamer (a cable filled with hydrophones), which recorded both signal and noise. The survey design and acquisition parameters were customized to the study of deep crustal structures. Nonetheless, the high energy source and narrow receiver spacing provides a rich seismic oceanography dataset (Fig. 1). In this work we have analyzed four seismic profiles, chosen to intersect perpendicularly with the known path of the MU (Bower et al., 2002; Richardson et al., 2000; Serra and Ambar, 2002) at different distances from its origin, in the Gibraltar Strait. The first profile is located nearly 400 km west of the Strait of Gibraltar while the distance between adjacent transects is about 200 km.

Source generated seismic waves travel through the water column. Acoustic impedance boundaries defined by varying density and sound speed modify the transmission to reflection ratio. As a result, the changes in density and sound speed partially backscatter propagating acoustic energy. The imaging procedure (Sheriff and Geldart, 1982; Yilmaz, 1987), takes advantage of the redundancy of sources and receivers to produce a continuous image of the subsurface and to attenuate random noise. In this method, instead of a single source and receiver, there are many sequentially fired sources and an array of receivers at regular intervals with varying source–receiver offsets.

In terms of imaging the solid earth, a seismic reflection profile is effectively a 'snap-shot' in time (due to the enormous time involved in geological processes). However, in application to physical oceanography, the seismic section is skewed in time due to the dynamic nature of ocean current velocities, which circulate in a time comparable to seismic data acquisition resulting in a picture of a progressively changing ocean. Recent seismic studies have shown that subtle thermohaline fine structure changes can occur in as little as 3 h (Géli and Cosquer, in preparation). Detailed acquisition parameters are summarized in Table 1.

Vertical resolution is much lower than the resolution available in oceanographic in situ probing (e.g. CTD) and is determined by the frequency content of the source, how sound is filtered by the water column and, ultimately, by what frequency bandwidth is recorded. Widess (1973) defined a one-quarter wavelength relationship for seismic data, whereby the smallest resolvable interface is expressed as one-quarter of the dominant seismic wavelength. Therefore, given a dominant frequency of 50 Hz, structures no smaller than about 7.5 m are resolvable. In practice however, one-quarter wavelength resolution is not obtainable due to the thickness and sharpness of the reflecting interface. Thus, we can confidently image interfaces of only about one-half the dominant frequency, or 15 m for a 50 Hz dominant frequency. As a result, although scattering and reflection of acoustic waves is known to occur from biological sources, plankton for instance (Haury et al., 1983; Stanton et al., 1996), seismic acoustic sources produce lower frequency waves that are not sensitive to these organisms.

2.2. Seismic data processing

The Iberian–Atlantic Margin lines were processed and analyzed similarly (with the exception of particular dataset dependent parameters) to ensure consistent interpretation from line to line. The linear direct wave (the wave which travels directly from source to receiver without reflecting) is shown emanating from the source at the surface and becoming deepest at the farthest offset. The acoustic reflections are hyperbolic and have lower amplitudes than the direct wave. Since this is a shot from a marine survey, we see water column reflections, seafloor reflections and those beneath the seafloor (Fig. 2).

The ultimate goal of seismic data processing is to produce an accurate, interpretable zero-offset section. All recorded seismic data contain signal and noise. To increase the interpretability of seismic data, it is necessary to increase the signal-to-noise ratio. Noise can be present in the form of random or coherent noise.

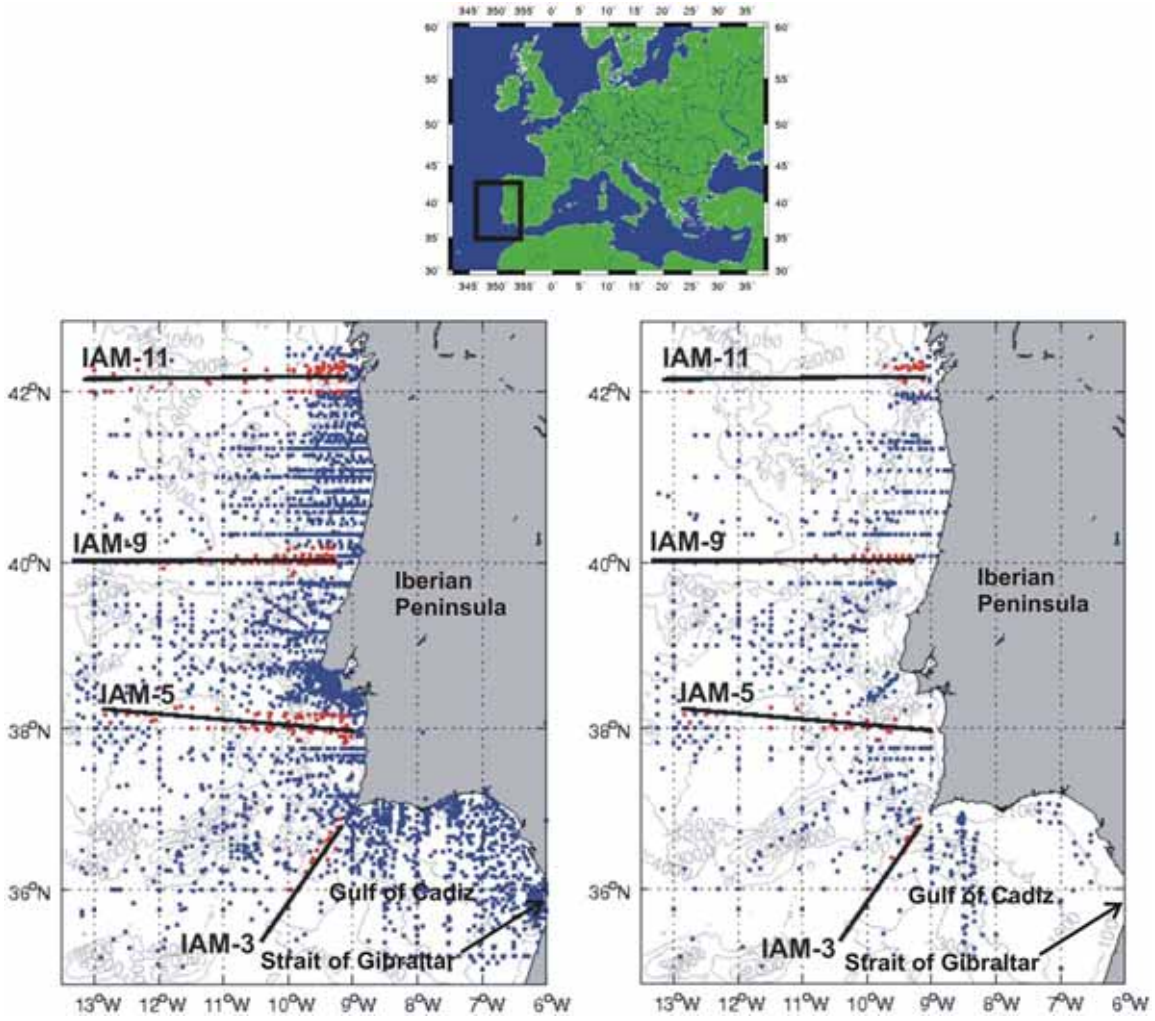

Fig. 1. Study location map showing seismic lines and oceanographic stations. Both databases supply quality-controlled data acquired throughout the 20th century. IAM sections are indicated. Stations within 20 km from these sections (red color) are used to build characteristic temperature and salinity fields. Left panel: WOD05 database (http://www.nodc.noaa.gov/OC5/SELECT/dbsearch/dbsearch.html). Right panel: Coriolis database (http://www.coriolis.eu.org/cdc/data_selection.htm).

Table 1
IAM Acquisition Parameters—the streamer used was the HSSQ/GX600 analog model.

Energy source—SWAG air gun array (bolt)
Total volume: 0.123 m^3
Nominal source depth: 10 m
Nominal shotpoint interval: 75 m
Peak energy: 20–50 Hz
Instrumentation—type: DFS-V
Format: SEG-D
Sample rate: 4 ms
Record length: 25 s
Low-cut filter OUT
High-cut filter 90 Hz
Cable Configuration—no. groups = 192
Streamer length: 5 km
Group interval: 25 m
Nominal cable depth: 15 m
Near offset (in-line): 254 m
CMP spacing: 12.5 m

The air gun array consisted of 36 BOLT guns organized into six identical sub strings.

While random noise is greatly reduced in the process of stacking (in the CMP method), due to the inherent redundancy of data traces, coherent noise has to be identified and attenuated to better enhance the reflection signal. In the case of seismic oceanography, the direct wave is the most prominent coherent noise and strongly masks shallow reflections.

We used an eigenvector filter to suppress the majority of direct wave energy and as a result enhance reflections. This filter, based on the Kahrunen–Loeve transform (Jones and Levy, 1987), decomposes the seismic traces into eigen-images. To suppress the direct wave, the shot record was first flattened using a linear moveout (LMO) correction with a constant sound speed of 1505 m s^{-1}. The eigenvector filter was applied and the LMO correction removed (Fig. 2) (Claerbout, 1978; Yilmaz, 1987). An Ormsby band-pass filter was then applied, truncating the frequency range to between 15 and 90 Hz, to increase the signal-to-noise ratio, with tapered ends (8/15−90/100 Hz) to prevent discontinuities such as oscillatory edge effects.

Next, a correction for divergence energy loss (geometric spreading) was applied that operates on the basis of an inverse distance, $1/r$, relationship. This cylindrical spreading correction assumes that the majority of energy comes from directly below the source, as opposed to off-line, as if energy propagates on a 2D vertical surface. This contrasts with spherical divergence corrections for 3D surveys, that would use a $1/r^2$ relationship. A single trace scalar was applied to balance trace amplitudes for display purposes. This trace scalar balanced all samples in a trace by the same scalar value, as opposed to scalars which are calculated in a

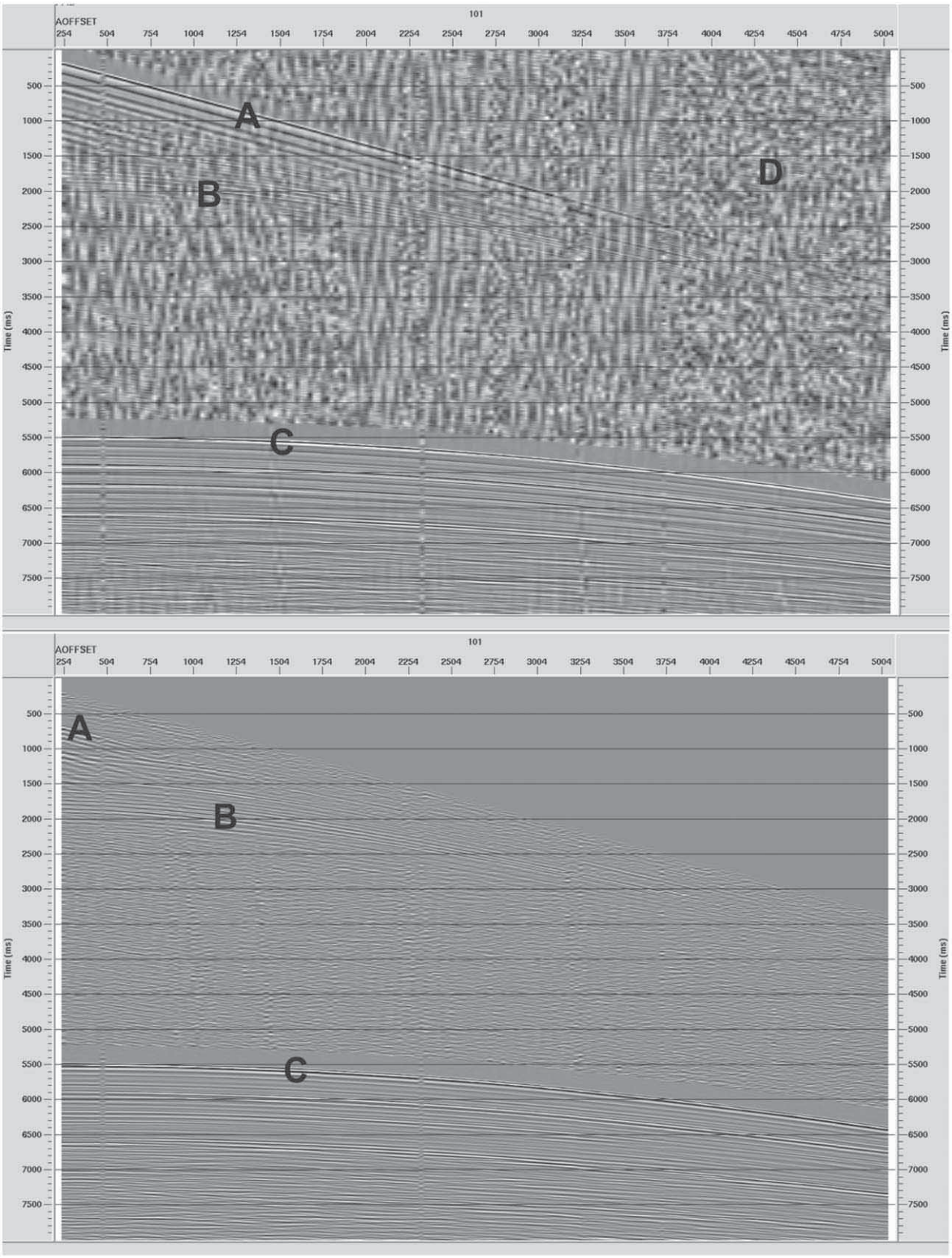

Fig. 2. Typical shot record from one IAM profile (IAM-3, SHOT 101) showing seismic events. (A) Direct wave. (B) Water column reflections. (C) Seafloor reflection. (D) Random noise. The shot record on the top shows the high amplitude direct wave (that masks lower amplitude water column reflections) and significant random noise. After application of the eigenvector filter, the direct wave is largely suppressed, with the exception of some residual energy at near offsets. The eigenvector filter is also very effective in reducing random noise.

sliding time window. In this way, lateral variations in amplitude are better preserved for data visualization. For true amplitude analysis (Section 3.2), no trace scalar was applied.

For a given CMP gather, in order to correct for the effect of normal moveout (NMO), that is, the effect of increasing reflection travel time to longer offset receivers, one needs to apply an appropriate shift in sound speed (known as 'stacking velocity') to flatten the hyperbolic reflectors (Hatton et al., 1986). In the water column, sound speed does not vary greatly, and indeed an assumed constant sound speed of $1500\,m\,s^{-1}$ will produce a stack (zero-offset section), yet velocity (sound speed) analysis is necessary and does improve the final stacked section, especially in the shallow ocean, where interfaces are more sensitive to processing sound speed adjustments (Fig. 3). Traces were then stacked, the process of summing together traces. This process increases coherent signal and attenuates random noise. Post-stack processing included an *f–x* deconvolution to improve signal-to-noise ratio (Cowen and Grant, 1985; Treitel, 1974).

Following post-stack noise reduction, a phase-shift time migration was applied to move reflectors to their true spatial locations and to collapse diffraction artifacts (Gazdag, 1978). Migration makes an adjustment of dipping interfaces but requires a priori knowledge of the acoustic structure of the media in question. In practice (in the absence of co-located and simultaneously recorded in situ oceanographic sound speed measurements) this is not known and must be arrived at iteratively through 'velocity analysis'. These fine depth variations are better sampled with oceanographic instruments and then used as the basis for seismic velocity analysis (that is, which sound speed function gives the best seismic stacking response). The result is a profile in two-way-time (vertical travel time to a reflection event and back) and horizontal distance. The two-way time profiles were converted to depth using the interval sound speed function calculated from picked stacking velocities using the Dix equation (Yilmaz, 1987). Fig. 3 illustrates the improved structural clarity obtained after velocity analysis. This is an important result, given the relatively small variations in water column sound speed as compared with those found in the solid earth.

2.3. Oceanographic data

Oceanographic data from 35°N to 42.5°N and 6°W to 13.5°W have been extracted from two historical databases: World Ocean Database 05 (WOD05) and Coriolis (Fig. 1a and b). Since most stations are present in both databases, some effort has been made to identify and delete duplicate stations. Stations acquired at the same time within 0.01° in latitude and longitude are considered to be duplicates (such a radius is larger than the usual precision in navigation systems, but short enough to distinguish between two different, yet proximally located stations). The number of stations available for each IAM section is 16 (IAM-3), 55 (IAM-5), 115 (IAM-9) and 58 (IAM-11). It is important to note that these stations, separated by an average distance that varies between 10 and 20 km, are not simultaneous in time (to one another, nor to their respective seismic profiles). Rather, the stations come from many different years and seasons, so the ensembled oceanographic sections in Fig. 1 cannot be used to examine any sort of horizontal coherence. Nevertheless, they are useful to illustrate the distribution of water masses along the path of the MU. Moreover, the outflow of MW from the Strait of Gibraltar does not experience substantial seasonal or interannual changes (Ambar et al., 2002; Candela, 2001), so we may expect that the large-scale characteristics of the MU, including its path and the characteristics of its exchange with the surrounding North Atlantic waters, are largely invariant.

NACW salinity decreases monotonically with depth from a sea-surface maximum value, until reaching the influence of MW. In the absence of North Atlantic intermediate waters (such as MW or Antarctic Intermediate Water, AAIW) salinity decreases rapidly with depth in the upper-thermocline until it becomes roughly constant at intermediate water levels (e.g. Machín et al., 2006, Fig. 3). Off the Iberian Peninsula, however, the presence of MW is easily detected through a change of sign in the slope of the salinity–depth relationship, which typically begins at neutral density values of $27.3\,kg\,m^{-3}$ or at depths of about 500–600 m, and corresponds to the salinity increasing back above 35.7. At deeper levels, in the 1700–1800 m depth and $27.90-27.93\,kg\,m^{-3}$ density range, the presence of MW disappears. These characteristics are easily appreciated in the temperature–salinity (*T–S*) diagrams (Fig. 4).

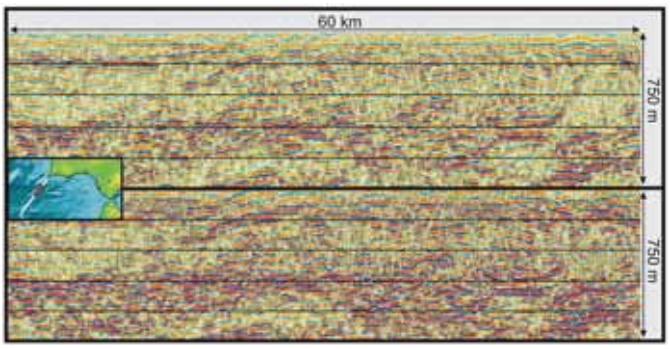

Fig. 3. Comparative results of semblance velocity (sound speed) analysis for a section of line IAM-3 (red, inset). Upper panel stacked with a constant sound speed of $1505\,m\,s^{-1}$. Lower panel stacked using a carefully picked temporally and spatially varying sound speed function. Note the better imaged reflections and improved structural clarity, especially in the shallow ocean.

3. Results

Figs. 5–8 present co-located seismic and oceanographic data. Characteristic features in the seismic sections are labeled by their section name (3, 5, 9 or 11) and a corresponding letter. We now present a brief description of these sections and the way they are partitioned using both seismic and oceanographic criteria.

3.1. Partition of seismic lines

Each seismic line is divided using both oceanographic and seismic criteria. The oceanographic partition into three principal zones is based on the presence of MW, which is brought by the MU either via advection or lateral and vertical diffusion. Zones 1 and 3 comprise pure NACW and NADW water masses, respectively, while Zone 2 includes all MW as well as the transitions between it and the overlying and underlying NACW and NADW. To establish this zonation we use a very simple criterion that intermediate waters with salinity above 35.7 have a significant contribution from MW and hence define Zone 2. Waters above and below correspond to Zones 1 and 3, respectively. In general, Zone 1 comprises waters between 0 and 600 m, Zone 2 between 600 and 1600 m and Zone 3 from 1600 m to the seafloor. The width of Zone 2 decreases with distance from the Strait of Gibraltar.

In order to have a comparable seismic partition in three zones we define the MW (Zone 2) based on the root mean square (rms) amplitude of seismic traces. Where this amplitude increases by a factor of five or more, we interpret this to represent the relatively high acoustic impedance of the MW. Amplitudes above and below

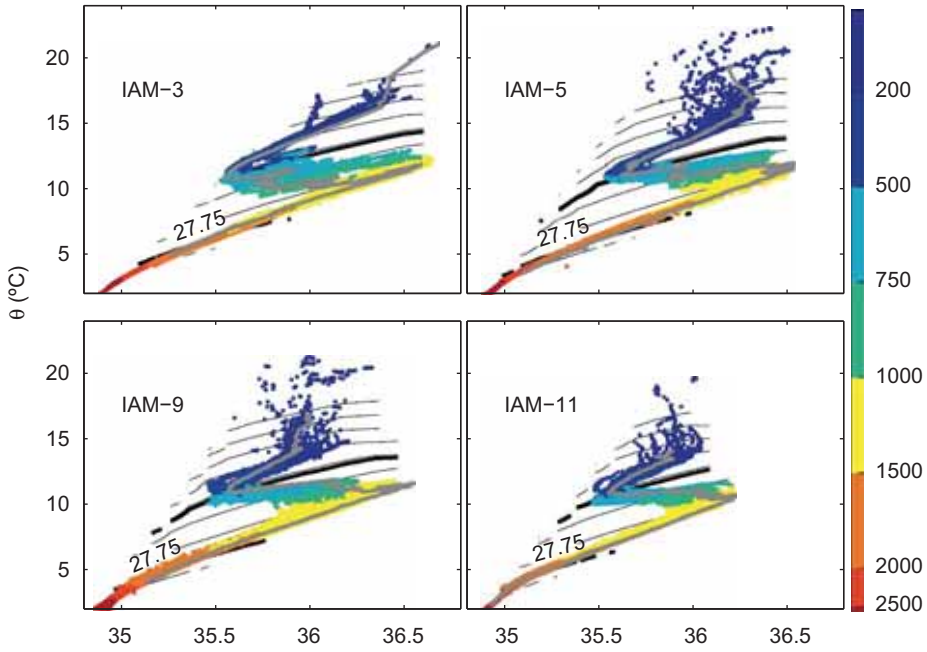

Fig. 4. *T–S* profiles for the co-located oceanographic sections. Depths (m) are indicated by colors. Isopycnals increase upward, with 0.25 kg m^{-3} intervals. The 27.3 and 27.93 isopycnals, which grossly delimit MW, are drawn as thick black lines. The gray line corresponds to an MW core station.

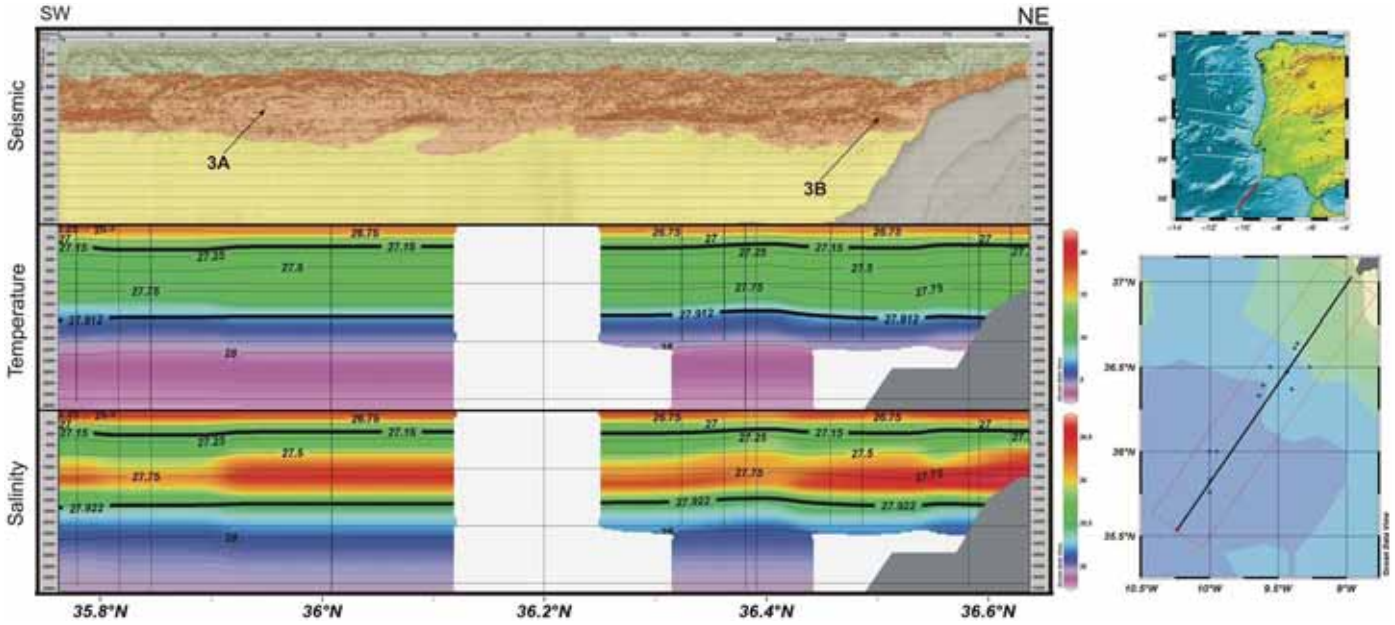

Fig. 5. Co-located seismic (line IAM-3) and historical oceanographic data. Zone 1 (NACW): green. Zone 2 (MW): red. Zone 3 (NADW): yellow. Seafloor: gray. MU is labeled on the top right of sections in white. See text for interpretation. Thick black lines in oceanographic data correspond to neutral density isopycnals (kg m^{-3}). Vertical black lines indicate locations of CTD casts with respect to seismic line. Bottom right inset shows location of seismic line relative to CTD casts (points). White zones indicate oceanographic data gaps.

the MW that fall outside this amplitude criterion are defined as either NACW (Zone 1) or NADW (Zone 3). Using this zonation, we overlay our interpretation by using three different colors: green—NACW; red—MW; yellow—NADW. By using these simple criteria a good correlation between the seismic images and the conventional oceanographic data is emphasized.

The seismic section in Fig. 5 is line IAM-3, a 186 km SW-NE line. There is a prominent lens shaped structure (Feature 3A) located at depths between 500 and 1500 m, extending from 17 to 66 km. The structure has high amplitude reflectivity at its top boundary and low amplitude reflectivity at its lower boundary. The low amplitude reflectivity contrasts starkly with the high amplitude horizontal reflectors present on either side and protrudes approximately 300–400 m below them. Feature 3A also shows moderate-to-high internal concentric reflectivity banding. Between about 78 and 98 km there is a sharp drop in the reflectivity of the lower boundary of Zone 2 (1400–1600 m), below which there are some lower amplitude sub-horizontal reflections extending to about 2000 m depth, notably deeper than the high amplitude adjacent horizontal reflectors. The north-east side of IAM-3 displays distinct lateral reflection continuity in Zone 2 and exhibits moderately dipping reflection events near the continental

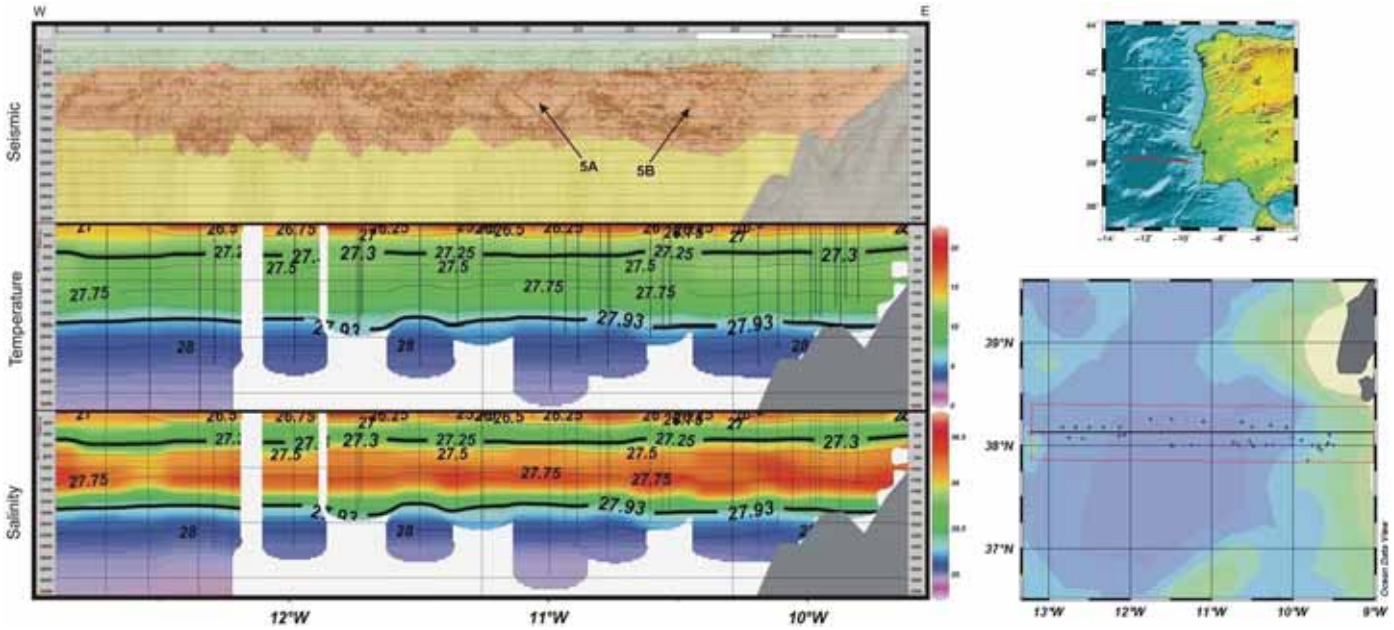

Fig. 6. Caption as in Fig. 5, but now for co-located seismic (line IAM-5) and historical oceanographic data.

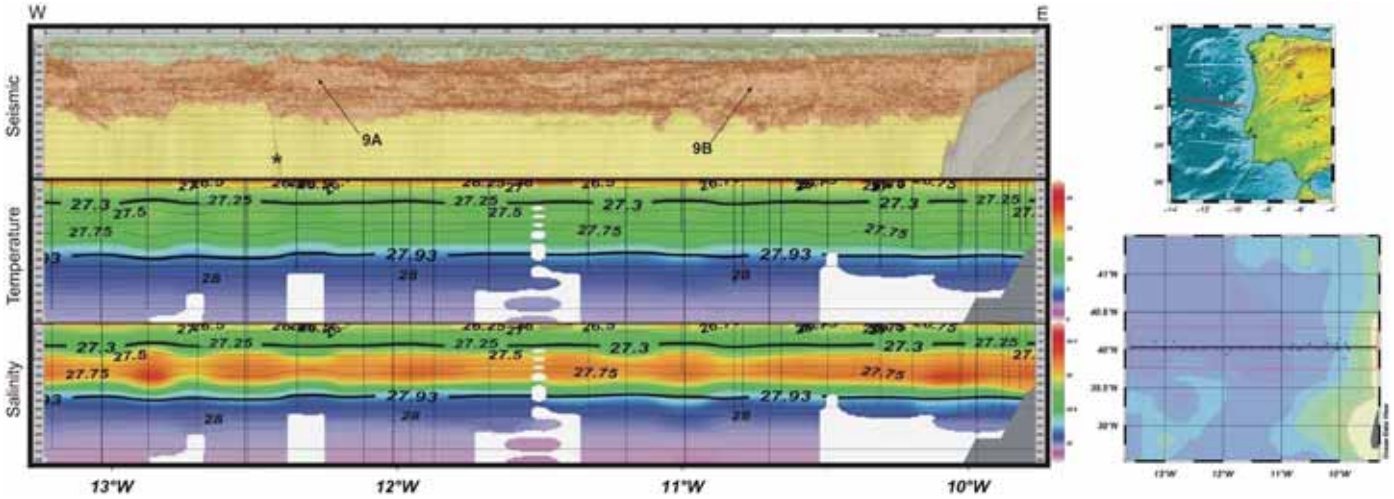

Fig. 7. Caption as in Fig. 5, but now for co-located seismic (line IAM-9) and historical oceanographic data. Asterisk indicates seismic processing artifact.

shelf (Feature 3B). Lateral seismic coherence (reflector lengths) range from 7 to 8 km in some sparse localities to over 60 km long in areas such as the western part of the profile, between 1200 and 1400 m. Zone 3 is largely featureless.

Seismic profile IAM-5 is a 330 km E–W line (Fig. 6). It is characterized by relatively horizontal layers in the upper 400 m (Zone 1). Zone 2 (from 400 to 1600 m) shows long seismic stratification in its easternmost portion (east of 200 km), but this coherency decreases towards the west, so that west of 160 km individual reflectors extend no more than 2–3 km. Two interesting features are noted: Feature 5A, located between 170 and 200 km is a distorted lens-like structure with two apparent cores. Feature 5B, in the eastern part, also appears spherical with low internal reflectivity. Below depths of approximately 1800 m reflectivity diminishes quickly (Zone 3).

Seismic line IAM-9 is a 300 km E–W profile (Fig. 7). Zone 1 contains horizontal reflectors, with maximum continuous lengths of 10 km. Zone 2 clearly exhibits higher amplitude reflections than Zone 1. From 0 to 10 km reflectors are intense and display long lateral continuity. From 10 to 55 km reflectors are no longer than 2–3 km. Between 55 and 70 km there is an increase in reflection continuity. These lengths increase across the MU, so that between 104 and 230 km we observe high lateral coherence, especially at depths between 1400 and 1700 m, where a single reflector can be traced for 85 km. East of 230 km, approaching the continental shelf, lateral seismic coherence degrades dramatically, with reflectors no longer than 5 km. Seismic features include the pronounced decrease in reflectivity between 600 and 1200 m centered around 84 km (Feature 9A). There are other transparent zones, with little internal structure, such as between 204 km and 235 km (Feature 9B), and between 140 and 170 km. Zone 3 is nearly featureless.

The northernmost line studied is IAM-11, a 220 km long E–W profile (Fig. 8). It shows high amplitude reflectivity with patches of low lateral coherence. At depths corresponding to Zone 1 continuous reflectors can extend up to 30 km, but are nominally between 10 and 20 km long. In Zone 2, in the western part of the profile (from 0 to 50 km) there is high amplitude reflectivity with maximum horizontal reflector lengths of 8 km. From 50 to 80 km and depths between 500 and 1600 m, where the continental shelf

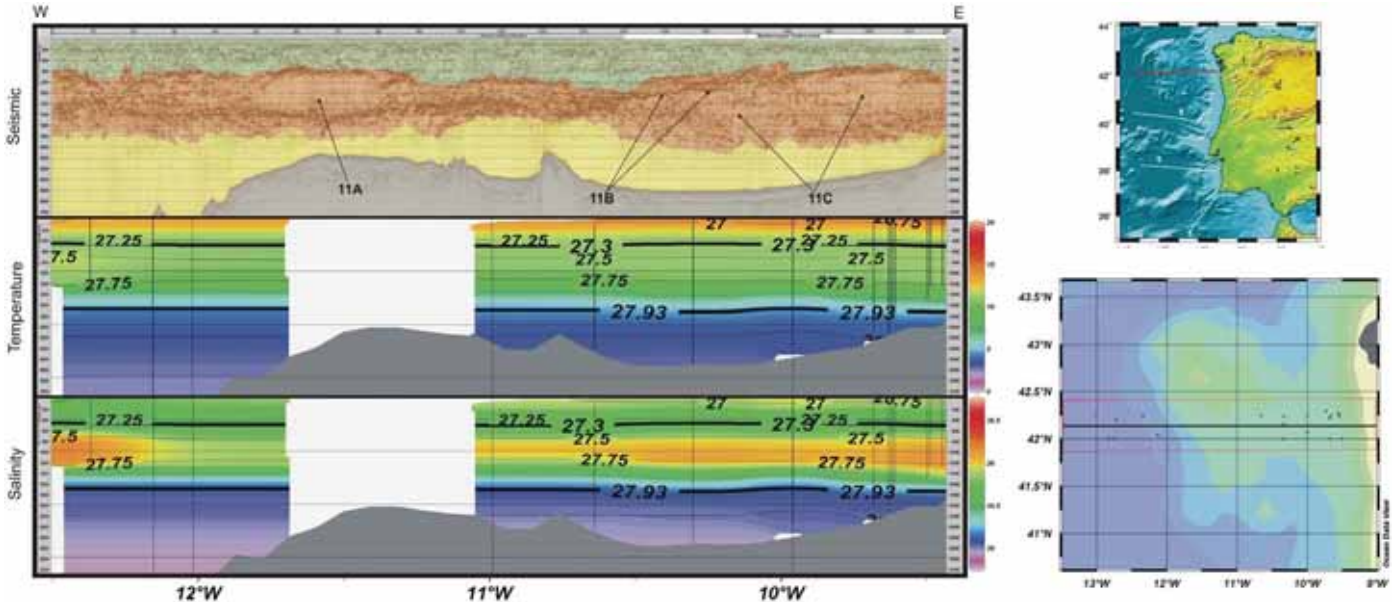

Fig. 8. Caption as in Fig. 5, but now for co-located seismic (line IAM-11) and historical oceanographic data.

noticeably rises, there is a large transparent area (Feature 11A). It is characterized by a high amplitude, relatively horizontally coherent upper boundary that is mimicked directly above (in length and signal strength) by a Zone 1 coherent reflector. Its bottom boundary shows high amplitude signal but is less laterally coherent. Within Zone 2, between 80 and 140 km, there is high amplitude seismic reflectivity but coherent lengths are no more than about 8 km, similar in signal character to the western part of the profile. From 140 km to the continental shelf (approximately 80 km) there are two main features, 11B and 11C. Feature 11B is defined by a high amplitude laterally coherent reflector that moderately rises toward the continental shelf exhibiting reflector lengths up to 20 km. Below this reflector there is a region of low, discontinuous reflectivity (Feature 11C) with sub-horizontal reflectors not longer than 2–3 km. Zone 3, corresponding to depths below 1800 m is highly seismically transparent across the line.

3.2. Seismic amplitude analysis

For display purposes, trace scaling was applied to Figs. 5–8. A trace balance processing algorithm, which applies a single value scalar across all data traces, was selected to preserve lateral amplitude variations and thus improve interpretive potential. However, amplitude contrasts between the seafloor and those internal to the water column are prominent, due to the fact that vertical trace balancing may distort relative amplitudes. Therefore, to further understand the quantitative relationships between the oceanic physical characteristics that influence reflectivity it is necessary to analyze true seismic amplitudes.

Using non-scaled data we calculated the rms seismic amplitude, within a chosen analysis window, for depths corresponding to the Mediterranean Water (500–1500 m; Armi et al., 1989; Richardson et al., 2000). The window locations and dimensions were chosen to coincide with the dominant flow of the MU, within about 80 km of the coast of Iberia (Ambar et al., 1999), while ignoring extremely noisy or clear areas (e.g. near the sea floor and the interior of Feature 5B, Fig. 6). The rms amplitudes are 4.26×10^5 (IAM-3), 3.29×10^5 (IAM-5), 2.71×10^5 (IAM-9) and 1.64×10^5 (IAM-11), a consistent trend of decreasing seismic amplitude with respect to distance from the source of the MW at the Strait of Gibraltar.

4. Discussion

The MU flows along the south and west coasts of Iberia, from its source in the Strait of Gibraltar (Madelain, 1970). As the MW enters Portimão Canyon at the south coast of Portugal it makes the transition from a density driven bottom current to an intermediate-depth jet, while entraining neighboring water with less momentum (Bower et al., 2002). From Portimão Canyon to Cape St. Vincent a deep and dense continuous MW stream forms (Bower et al., 2002), which is then coerced north along the continental slope by the Earth's rotation. Climatological salinity maps illustrate a high-salinity intermediate-water wedge stretching west of Cape St. Vincent. This is the result of enhanced lateral mixing operating far from the MU through large MW eddies (meddies) (Serra and Ambar, 2002). The MU continues further north along the western coast of Europe, possibly as far as Porcupine Bank (50°N), becoming progressively more diluted (Daniault et al., 1994; Iorga and Lozier, 1999).

4.1. Temperature and salinity fine structure

MW is distinct from the surrounding Atlantic Waters because of its relatively high salinity and temperature values (Ambar et al., 1999). In the Strait of Gibraltar the MU core has a temperature of 13.2 °C and a salinity of 38.45, which gives it a density of nearly 1030 kg m^{-3}, more than the underlying NADW (Richardson et al., 1989; Xu et al., 2007). As the MU enters the Gulf of Cádiz it rapidly entrains the neighboring waters and its density decreases until it eventually levels in the 27.7−27.8 kg m^{-3} isopycnic range, at the 1000–1500 m depth level. This has a positive anomaly of about 1.0 in salinity and 1.5 °C in temperature, as compared with NACW of the same density, which may be redistributed in the form of intermittent steps (fine structure) that become the source of reflectors. These steps consist of nearly constant temperature and salinity values with thicknesses on the order of 10 m (treads in the staircase) that change abruptly over distances of typically 1 m (risers in the staircase).

As the MU moves away from its origin, the temperature, and especially the salinity anomalies become progressively eroded, as is apparent from the T–S diagrams in Figs. 4 and 9. Such a decrease goes together with a reduction in the intensity and number of temperature and salinity steps, and hence in the seismic reflectors seen in the northernmost seismic section (Fig. 8). The erosion of these reflectors along the path of the MU is most probably the result of the interplay between along-stream advection and vertical/horizontal diffusion with the surrounding waters. The evolution of a layer between the MU and the background waters depends on three time scales: (1) an advective time scale T_a, which is the time the MU takes to travel from its Gibraltar source, (2) a vertical diffusive time scale T_v, or the time that the vertical diffusion takes to affect this layer and (3) a horizontal diffusive time scale T_h, the time that this layer takes to laterally incorporate the surrounding properties.

Let us estimate the order of magnitude of these time scales. The diffusive time scale for a layer of thickness h depends on the vertical diffusion coefficient K_v as, $T_d = sh^2/K_v$, where s is a factor that considers the fraction of the property transferred to the adjacent layer (Batchelor, 1977, p. 190). For the MW characteristics to become recognizable we choose $s = 1$, which corresponds to 50% dilution, so that with $K_v \simeq 10^{-5}\ \mathrm{m^2\ s^{-1}}$ (as reported by Ledwell et al. (1998), for the eastern subtropical Atlantic) we get $T_d \approx 115$ days for $h \approx 10$ m. The horizontal diffusive time scale for a layer $b \approx 30$ km long has a similar dependence on the horizontal diffusion coefficient, K_h, i.e. $T_e = sb^2/K_h$. A sensible choice is $K_h \simeq 10\ \mathrm{m^2\ s^{-1}}$, again from Ledwell et al. (1998), so that $T_e \simeq$ 104 days ($s = 1$). These two mechanisms tend to erode the layers and compete with its downstream advection. The advective time scale depends on the distance traveled from the region where the temperature and salinity steps were formed. For example, an average current speed of $U \approx 0.1\ \mathrm{m\ s^{-1}}$ would take a time $T_a = L/U \approx 115$ days to travel a distance $L \approx 1000$ km.

Within the MU these diffusive times are probably upper bound estimates, as vertical mixing will be enhanced through bottom friction and vertical shear, while lateral shear will cause enhanced horizontal diffusivity. Furthermore, in some instances the vertical and horizontal diffusive processes will interact such that, in some locations, fine structure may disappear in substantially shorter times. For example, a combined effective diffusive time scale on the order of 10 days implies that layers would not last more than some 100 km as they are advected by the MU.

4.2. Seismic profiles

Fine structure features within the MU are transient. Nonetheless, they have enough spatial and temporal coherence to be imaged by seismic data via strategically located cross-cutting sections of the MU. The coherence and intensity of these seismic reflections not only provide a measure of the sharpness and lateral coherence of the temperature and salinity steps but also draw the bounds of mesoscale structures such as meddies, and the rising/dipping of isopycnals associated with geostrophic currents. Let us now briefly describe some of these features as observed from the processed seismic lines (Figs. 5–8).

We identify the prominent lens shaped structure in IAM-3, Feature 3A (Fig. 5), as a meddy because of its spatial extent (Bower et al., 1997), its location at the depth range predicted by CTD and float surveys (500–1500 m, Armi et al., 1989; Richardson et al., 2000), and the marked horizontal reflection continuity (Chérubin et al., 2003). At the top of the meddy there is a higher than normal amplitude contrast. This agrees with reports of high density contrasts at the top of meddies as the result of lateral intrusions between MW and NACW and double diffusion processes (Biescas et al., 2008; Serra and Ambar, 2002). An abrupt drop in reflectivity, at about 80 km from the coast, seems to correspond with the western boundary of the MU (Ambar et al., 1999). The north-east side of IAM-3 displays increased lateral reflection continuity but also shows dipping events and areas of lower reflection amplitude (Fig. 5). Notable here is a half lens-shaped structure, 3B, possibly a meddy formed at Cape St. Vincent (Ambar et al., 1999; Serra and Ambar, 2002).

Structures 5A and 5B in IAM-5 (Fig. 6) may represent meddies generated at Cape St. Vincent (Bower et al., 2002; Richardson et al., 2000; Serra and Ambar, 2002). At approximately 200 km, there is a sudden change in signal character, from short-broken reflectors to long-smooth ones. This is likely an artifact due to changes in sea state during seismic recording on either side. The portion from 0 to 200 km (section A offshore) was recorded on 28–29 August 1993. The eastern portion of the line, from 200 to 325 km (section B nearshore), was recorded on 2–3 September 1993. Given that the acquisition parameters were invariant, the difference is most probably due to varying surface conditions at the times of acquisition. Wind speeds were noted on the Beaufort Wind Scale (Ruiz, 1997), of F6 (strong breeze: 41–50 km/h) for section A and F3 (gentle breeze: 13–19 km/h) for section B. As a result wave heights were significantly greater in section A as compared with section B, explaining the discontinuity in signal character and emphasizing the sensitivity of the method to the measurement of environmental conditions. In section A reflectivity and lateral coherence increases toward the coast, pointing to the presence of fine structure reflectors within the MU.

The broken reflectivity observed in the eastern and western parts of IAM-9, such as in Features 9A and 9B, suggests that less fine structure is present (Fig. 7). There are some instances of stable reflections in the central part of the line, but reflectivity appears broken in the nearshore region. This is surprising as the co-located oceanographic data displays a MU core of high salinity, and suggests lateral mixing or intrusions of surrounding water masses. Yet another possibility is that the MU decreases intermittently, for example during the formation of meddies off Cape St. Vincent (Serra and Ambar, 2002).

Profile IAM-11 contains a large lens shaped structure (Feature 11A), a meddy on the basis of its spatial dimensions (Armi et al., 1989; Richardson et al., 2000). Curiously, unlike the meddy from line IAM-3 (Feature 3A), it contains little internal structure (Fig. 8). This suggests an evolution of the meddy interior, which becomes more well mixed as it evolves downstream, resulting in smaller acoustic impedance contrasts and lower reflectivity. Toward the eastern part of the profile, a large sub-horizontal reflector separates NACW and MW (Feature 11B). Below this, a large area of broken reflectivity (Feature 11C) is imaged, suggesting that fine structure layers have less spatial coherence.

4.3. Along-stream changes in seismic reflectors and hydrographic properties

There are abundant seismically imaged mesoscale structures in the MW stratum. In particular, the MU core is easily identified through the rising reflectors against the continental slope, and several meddy-like structures are contoured by long horizontal reflectors. This is in accordance with studies showing increased MW-NACW mixing that occurs as a result of entrainment further away from the source of the MW at the Strait of Gibraltar (Daniault et al., 1994; Iorga and Lozier, 1999; Ochoa and Bray, 1991). However, the MU core displays intermittent reflectivity, which progressively breaks down along its path so that, far from Gibraltar, it becomes nearly transparent. This suggests that the edges of the MU sustain mixing processes, such as double

diffusive vertical mixing and lateral intrusions, prone to result in salinity and temperature staircases, while the MU core is possibly too turbulent to sustain vertical structures. It is possible that these structures are temporally produced through shear-mixing (Pelegrí and Sangrá, 1998) but do not appear to last long enough. Therefore, in the core of the undercurrent, the effective vertical and horizontal diffusivities may be substantially larger than at its edge, at least of order $K_v \simeq 10^{-4}\,\mathrm{m^2\,s^{-1}}$ and $K_h \simeq 100\,\mathrm{m^2\,s^{-1}}$. This would cause the relevant diffusive times (between vertically adjacent layers or between the MU core and the surrounding water) to be shorter than the advective times between adjacent IAM sections, separated by some 200 km.

With the exception of the MU core, the amplitude of seismic reflectors remains maximum within the MW (Zone 2) for all seismic lines. Nevertheless, the rms amplitudes in Zone 2 decrease with distance from the Strait of Gibraltar. We hypothesize that these reflectors are the result of double-diffusion processes, either through diffusive or salt-finger vertical diffusion (on the upper and lower parts of the MW stratum, respectively) or through lateral intrusions. Hence, we may expect that downstream changes in rms seismic amplitudes within the MW are related to changes in salinity and temperature contrasts between the MU and surrounding waters. It could be argued that the observed thermohaline fine structure is the result, to a large degree, of epipycnal (near-horizontal) processes, so that epipycnal contrasts are the most relevant quantities. However, the long-term near-horizontal diffusion of MW is so important that the salinity and temperature contrasts at the MW level are relatively small (Fig. 4), particularly if we are to consider relatively short horizontal distances within the eastern boundary subtropical gyre. Hence, by only considering temperature and salinity values on isopycnals we would likely underestimate the property differences necessary to maintain a long-term and large-scale fine structure field in the whole eastern boundary region. Therefore we believe it is best to consider the properties of the vertically adjacent water masses as they are ultimately responsible for the fine structure in the region, that is the core MW and the deepest NACW.

To calculate the salinity and temperature contrasts we have to define both the MU core and NACW background salinity and temperature values. Here we will use the simplest possible approach for both salinity and temperature. The NACW background salinity is estimated as the minimum salinity value in layers with neutral density less than $27.3\,\mathrm{kg\,m^{-3}}$ (roughly in the top 600 m). The MU core salinity is estimated from data between 27.2 and $27.90\,\mathrm{kg\,m^{-3}}$ (about 500 and 1400 m) in two different ways: (i) directly as the maximum salinity value, and (ii) as the salinity value associated with the maximum temperature value. Similarly, the NACW background temperature is estimated as the temperature corresponding to the minimum salinity value in the top 1000 m. The MU core temperature is estimated from data between 600 and 1400 m in two different ways: (i) directly as the maximum temperature value, and (ii) as the temperature value associated with the maximum salinity value. The NACW and MW data points are shown in Fig. 9 on top of the T–S diagrams for intermediate waters. The salinity, temperature, depth, density and sound speed values are reported in Table 2. When applying the temperature criterion to section IAM-3 we find two cores of MW at different depths, consistent with historical reports of two levels of MW in the western Gulf of Cádiz (Ambar et al., 2002). The two data points are shown in Fig. 9 and the corresponding numbers are reported in Table 2, but thereafter we set the corresponding salinity, temperature and depth values as the average of these pairs of values.

Temperature and salinity contrasts are directly calculated from the NACW and MW temperature and salinity values in Table 2. A plot of rms seismic amplitudes together with salinity and temperature contrasts, as a function of distance (Fig. 10a) does suggest a direct relation between these quantities. We may appreciate that seismic intensity, as well as salinity and temperature contrasts, decreases along the path of the MU. The precise salinity and temperature contrasts depend on whether we use the maximum salinity (subindex S: ΔS_S, ΔT_S) or the maximum temperature (subindex T: ΔS_T, ΔT_T) criteria, yet both methods show the same tendency. We may further examine if there is a relationship between seismic intensity and the overall salinity and temperature vertical gradients. These gradients are estimated as the property contrast divided by the vertical distance between the corresponding NACW and MW data points, e.g. the salinity contrast attained using the salinity criterion is divided by the vertical distance between the NACW point and the maximum salinity MW point (Fig. 10b). The vertical gradients depend largely on the selected criterion, the gradients being roughly twice as large when using the temperature criterion compared with the salinity criterion. Nevertheless, no matter which criterion, we find that the gradients decrease with distance from the Strait of Gibraltar, roughly paralleling the decrease in seismic amplitude. A linear regression between seismic amplitude and overall vertical temperature gradient gives a slope of 1.2×10^8 with a correlation coefficient of 0.95 when using the salinity criterion and 2.4×10^7 with a correlation coefficient of 0.99 when using the temperature criterion.

These results reinforce the hypothesis that the intensity of the reflectors responds to temperature and salinity vertical differences that favor double-diffusion processes. Yet, we still have not explored two important issues: if one of the two properties, temperature or salinity, has a predominant influence on the presence of these reflectors, and whether the reflectors are mainly controlled by either density or sound speed differences. Let us first explore the latter question. As mentioned in the Introduction, the presence of acoustic reflectors depends on the vertical contrasts of acoustic impedance $I = \rho c$, defined as the product of in situ density ρ and sound speed c. Changes in impedance are given by $\Delta(\rho c) = \rho \Delta c + c \Delta \rho$, such that the relative effect of the two is given by the fraction $(c\Delta\rho)/(\rho\Delta c)$.

The results are reported in Table 3, with subindices S and T referring to the differences obtained using the maximum salinity and temperature criteria, respectively (data in Table 2). The mean sound speed and density contrasts are calculated as the average of the values obtained using both criteria, i.e. $\Delta c = (\Delta c_S + \Delta c_T)/2$ and $\Delta\rho = (\Delta\rho_S + \Delta\rho_T)/2$. Notice that to compute the last column we use mean speed and density values calculated simply as the average between core MW and deep NACW values. In order to avoid having differences induced by the overwhelming pressure effect we use one single reference pressure, taken to be that corresponding to a depth of 1000 m, a characteristic depth of the MW. Contrasts in sound speed cause a change in impedance which is typically one order of magnitude larger than those changes caused by contrasts in density, although for section IAM-11 the difference reduces to a factor of about 3.5. These results could have been anticipated, as the difference in potential density between NACW and MW is about $0.2\,\mathrm{kg\,m^{-3}}$ while the sound speed difference is of a few $\mathrm{m\,s^{-1}}$ (at the same pressure), so that $\Delta\rho/\rho$ is one order of magnitude less than $\Delta c/c$.

Finally, we may assess the relative effect that salinity and temperature contrasts have on impedance. We may estimate the speed and density changes due to the salinity contrast as $\Delta c(S) = c(S_m, T_b, z_0) - c(S_b, T_b, z_0)$ and $\Delta\rho(S) = \rho(S_m, T_b, z_0) - \rho(S_b, T_b, z_0)$, and the speed and density changes due to the temperature contrast as $\Delta c(T) = c(S_b, T_m, z_0) - c(S_b, T_b, z_0)$ and $\Delta\rho(T) = \rho(S_b, T_m, z_0) - \rho(S_b, T_b, z_0)$, where S_m and T_m correspond to the maximum MW salinity and temperature values, S_b and T_b correspond to the deep NACW salinity and temperature values, and $z_0 = 1000\,\mathrm{m}$ is a characteristic depth of the MW.

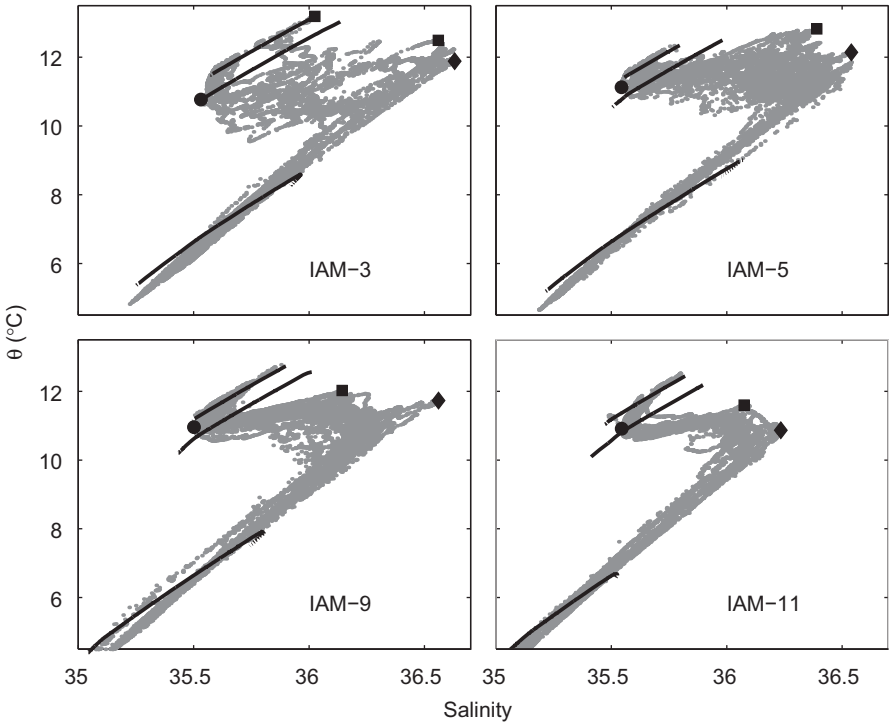

Fig. 9. *T–S* profiles for the co-located oceanographic data in the MW region, illustrating the criteria used to obtain the background and maximum salinity values. The black lines represent 27.2, 27.3 and 27.9 neutral densities. The dots indicate the background salinity and temperature values, the diamonds show the maximum salinity and temperature values as derived from the maximum salinity criterion, and the squares locate the maximum salinity and temperature values as derived from the maximum temperature criterion. Notice there are two squares in section IAM-3 corresponding to the two MW levels as explained in the text.

Table 2
Salinity, temperature, depth, density and sound speed values.

	MW core (*T* criteria)			MW core (*S* criteria)			Deep NACW		
	T_{max} (°C)	S_{max}	z (m)	T_{max} (°C)	S_{max}	z (m)	T (°C)	S	z (m)
IAM-3	13.19	36.03	482.7	11.96	36.62	1176.7	10.77	35.53	555.2
IAM-5	12.83	36.39	733	12.14	36.54	1098.7	11.12	35.54	489.7
IAM-9	12.02	36.14	661.8	11.73	36.56	1383.6	10.96	35.50	428.9
IAM-11	11.60	36.08	790	10.87	36.23	1153	10.91	35.54	427.5
	ρ (kg m^{-3})		c (m s^{-1})	ρ (kg m^{-3})		c (m s^{-1})	ρ (kg m^{-3})		c (m s^{-1})
IAM-3	1031.84		1517.74	1032.29		1515.16	1031.69		1509.72
IAM-5	1031.92		1517.81	1032.19		1515.68	1031.62		1510.96
IAM-9	1031.93		1514.99	1032.29		1514.30	1031.62		1510.36
IAM-11	1031.94		1513.27	1032.21		1510.92	1031.67		1510.22

The results are reported in Table 4, again with subindices *T* and *S* indicating the criterion used to obtain the salinity and temperature differences (Fig. 9). The last column of Table 4 displays the salinity/temperature ratio as obtained using the mean speed contrasts $\Delta c(S)/\Delta c(T) = (\Delta c(S)_T + \Delta c(S)_S)/(\Delta c(T)_T + \Delta c(T)_S)$; in parenthesis we show the range $(\Delta c_S(S)/\Delta c_S(T)$ to $\Delta c_T(S)/\Delta c_T(T)$. The results indicate that changes in seismic amplitude are more likely related to temperature than to salinity changes. The mean salinity/temperature ratio varies between 0.20 near the MW source to as high as 0.66 in downstream regions, where salinity contrasts are thus likely to play an increasing (but, still lesser) role in determining thermohaline fine structure. These values agree with recent studies (Nandi et al., 2004; Ruddick et al., 2009) that point to temperature as the major influence on reflection coefficient. Ruddick et al. (2009) obtained a synthetic seismic trace through a meddy located southwest of line (IAM-3) and found temperature–salinity contributions of 0.83–0.17, giving a salinity/temperature ratio of 0.20.

5. Conclusions

Analysis of four seismic lines acquired as part of the Iberian–Atlantic Margin survey, transecting the Mediterranean Undercurrent, shows distinct seismic reflectors in the upper 1800 m of the ocean. Layering is most prominent from approximately 500 to 1500 m, though this thickness varies from line to line. This corresponds to the base of the North Atlantic Central Water (NACW) and the whole Mediterranean Water (MW) stratum, in many instances with reflectors coherent over distances of over 100 km. Common to all sections is a significant decrease in seismic amplitude between 1400 m and approximately 1800 m, which we interpret as the base of the MW, beyond which North Atlantic Deep Water (NADW) is seismically near-transparent.

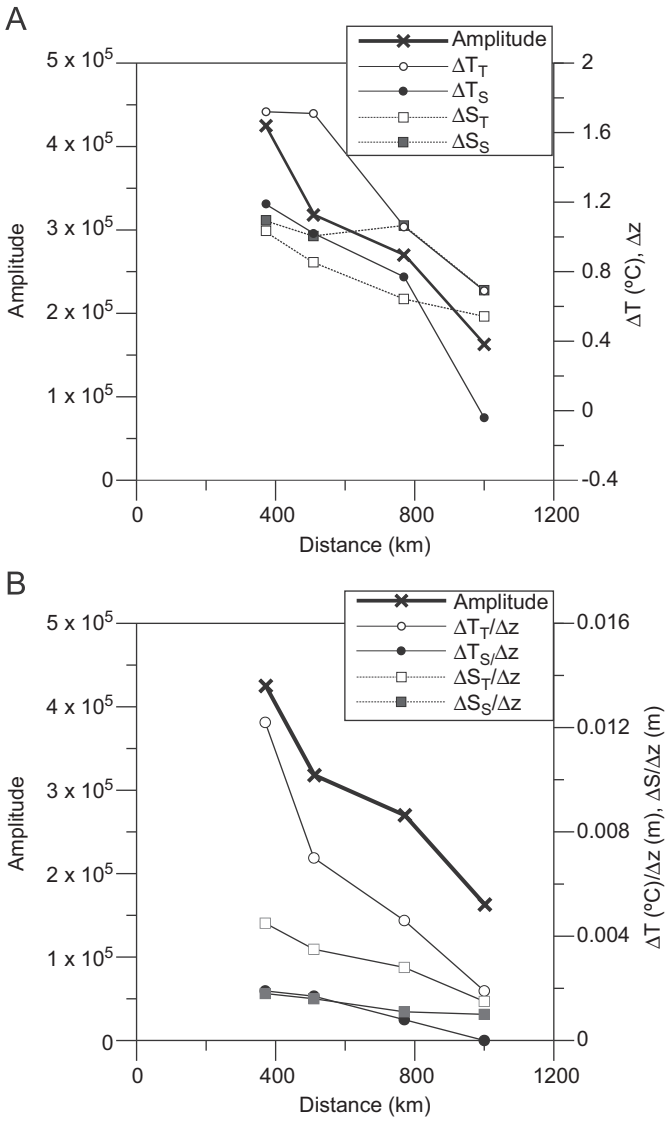

Fig. 10. (A) Decreasing rms seismic amplitudes for the MW and corresponding temperature and salinity contrasts between the MU core and the background NACW, ΔT (solid lines, circles) and ΔS (dotted lines, squares), respectively. We display two different values for the temperature and salinity contrasts, calculated as explained in the text. (B) Seismic amplitude variation alongside the overall vertical temperature and salinity gradients, $\Delta T/\Delta z$ (solid lines, circles) and $\Delta S/\Delta z$ (dotted lines, squares), respectively. In both panels we use the following key. Temperature criterion: empty circles/squares; salinity criterion: filled circles/squares (black: temperature, gray: salinity); rms seismic amplitude: crosses.

Three seismic reflectivity zones are identified, which we associate with NACW, MW and NADW, respectively. The thermohaline spatial structure of NACW and, particularly, MW strata may be studied using seismic oceanography because of the existence of large temperature and salinity contrasts between vertically adjacent water masses. These contrasts translate into gradients of density and sound speed, which bring about impedance gradients and correspondingly large variations in the amplitude of seismic reflectivity. Typical temperature and salinity contrasts between the MU core and the base of the overlying NACW are 1 °C and 1, respectively, which lead to (potential) density differences of about 0.3–0.5 kg m^{-3} and sound speed differences of about 5–7 m s^{-1}. Note that despite the fact that acoustic impedance depends on in situ density, while we look at the role of salinity and temperature contrasts on impedance gradients we must set one single depth in order to remove the overwhelming pressure effect, this is why here we speak of potential density.

Table 3
Sound speed and density contrasts calculated using both the temperature and salinity criteria.

	T criteria	
	$\Delta\rho_T$ (kg m^{-3})	Δc_T (m s^{-1})
IAM-3	0.22	8.02
IAM-5	0.30	6.85
IAM-9	0.29	4.63
IAM-11	0.27	3.05
	S criteria	
	$\Delta\rho_S$ (kg m^{-3})	Δc_S (m s^{-1})
IAM-3	0.60	5.44
IAM-5	0.57	4.72
IAM-9	0.67	3.94
IAM-11	0.54	0.70

	Mean				
	ρ (kg m^{-3})	$\Delta\rho$ (kg m^{-3})	c (m s^{-1})	Δc (m s^{-1})	$(c\Delta\rho)/(\rho\Delta c)$
IAM-3	1031.89	0.41	1513.09	6.73	0.10
IAM-5	1031.84	0.44	1513.86	5.79	0.11
IAM-9	1031.87	0.48	1512.51	4.29	0.16
IAM-11	1031.90	0.36	1511.16	1.88	0.28

Table 4
Sound speed contrasts caused by changes in salinity, $\Delta c(S)$, and temperature, $\Delta c(T)$.

	$\Delta c_S(S)$	$\Delta c_T(S)$	$\Delta c_S(T)$	$\Delta c_T(T)$	$r = \Delta c(S)/\Delta c(T)$
IAM-3	1.33	0.94	4.13	7.11	0.20 (0.32–0.13)
IAM-5	1.21	1.02	3.50	5.81	0.24 (0.35–0.18)
IAM-9	1.28	0.78	2.69	3.68	0.32 (0.48–0.21)
IAM-11	0.84	0.64	−0.16	2.39	0.66 (−5.25 to 0.27)

See text for explanations.

Seismic characterization of the Mediterranean Undercurrent (MU) is found in the reflectivity patterns seen within Zone 2 (MW). The undercurrent is located within some 80 km of the Iberian Peninsula continental slope, as viewed through the rising of reflectors against it, while the MU core remains largely transparent. We interpret these layers of reflectors as representing staircase-type structures induced by double-diffusion processes, which last longer than eroding diffusive processes, while within the MU core the erosion mechanisms dominate.

The analysis of root mean square (rms) amplitudes reveals a decreasing trend of MW seismic amplitude with respect to distance from the Strait of Gibraltar, alongside decreasing temperature and salinity contrasts between MW and the overlying NACW. We deduce that the decrease in seismic amplitude is a result of reduced double-diffusion processes that cannot compete with other diffusive processes that tend to erode the layering. Considering the deepest NACW and the core MW, the latter characterized by the mid-depth temperature maximum, we find a linear relationship between the overall vertical temperature gradient (in °C m^{-1}) and the true seismic amplitude with a linear regression slope of 2.4×10^7. This relation strongly suggests a causal relationship between the intensity of double-diffusion processes, and therefore fine structure, and true seismic amplitude.

Finally, we find that impedance changes are mainly controlled by sound speed changes, as opposed to density contrasts (a factor between 3.5 and 10), and that the speed variations are predominantly caused by temperature rather than salinity contrasts (a factor between 1.5 and 5).

Acknowledgments

The authors would like to extend thanks to the New and Emerging Science and Technology (NEST) initiative of the European Union—The GO Project (NEST-2003-1 adventure), the Spanish Ministry of Education and Science (CGL200404623), GEOCEAN, TOPOIBERIA (CSD2006-00041) and the Generalitat de Catalunya (2005SGR00874) for financial support. Seismic data were processed using ProMAX v.2003, Seismic Unix and Claritas 4.4.1 software. Oceanographic data were analyzed with Matlab and were plotted with Ocean Data View. Finally, we would like to thank Barry Ruddick and an anonymous reviewer for several useful comments which have greatly improved this paper.

References

Ambar, I., Armi, L.D., Bower, A., Ferreira, T., 1999. Some aspects of time variability of the Mediterranean Water off South Portugal. Deep-Sea Res. 46, 1109–1136.

Ambar, I., Serra, N., Brogueira, M., Cabecadas, G., Abrantes, F., Freitas, P., Gonçalves, C., González, N., 2002. Physical, chemical and sedimentological aspects of the Mediterranean outflow off Iberia. Deep-Sea Res. II 49, 4163–4177.

Armi, L.D., Hebert, D., Oakey, N., Price, J.F., Richardson, P.L., Rossby, H.T., Ruddick, B., 1989. Two years in the life of a Mediterranean salt lens. J. Phys. Oceanogr. 19, 354–370.

Batchelor, G.K., 1957. Symposium on Naval Hydrodynamics, National Academy of Sciences, Washington DC, pp. 409–423.

Batchelor, G.K., 1977. An Introduction to Fluid Dynamics. Cambridge University Press, Cambridge.

Biescas, B., Sallarès, V., Pelegrí, J.L., Machín, F., Carbonell, R., Buffett, G., Dañobeitia, J.J., Calahorrano, A., 2008. Imaging meddy finestructure using multichannel seismic reflection data. Geophys. Res. Lett. 35, L11609 10.1029/2008GL033971.

Bower, A.S., Armi, L.D., Ambar, I., 1997. Lagrangian observations of meddy formation during a Mediterranean Undercurrent seeding experiment. J. Phys. Oceanogr. 27, 2545–2575.

Bower, A.S., Serra, N., Ambar, I., 2002. Structure of the Mediterranean Undercurrent and Mediterranean Water spreading around the Southwestern Iberian Peninsula. J. Geophys. Res. 107 (C10), 3161 10.1029/2001JC001007.

Brandt, A., 1975. Acoustic returns from density fluctuations in turbulent jets. In: Oceans, vol. 75. IEEE, New York.

Candela, J., 2001. Mediterranean water and global circulation. Observing and modelling the global ocean. In: Church, J., Siedler, G., Gould, J. (Eds.), Ocean Circulation and Climate. Academic Press, New York, pp. 419–429.

Chernov, L.A., 1957. Correlation of amplitude and phase fluctuations of a wave propagating in a medium with random inhomogeneities. Akust. Zh. 3, 192.

Chérubin, L.M., Serra, N., Ambar, I., 2003. Low frequency variability of the Mediterranean Undercurrent downstream of Portimão Canyon. J. Geophys. Res. 108 (3), 3058 10.1029/2001JC001229.

Claerbout, J.F., 1978. Snell waves. Stanford exploration project report (15), Stanford University, pp. 57–72.

Cowen, C.F.N., Grant, P.M., 1985. Adaptive Filters. Prentice-Hall, New Jersey.

Daniault, N., Mazé, J.P., Arhan, M., 1994. Circulation and mixing of Mediterranean Water west of the Iberian Peninsula. Deep-Sea Res. 41 (1), 1614–1685.

Gazdag, J., 1978. Wave-equation migration by phase shift. Geophysics 43, 1342–1351.

Géli, and Cosquer, in preparation.

Gonella, J., Michon, D., 1988. Ondes internes profondes revelees par sismique reflexion au sein des masses d'eau en atlantique-est, 306.

González, A., Torné, M., Córdoba, D., Vidal, N., Matias, L.M., Díaz, J., 1996. Crustal thinning in the southwestern Iberia Margin. Geophys. Res. Lett. 23 (18), 2477–2480.

Goodman, L., 1990. Acoustic scattering from ocean microstructure. J. Geophys. Res. 95 (C7), 11,557–11,573.

Hatton, L., Worthington, M.H., Makin, J., 1986. Seismic Data Processing, Theory and Practice. Blackwell Scientific Publications, Oxford ISBN: 0-632-01374-5.

Haury, L.R., Wiebe, P.H., Orr, M.H., Briscoe, M.G., 1983. Tidally generated high-frequency internal wave packets and their effects on plankton in Massachusetts Bay. J. Mar. Res. 41, 65–112.

Holbrook, W.S., Fer, I., 2005. Ocean internal wave spectra inferred from seismic reflection transects. Geophys. Res. Lett. 32, L15604 10.1029/2005GL023733.

Holbrook, W.S., Páramo, P., Pearse, S., Schmitt, R.W., 2003. Thermohaline fine structure in an oceanographic front from seismic reflection profiling. Science 301, 821–824.

Iorga, M.C., Lozier, M.S., 1999. Signatures of the Mediterranean outflow from a North Atlantic climatology, 1, salinity and density fields. J. Geophys. Res. 104 (C11(a)), 25,985–26,029.

Johnson, G.C., Sanford, T.B., O'Neil Baringer, M., 1994. Stress on the Mediterranean outflow plume: part i. velocity and water property measurements. J. Phys. Oceanogr. 24, 2072–2083.

Jones, I.F., Levy, S., 1987. Signal-to-noise ratio enhancement in multichannel seismic data via the Karhunen–Loeve transform. Geophys. Prospect. 35, 12–32.

Ledwell, J., Watson, A., Law, C., 1998. Mixing of a tracer in the pycnocline. J. Geophys. Res. 103 (21), 21,499–21,529.

Machín, F., Hernández-Guerra, A., Pelegrí, J.L., 2006. Mass fluxes in the Canary Basin. Prog. Oceanogr. 70, 416–447.

Madelain, F., 1970. Influence de la topographie du fond sur l'ecoulement méditerranée entre le detroit de gibraltar et le cap saint-vincent. Cah. Oceanogr. 22 (1), 43–61.

Munk, W.H., Garrett, J.C.R., 1973. Internal wave breaking and microstructure (the chicken and the egg). Boundary-Layer Meteorol. 4, 37–45.

Munk, W.H., Wunsch, C., 1979. Ocean acoustic tomography: a scheme for large scale monitoring. Deep-Sea Res. A26, 123–161.

Nakamura, Y., Noguchi, T., Tsuji, T., Itoh, S., Niino, H., Matsuoka, T., 2006. Simultaneous seismic reflection and physical oceanographic observations of oceanic fine structure in the Kuroshio extension front. Geophys. Res. Lett. 33, L23605 10.1029/2006GL027437.

Nandi, P., Holbrook, W.S., Pearse, S., Páramo, P., Schmitt, R.W., 2004. Seismic reflection imaging of water mass boundaries in the Norwegian Sea. Geophys. Res. Lett. 31, L23311.

Obukhov, A.M., 1941. Scattering of sound in turbulent flow. Dokl. Akad. Nauk. SSSR 30, 611–614.

Ochoa, J., Bray, N.A., 1991. Water mass exchange in the Gulf of Cádiz. Deep-Sea Res. 38 (Suppl. 1), S465–S503.

Orr, M.H., Hess, F.R., 1978. Remote acoustic monitoring of natural suspensate distributions, active suspensate and slope/shelf water intrusions. J. Geophys. Res. 83, 4062–4068.

Ottersten, H., 1969. Atmospheric structure and radar backscattering in clear air. Radio Sci. 4, 1179–1193.

Páramo, P., Holbrook, W.S., 2005. Temperature contrasts in the water column inferred from amplitude-versus-offset analysis of acoustic reflections. Geophys. Res. Lett. 32, L24611 10.1029/2005GL024533.

Phillips, J.D., Dean, D.F., 1991. Multichannel acoustic reflection profiling of ocean water mass temperature/salinity interfaces. In: Potter, J., Warn-Varnas, A. (Eds.), Ocean Variability and Acoustic Propagation. Springer, New York, pp. 199–214.

Pelegrí, J.L., Sangrá, P., 1998. A mechanism for layer formation in stratified geophysical flows. J. Geophys. Res. 103, 30679–30693.

Price, J.F., Baringer, M.O., Lueck, R.G., Johnson, G.C., Ambar, I., Parrilla, G., Cantos, A., Kennelly, M.A., Sanford, T.B., 1993. Mediterranean outflow mixing and dynamics. Science 259, 1277–1282.

Richardson, P.L., Walsh, D., Armi, L.D., Schroder, M., Price, J.F., 1989. Tracking three meddies with sofar floats. J. Phys. Oceanogr. 19, 371–383.

Richardson, P.L., Bower, A.S., Zenk, W., 2000. A census of meddies tracked by floats. Progr. Oceanogr. 45, 209–250.

Ruddick, B., 1992. Intrusive mixing in a Mediterranean salt lens—intrusion slopes and dynamical mechanisms. J. Phys. Oceanogr. 22, 1274–1285.

Ruddick, B., 2003. Sounding out ocean fine structure. Science 301, 772–773.

Ruddick, B., Gargett, A., 2003. Oceanic double-infusion: introduction. Prog. Oceanogr. 56, 381–393.

Ruddick, B., Kerr, O., 2003. Oceanic thermohaline intrusions: theory. Prog. Oceanogr. 56, 483–497.

Ruddick, B., Song, H., Dong, C., Pinheiro, L., 2009. Water column seismic images as maps of temperature gradient. Oceanography 22 (1), 184–197.

Ruiz, A.L., 1997. Encyclopedia of the sea (in Spanish). Encyclopedias Planeta. ISBN 84-08-01589-3.

Schmitt, R.W., 1994. Double diffusion in oceanography. Ann. Rev. Fluid Mech. 24, 255–285.

Serra, N., Ambar, I., 2002. Eddy generation in the Mediterranean Undercurrent. Deep-Sea Res. II 49, 4225–4243.

Sheriff, R.E., Geldart, L.P., 1982. The CMP method of seismic reflection acquisition. Exploration Seismology, History, Theory and Data Acquisition, vol. 1. Cambridge University Press, Cambridge.

Stanton, T., Chu, K.D., Wiebe, P.H., 1996. Acoustic scattering characteristics of several zooplankton groups. ICES J. Mar. Sci. 53, 289–295.

St. Laurent, L., Schmitt, R.W., 1999. The contribution of salt fingers to vertical mixing in the North Atlantic tracer release experiment. J. Phys. Oceanogr. 29, 1404–1424.

Tatarski, V.I., 1971. The Effects of Turbulent Atmosphere on Wave Propagation. Israel Program for Scientific Translation, Jerusalem, US Department of Commerce Publ., TT-68-50464, pp. 153–162.

Thorpe, S.A., 2005. The Turbulent Ocean. Cambridge University Press, New York ISBN-13 978-0-521-83543-5.

Treitel, S., 1974. The complex Wiener filter. Geophysics 39-2, 169–173.

Tsuji, T., Noguchi, T., Niino, H., Matsuoka, T., Nakamura, Y., Tokuyama, H., Kuramoto, S., Bangs, N., 2005. Two-dimensional mapping of fine structures in the Kuroshio Current using seismic reflection data. Geophys. Res. Lett. 32, L14609 10.1029/2005GL023095.

Widess, M., 1973. How thin is a thin bed?. Geophysics 38, 1176–1180.

Wood, W.T., Holbrook, W.S., Sen, M.K., Stoffa, P.L., 2008. Full waveform inversion of reflection seismic data for ocean temperature profiles. Geophys. Res. Lett. 35, L04608 10.1029/2007GL032359.

Xu, X., Chassignet, E.P., Price, J.F., Özgökmen, T.M., Peters, H., 2007. A regional modeling study of the entraining Mediterranean outflow. J. Geophys. Res. 112, C12005 10.1029/2007JC004145.

Yilmaz, O., 1987. Seismic Data Processing, vol. 2. Society of Exploration Geophysicists.

CHAPTER 2

Stochastic Heterogeneity Mapping Around a Mediterranean Salt Lens

Mother, Mother Ocean, I have heard your call. I wanted to sail upon your waters since I was three feet tall. You've seen it all.

--Jimmy Buffett

Ocean Sci., 6, 423–429, 2010
www.ocean-sci.net/6/423/2010/

Ocean Science

Stochastic Heterogeneity Mapping around a Mediterranean salt lens

G. G. Buffett[1], **C. A. Hurich**[2], **E. A. Vsemirnova**[3], **R. W. Hobbs**[3], **V. Sallarès**[4], **R. Carbonell**[1], **D. Klaeschen**[5], **and B. Biescas**[4]

[1]Institut de Ciències de la Terra "Jaume Almera", C. Lluís Solé i Sabarís s/n, 08028 Barcelona, Spain
[2]Department of Earth Sciences, Memorial University of Newfoundland, Prince Phillip Drive, St. John's, Newfoundland, A1B 3X5, Canada
[3]Department of Earth Sciences, Durham University, Durham, DH1 3LE, UK
[4]Unitat de Tecnología Marina – Centre Mediterrani D'Investigacions Marines i Ambientals, Psg. Marítim de la Barceloneta, 37-49 08003 Barcelona, Spain
[5]Leibniz-Institute of Marine Sciences, IFM-GEOMAR, Duesternbrooker Weg 20, 24105 Kiel, Germany

Received: 10 November 2009 – Published in Ocean Sci. Discuss.: 4 January 2010
Revised: 12 March 2010 – Accepted: 18 March 2010 – Published: 31 March 2010

Abstract. We present the first application of Stochastic Heterogeneity Mapping based on the band-limited von Kármán function to a seismic reflection stack of a Mediterranean water eddy (meddy), a large salt lens of Mediterranean water. This process extracts two stochastic parameters directly from the reflectivity field of the seismic data: the Hurst number, which ranges from 0 to 1, and the correlation length (scale length). Lower Hurst numbers represent a richer range of high wavenumbers and correspond to a broader range of heterogeneity in reflection events. The Hurst number estimate for the top of the meddy (0.39) compares well with recent theoretical work, which required values between 0.25 and 0.5 to model internal wave surfaces in open ocean conditions based on simulating a Garrett-Munk spectrum (GM76) slope of −2. The scale lengths obtained do not fit as well to seismic reflection events as those used in other studies to model internal waves. We suggest two explanations for this discrepancy: (1) due to the fact that the stochastic parameters are derived from the reflectivity field rather than the impedance field the estimated scale lengths may be underestimated, as has been reported; and (2) because the meddy seismic image is a two-dimensional slice of a complex and dynamic three-dimensional object, the derived scale lengths are biased to the direction of flow. Nonetheless, varying stochastic parameters, which correspond to different spectral slopes in the Garrett-Munk spectrum (horizontal wavenumber spectrum), can provide an estimate of different internal wave scales from seismic data alone. We hence introduce Stochastic Heterogeneity Mapping as a novel tool in physical oceanography.

Correspondence to: G. G. Buffett
(gbuffett@ictja.csic.es)

1 Introduction

Mediterranean Water eddies, or "meddies", are large, warm, isolated lenses of highly saline Mediterranean Water that are found in the North Atlantic ocean. Mediterranean Water flows through the Strait of Gibraltar as an undercurrent (Bower et al., 2002), cascades down the continental shelf, while entraining less dense North Atlantic Central Water (Bower et al., 1997) and settles at depths between 500 and 1500 m (Richardson et al., 2000). The undercurrent then rounds the corner of the Iberian peninsula at Cape St. Vincent, directed north by the Coriolis force. It is here that meddies form, spinning off the main undercurrent, translating westward and rotating anti-cyclonically (Serra et al., 2002). Meddies were first reported in the western North Atlantic ocean by McDowell and Rossby (1978). Since that time they have been found to be a common feature in the North Atlantic ocean, (Richardson et al., 2000). Many different aspects of meddies are currently being researched to understand their properties as well as their influence on large-scale mixing and climate (e.g. Bashmachnikov et al., 2009).

Meddies have traditionally been studied using established oceanographic techniques, such as CTD (Conductivity-Temperature-Depth) probes to measure salinity and temperature (Ruddick, 1992) and acoustically tracked SOFAR floats

(Armi et al., 1989). Recently, multi-channel seismic (MCS) reflection profiling has been employed as a thermohaline imaging tool starting with the work of Holbrook et al. (2003) (e.g. Nandi et al., 2004; Nakamura et al., 2006; Buffett et al., 2009). Holbrook and Fer (2005) used this technique to study internal waves in the Norwegian Sea. They found that horizontal wave number spectra derived from digitizing seismic reflector horizons in the open ocean compared favorably with the Garrett-Munk spectrum (Garrett and Munk, 1975), which describes oceanic internal wave displacements. Biescas et al. (2008) performed the first detailed MCS analysis of a meddy. They found distinct seismic reflectivity differences in the upper and lower bounds of the meddy that are consistent with differences seen in historical temperature and salinity data. The upper boundary of the meddy was characterized by a few high-amplitude, laterally continuous reflections, whereas the lower boundary exhibited more numerous, shorter, lower amplitude reflectors.

To further understand meddy processes, we apply Stochastic Heterogeneity Mapping to the study of a meddy in the Gulf of Cadiz (Fig. 1). This method of statistically analyzing the reflection field of seismic data has been used extensively to study complex acoustic impedance variability in the solid earth (e.g. Goff et al., 1994; Holliger et al., 1994; Hurich and Kocurko, 2000; Carpentier and Roy-Chowdhury, 2007) even in areas where there is a predominance of diffuse reflectivity (as opposed to specular reflectivity) observed. This research represents the first application of Stochastic Heterogeneity Mapping to the ocean.

Stochastic Heterogeneity Mapping is based on the premise that the seismic reflection wave field contains information on the spatial properties of the reflecting bodies and could thereby be used to extract quantitative information about thermohaline finestructure. By extracting these parameters from a stacked seismic image of a meddy we can estimate the range of scales of its reflectivity patterns. In this way, we provide an estimate of the characteristic scales of internal waves of physical oceanographic processes directly from seismic data on zones of particular interest to oceanographers: the top and bottom (Biescas et al., 2008) and the sides of a meddy (Armi et al., 1989; Ruddick, 1992). Since Stochastic Heterogeneity Mapping operates on the reflectivity field of a processed seismic reflection profile, we focus here on that methodology and its interpretive implications, not on MCS data acquisition or processing. For an introductory treatise of MCS methodology as it relates to physical oceanography, we refer the reader to Ruddick et al. (2009). See Yilmaz (1987) for a more complete discourse on seismic data processing.

2 The stochastic model

The 1-D von Kármán model is described by three parameters: the correlation length (a), which is the upper limit for the scale invariance in heterogeneity (Carpentier, 2007), the

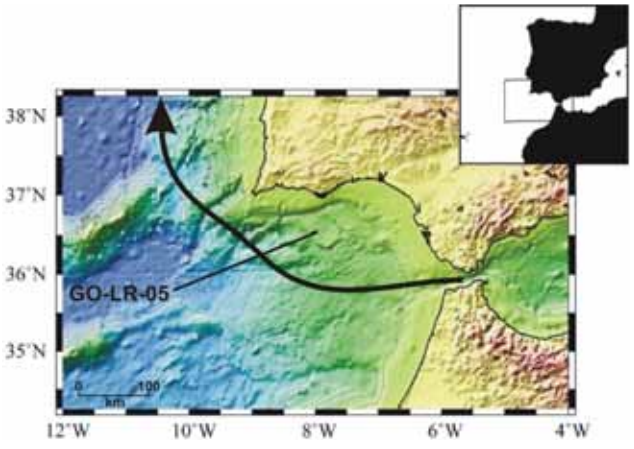

Fig. 1. Location of seismic profile and approximate trajectory of Mediterranean Outflow Water.

Hurst number (ν), a measure of surface roughness or equivalently, the richness of the range of scales in the power law distribution (having values between 0 and 1), and statistical variance. We apply unit variance to standardize the distribution. For scale sizes smaller than the correlation length, the von Kármán model describes a power law (fractal) process, where ν represents its exponent. The parameter, ν relates to the fractal dimension (D) by

$$D = E + 1 - \nu, \tag{1}$$

where E is the Euclidean dimension. For scales longer than the correlation length, the von Kármán model represents a process that is uncorrelated, such as white noise (Hurich and Kocurko, 2000). The structure of the impedance field, and hence its autocorrelation, are in accordance with the defined power spectrum. This spectrum could take on a variety of forms. However, we choose a von Kármán stochastic distribution because it is capable of describing a band-limited power law process and has been thoroughly tested for this algorithm, albeit for deep crustal studies (Carpentier and Roy-Chowdhury, 2007). However, the original work of Theodore von Kármán was to characterize random fluctuations in the velocity field of a turbulent medium (von Kármán, 1948), indicating that the method is also suited to the characterization of ocean fluid dynamics.

We express the analytic radial 2-D von Kármán power spectrum as (Carpentier, 2007),

$$P(\boldsymbol{k}) = \frac{4\pi \nu a_x a_z}{(1+\boldsymbol{k}^2)^{\nu+1}} \tag{2}$$

where a_x and a_z are the correlation lengths in the lateral and vertical directions, respectively, ν is the Hurst number, $\mathbf{k}$ is the weighted radial wavenumber, $\sqrt{k_x^2 a_x^2 + k_z^2 a_z^2}$. In the space

domain, we express a 2-D autocorrelation function (Goff and Jordan, 1988),

$$C(r) = \frac{G_\nu(r)}{G_\nu(0)}, \tag{3}$$

where $G_\nu(r) = r^\nu K_\nu(r)$, $K_\nu(r)$ being the second modified Bessel function of fractional order, and r the weighted radial autocorrelation lag, defined as $\sqrt{x^2/a_x^2 + z^2/a_z^2}$. $G_\nu(0)$ is defined according to Carpentier (2007),

$$G_\nu(0) = 2^{\nu-1}\Gamma(\nu), \tag{4}$$

where the gamma function, $\Gamma(\nu)=(\nu-1)!$.

From here we shall refer to correlation lengths as scale lengths because, in band-limited fractal fields, these lengths give the threshold below which scaling is determined by a power law (Carpentier and Roy-Chowdhury, 2007) and due to the fact that the decorrelation length is the dominant visual scale of the fabric morphology. Furthermore, we restrict our analysis to estimating horizontal scale lengths because determination of the vertical scale length is complicated by the estimation of source wavelet characteristics. This is because the source impulse is not a perfect spike, but is instead contaminated by side lobe energy, especially in the near offset traces (Yilmaz, 1987, pp. 17–20).

We estimate a_x and ν by performing a 2-D Fast Fourier Transform, from which we derive a 2-D power spectrum. We sum over the frequency direction and apply an inverse Fourier transform to obtain an autocorrelation function of NxM samples (Holliger et al., 1994; Carpentier and Roy-Chowdhury, 2007). We choose window sizes to be representative of the areas of interest. Constraints are placed on window sizes to cover a minimum of 10 times the horizontal scale length, and at least 2 cycles vertically. Next, the 1-D analytic von Kármán autocorrelation function (Eq. 4) is fitted to the calculated autocorrelation function using a model-space grid search and an L2 norm misfit, providing the estimate of a_x and ν. Temporal and spatial band-limiting of the broadband von Kármán spectrum of the seismic data affects the accuracy of estimating ν, which, based on impedance contrast fields and Primary Reflectivity Sections can be overestimated by a factor of 2. Likewise, a_x can be underestimated by a factor of 3–6 (Carpentier and Roy-Chowdhury, 2007). More recently, for complex scattered visco-elastic reflection data, Carpentier et al. (2009a) found underestimation factors for a_x of between 6 and 10 and overestimation factors of up to 10 for ν. These errors are due to the fact that, although the impedance field is highly correlated to the reflectivity field, they are not equivalent. Nonetheless, they represent the current state of the art of Stochastic Heterogeneity Mapping.

The Stochastic Heterogeneity Mapping algorithm accounts for the fact that reflectors may have some apparent dip by performing dip searching so that the values are derived along the angle of maximum coherence. However, apparent dips are small: 3° on average across the seismic section, with a standard deviation of 0.3°.

3 Results

Under the premise that the statistical properties of the scattered wave field are highly correlated to the properties of the acoustic impedance field (Carpentier and Roy-Chowdhury, 2007), we analyzed a meddy in the seismic line GO-LR-05 acquired in the Gulf of Cadiz during the GO (Geophysical Oceanography) cruise of April and May, 2007 (Fig. 1) for the distribution of the stochastic parameters Hurst number (Fig. 2) and correlation length (Fig. 3) around its margins. Four zones are described: The top of the meddy (A), the bottom of the meddy (B) and its sides (C and D). The stochastic parameters were extracted from the seismic section and overlaid using two different color schemes. The mapping procedure reveals the stochastic heterogeneity of the thermohaline-related fabric observed in the reflectivity field. Median and average Hurst numbers and scale lengths and their statistical distribution are reported in Fig. 4.

Zone A exhibits middle to higher Hurst number values, with median and average values of 0.35 and 0.39, respectively. Zone B is dominated by lower Hurst numbers, having a median value of 0.14 and an average of 0.17. Zone C/D Hurst numbers both lie approximately between those of Zone A and Zone B, showing median/average values of 0.24/0.27 (C) and 0.23/0.26 (D). However, the distributions of Zones C/D Hurst numbers both resemble that of Zone A, in that there is an absence of the lowest values (those between 0 and 0.1). The majority of Hurst numbers for Zone A lie in the range between 0.15 and 0.5 (67%). In contrast, Zone B shows the dominant Hurst number distribution between 0 and 0.25 (80%). The majority of the Hurst numbers for Zones C and D fall between 0.1 and 0.5, 68% and 64%, respectively.

Scale lengths for Zone A are the highest of the four zones: 1120 m (median) and 1310 m (average). Zone B values are lower than those of Zone A, having median and average values of 946 m and 1220 m, respectively. Zones C/D show a predominance of lower scale lengths, with median/average values of 697 m/961 m and 598 m/980 m, respectively. Further illustrating the difference between the sides and top/bottom: approximately 40% of scale lengths in Zones C and D are between 0 and 500 m, whereas only 12% and 22% of scale lengths for Zones A and B, respectively, lie in this range.

4 Discussion

The top of the meddy (Zone A), shows more lateral reflector continuity and a smaller variety of length scales than the bottom (Zone B). The Hurst numbers we obtained at Zone A (0.39) are in agreement with theoretical results Vsemirnova et al. (2009) modeled for open ocean conditions by emulating internal wave surfaces of a -2 slope Garrett-Munk spectrum (GM76). The Garrett-Munk spectrum describes the variation in internal wave energy in frequency and both vertical and

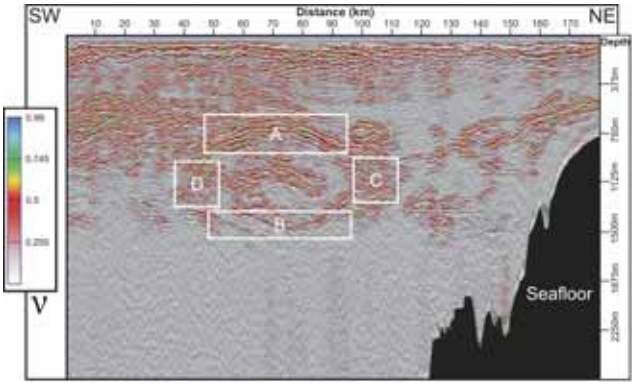

Fig. 2. Hurst number (ν) overlaid on seismic data along with stochastic parameter analysis boxes.

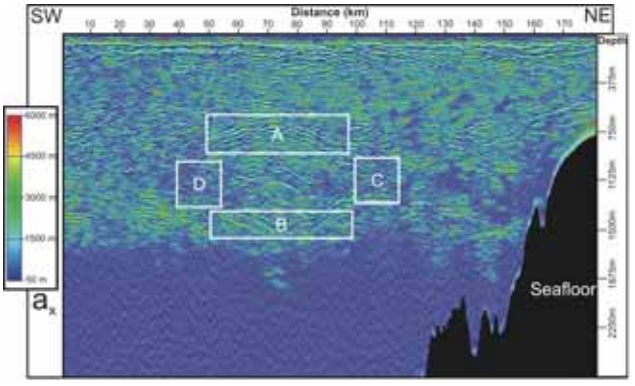

Fig. 3. Horizontal scale length (a_x) overlaid on seismic data along with stochastic parameter analysis boxes.

horizontal wavenumber spaces (Garrett and Munk, 1975). To simulate the GM76 slope they used Hurst numbers in a range of 0.25–0.50 with horizontal scale lengths of 5–10 km.

Internal waves develop in the ocean when density stratification is disturbed, thereby driving turbulent processes and diapycnal mixing (Müller and Briscoe, 2000; Garrett, 2003). The recorded seismic signal is reflected from ocean density stratification whether it is strong specular reflectivity or weak diffuse reflectivity. Acoustic impedance boundaries, which are what give rise to the reflectivity as revealed by the multichannel seismic (MCS) method, are expressed as the product of in-situ density and sound speed. Density and sound speed, in turn are functions of the relative proportions of temperature and salinity of the reflecting interface (Sallarès et al., 2009). Ruddick (1992) reported that the upper boundaries of meddies are dominated by diffusive convection processes, whereas the lower boundaries are susceptible to salt fingering. Salt finger scales are several orders of magnitude smaller than that directly resolvable by MCS methods (typically, in the tens of centimeter range, Linden, 1973). However, we may expect to detect them indirectly through our estimation of the Hurst number. The reason for this is that the Hurst number is a measure of surface roughness, low Hurst numbers being representative of a richer range of high wavenumbers. As seen in Fig. 4, Hurst numbers calculated for the bottom of the meddy are found to be dominated by lower numbers, whereas for the top and sides of the meddy, a lack of these lower Hurst numbers is found. This seems to indicate that, although we can not hope to actually resolve the salt fingers themselves with seismic frequencies, the richer range of high wavenumbers may point to the presence of such finer structures at the bottom as opposed to at the meddy's top and sides.

The scale lengths estimated from the seismic section are significantly lower than those used to model internal waves by Vsemirnova et al. (2009), even for Zone A (ca. 1 km compared to their 5–10 km). This difference is possibly due to the factor of 3–6 underestimation that was reported by Carpentier and Roy-Chowdhury (2007). Alternatively, the lower estimated scale lengths of the meddy may be explained by the fact that it is a dynamic, three-dimensional structure with currents that may be moving obliquely to the two-dimensional acquisition path. This is supported by an observation by Klaeschen et al. (2009), who estimated reflector motion by using an in-situ sound speed model near the NE edge of Zones A and B. They found longer horizontal wavelengths on the NE side of Zone A, as opposed to the SW side, and conclude that this is an indication of a different movement between the respective sides. Direct LADCP (Lowered Acoustic Doppler Current Profiler) measurements during the seismic acquisition confirmed that different parts of the meddy have different distributions of velocities, some along the path of the acquisition, some oblique to it (Klaeschen et al., 2009). That is, the meddy was not simply in solid-body rotation, but was stretching slightly in a SW direction at the time of acquisition. This motion could disturb the reflector undulations that we observe, as measured by the extracted horizontal scale lengths. Since we are making a two-dimensional observation in a three-dimensional domain, the stochastic values we obtained are measurements of the component of the meddy motion in the plane of the seismic profile, rather than in the direction of meddy motion. Thus, we can expect our measurements of scale length to be shorter than theoretical predictions based on two-dimensional geometries.

Due to the band limiting of the seismic data, the scales observed are most likely confined to the lower extreme of mesoscale (2–200 km) size features. It follows that the stochastic parameters seen here are a reflection of the effects of internal waves, as seen in the Garrett-Munk spectrum, rather than smaller turbulent, ie. Batchelor scales (Batchelor, 1959). The notably lower Hurst numbers seen at the bottom of the meddy (Zone B) may be partially a result of the fact that the frequency content of the source used in this survey (10–70 Hz) was too narrow-band to recover the smaller thermohaline staircases known to occur at the base of meddies (Ruddick, 1992). Thermohaline staircases are well-known structures in the ocean that range from tens to hundreds of meters thick and are found in regions where both temperature and salinity

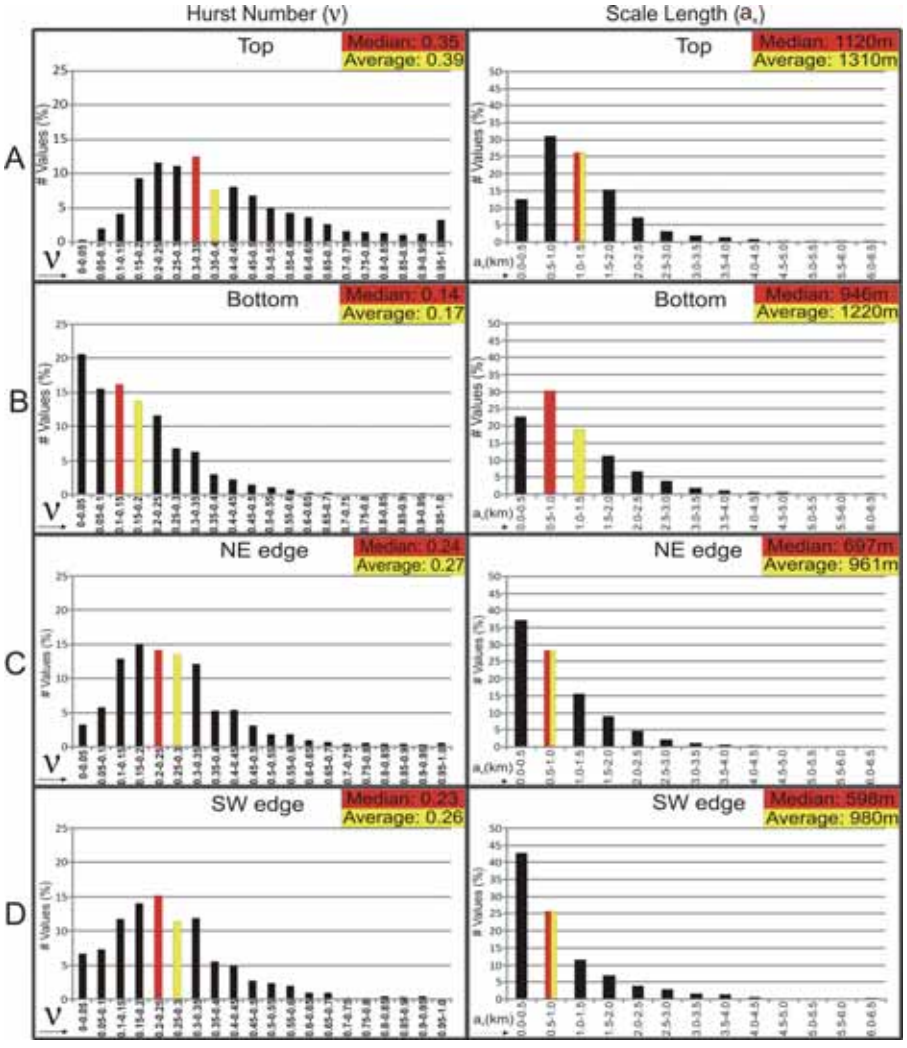

Fig. 4. Histograms of analyzed meddy zones showing the statistical distribution of Hurst number (ν) and horizontal scale length (a_x). Left column: ν; right column: a_x. Rows from top to bottom represent analyzed parts of the meddy, as outlined in analysis boxes (Figs. 2-3). Values of ν were grouped into families incremented by 0.05 between 0 and 1. Values of a_x were grouped into families incremented by 500 m between 0 and 6500 m. Median and average ν and a_x were then calculated.

increase upward in a manner that promotes salt fingering processes (Schmitt, 1994). Given the low frequency, narrowband source, we are only able to theoretically recover structures on the order of 5–75 m (Widess, 1973). Moreover, in the ocean there is both heat and mass diffusion across interfaces that produce a gradual change over a finite boundary width that may extend for several tens of meters (Hobbs et al., 2009). Hence, due to the thickness and gradient of a reflecting interface, a safer upper estimate for maximum resolvable thickness would be about double this estimate, between 10 and 150 m, the reflectivity being frequency dependent. As a result, it is plausible that the scales of some structures at the base of the studied meddy are smaller than those resolvable by this seismic source. Horizontal resolution is determined by the Fresnel zone width (Yilmaz, 1987, p. 470), itself a function of frequency, sound speed and depth. For the upper and lower limits of the meddy, considering a dominant frequency of 50 Hz, the horizontal resolution thus ranges between 12 and 30 m.

The seismic data presented herein are unmigrated. Given the near horizontal reflectivity of the seismic data (dips average at about 3° with a standard deviation of 0.3°) migration does not appreciably change the position of reflectors. With this in mind and due to the fact that the spatial bandlimit that is imposed by the migration operator smoothes the data, thus removing the information in the first few lags of the autocorrelation function, we chose to analyze the unmigrated stacks. Intriguingly, in recent studies by Carpentier et al. (2009a, b) Hurst numbers were found to actually exceed 1 in both synthetic and real data in order to obtain von Kármán

best fits. These exceptionally high Hurst numbers were said to be a result of the lateral smoothness of the data, caused by first-Fresnel-zone averaging during migration. Although migration, in principal, should completely collapse the 2-D seismogram's first-Fresnel zone, it is complicated by factors such as the lack of a sufficient recording aperture (zone of seismic illumination), complex scattering effects, wavelet attenuation and wavefront healing, and the uncertainty inherent in choosing the correct migration velocity (sound speed). Therefore there will always be some residual first-Fresnel-zone averaging. Furthermore, 2-D migration in a 2-D seismic profile will only collapse the first-Fresnel-zone and does not address out-of-plane reflections. This result supports the fact that the Hurst numbers we obtained from unmigrated data are not in the upper end (nor do they exceed) the range of theoretical Hurst numbers, and therefore may be closer to the true values than those extracted from migrated data, which are biased by many of the factors aforementioned. While we cannot definitively state that the low-end Hurst numbers are not a simply result of some remaining uncorrelated noise (thereby representing high-wavenumber artifacts, not actual sub-wavelength thermohaline finestructure) we can neither dismiss the possibility that the information contained in the first few autocorrelation lags actually has a positive effect on the von Kármán fitting process.

Uncertainty in both Hurst number and scale length could be further improved by inverting in-situ sound speed functions for acoustic impedance, thereby improving the certainty of correlation to the reflectivity field, upon which the stochastic parameters are extracted. Improving this certainty would also be useful to Stochastic Heterogeneity Mapping studies of the solid earth where sufficiently sampled sound speed functions are in practice unachievable.

5 Conclusions

We partition our observation of Hurst number distributions for the meddy into three distinct zones: top, bottom and sides. Our calculations of Hurst number for the top of the meddy agree with recent theoretical work, which used values between 0.25 and 0.5 to model internal wave surfaces in open ocean conditions based on simulating a Garrett-Munk (GM76) slope spectrum of -2. The corresponding scale lengths (correlation lengths) mapped over the same reflectivity field, however, do not fit as well to specific seismic reflection events. We suggest two possible explanations for this discrepancy: (1) because the stochastic parameters are derived from the reflectivity field rather than the impedance field the estimated scale lengths may be underestimated, as has been reported; and (2) because the meddy seismic image is a two-dimensional slice of a complex and dynamic three-dimensional object, the estimated scale lengths are likely skewed to the direction of flow, where the theory is most applicable. Nevertheless, this work illustrates the potential of Stochastic Heterogeneity Mapping as a tool within the growing discipline of Seismic Oceanography because it allows an estimate of lateral scale ranges of reflection events, and therefore actual physical oceanographic processes, such as internal waves. The multi-channel seismic (MCS) method records seismic signal that is reflected from ocean density stratification (i.e. boundaries of acoustic impedance). These boundaries give rise to the reflectivity field. Acoustic impedance boundaries are functions of the relative proportions of temperature and salinity of a given reflecting interface, whether strictly specular reflectivity or more diffuse reflectivity. So we may conclude that the estimations of the Hurst numbers and scale lengths are representative of actual thermohaline finestructure. We therefore introduce Stochastic Heterogeneity Mapping as a new tool of physical oceanography. To improve upon errors in estimation of Hurst number and scale length in-situ sound speed functions should be inverted for acoustic impedance. In this manner stricter constraints on the degree of correlation to the reflectivity field, upon which the stochastic parameters are extracted could be obtained. These constraints, in turn, could be applied to solid earth studies, where such a sound speed function is practically unattainable.

Acknowledgements. This work is part of the EU-FP6 funded GO project (NEST-2003-1 no. FP6015603). The data set used here was acquired within the framework of this project. It has also been supported by the Consejo Superior de Investigaciones Cientficas (CSIC) through the GEOCEAN PIF Project no. 200530f081. We also acknowledge important comments by John Goff, Stefan Carpentier and an anonymous reviewer.

Edited by: E. J. M. Delhez

References

Armi, L. D., Hebert, D., Oakey, N., Price, J. F., Richardson, P. L., Rossby, H. T., and Ruddick, B.: Two years in the life of a Mediterranean salt lens, J. Phys. Oceanogr., 19, 354–370, 1989.

Bashmachnikov, I., Machín, F., Mendonça, A., and Martins, A.: In situ and remote sensing signature of meddies east of the mid-Atlantic ridge, J. Geophys. Res., 114, C05018, doi:10.1029/2008JC005032, 2009.

Batchelor, G. K.: Small-scale variation of convected quantities like temperature in turbulent fluid. Part 1. General discussion and the case of small conductivity, J. Fluid Mech., 5, 113–133, 1959.

Biescas, B., Sallarès, V., Pelegrí, J. L., Machín, F., Carbonell, R., Buffett, G. G., Dañobeitia, J. J., and Calahorrano, A.: Imaging meddy finestructure using multichannel seismic reflection data, Geophys. Res. Lett., 35, L11609, doi:10.1029/2008GL033971, 2008.

Bower, A. S., Armi, L., and Ambar, I.: Lagrangian Observations of Meddy Formation during A Mediterranean Undercurrent Seeding Experiment, J. Phys. Oceanogr., 27, 2545–2575, 1997.

Bower, A. S., Serra, N., and Ambar, I.: Structure of the Mediterranean Undercurrent and Mediterranean Water spreading around

the southwestern Iberian Peninsula, J. Geophys. Res., 107(C10), 3161, doi:10.1029/2001JC001007, 2002.

Buffett, G. G., Biescas, B., Pelegrí, J. L., Machín, F., Sallarès, V., Carbonell, R., Klaeschen, D., and Hobbs, R. W.: Seismic reflection along the path of the Mediterranean Undercurrent, Cont. Shelf Res., 29, 1848–1860, doi:10.1016/j.csr.2009.05.017, 2009.

Carpentier, S.: On the estimation of stochastic parameters from deep seismic reflection data and its use in delineating lower crustal structure, PhD thesis, Universiteit Utrecht, 2007.

Carpentier, S. and Roy-Chowdhury, K.: Underestimation of scale lengths in stochastic fields and their seismic response: a quantification exercise, Geophys. J. Int., 169, 547–562, 2007.

Carpentier, S. F. A. and Roy-Chowdhury, K.: Conservation of lateral stochastic structure of a medium in its simulated seismic response, J. Geophys. Res., 114, B10314, doi:10.1029/2008JB006123, 2009a.

Carpentier, S. F. A., Roy-Chowdhury, K., Stephenson, R. A., and Stovba, S.: Delineating tectonic units beneath the Donbas Fold Belt using scale lengths estimated from DOBRE 2000/2001 deep reflection data, J. Geophys. Res., 114, B10315, doi:10.1029/2008JB006124, 2009b.

Garrett, C. and Munk, W.: Space-Time Scales of Internal Waves: A Progress Report, J. Geophys. Res., 80(3), 291–297, 1975.

Garrett, C.: Internal tides and ocean mixing, Science, 301, 1858–1859, 2003.

Goff, J. A., Holliger, K., and Levander, A. R.: Modal fields: A new method for characterization of random seismic velocity heterogeneity, Geophys. Res. Lett, 21(6), 493–496, 1994.

Goff, J. A. and Jordan, T. H.: Stochastic modeling of seafloor-morphology: Inversion of seabeam data for second order statistics, J. Geophys. Res., 93(6), 13589–13608, 1988.

Hobbs, R. W., Klaeschen, D., Sallarès, V., Vsemirnova, E., and Papenberg, C.: Effect of seismic source bandwidth on reflection sections to image water structure, Geophys. Res. Lett., 36, L00D08, doi:10.1029/2009GL040215, 2009.

Holbrook, W. S. and Fer, I.: Ocean internal wave spectra inferred from seismic reflection transects. Geophys. Res. Lett., 32, L15604, doi:10.1029/2005GL023733, 2005.

Holbrook, W. S., Páramo, P., Pearse, S., and Schmitt, R. W.: Thermohaline fine structure in an oceanographic front from seismic reflection profiling, Science, 301, 821–824, 2003.

Holliger, K., Levander, A. R., Carbonell, R., and Hobbs, R.: Some attributes of wave fields scattered from ivrea-type lower crust, Tectonophysics, 232, 267–279, 1994.

Hurich, C. A. and Kocurko, A.: Statistical approaches to interpretation of seismic reflection data, Tectonophysics, 329, 251–267, 2000.

Klaeschen, D., Hobbs, R. W., Krahmann, G., Papenberg, C., and Vsemirnova, E.: Estimating movement of reflectors in the water column using Seismic Oceanography, Geophys. Res. Lett., 36, L00D03, doi:10.1029/2009GL038973, 2009.

Linden, P. F.: On the structure of salt fingers, Deep-Sea Res., 20, 325–340, 1973.

McDowell, S. E. and Rossby, H. T.: Mediterranean Water: An Intense Mesoscale Eddy off the Bahamas, Science, 202, 4372, 1085–1087, doi:10.1126/science.202.4372.1085, 1978.

Müller, P. and Briscoe, M. G.: Diapycnal Mixing and Internal Waves, Oceanography, 13 98–103, 2000.

Nandi, P., Holbrook, W. S., Páramo, P., Pearse, S., and Schmitt, R. W.: Seismic reflection imaging of water mass boundaries in the Norwegian sea, Geophys. Res. Lett., 31, L23311, doi:10.1029/2004GL021325, 2004.

Nakamura, Y., Noguchi, T., Tsuji, T., Itoh, S., Niino, H., and Matsuoka, T.: Simultaneous seismic reflection and physical oceanographic observations of oceanic fine structure in the kuroshio extension front, Geophys. Res. Lett., 33, L23605, doi:10.1029/2006GL027437, 2006.

Richardson, P. L., Bower, A. S., and Zenk, W.: A census of meddies tracked by floats, Prog. Oceanogr., 45, 209–250, 2000.

Ruddick, B.: Intrusive mixing in a Mediterranean salt lens – intrusion slopes and dynamical mechanisms, J. Phys. Oceanog., 22, 1274–1285, 1992.

Ruddick, B., Song, H., Dong, C., and Pinheiro, L.: Water column seismic images as maps of temperature gradient, Oceanography, 22, 192–205, 2009.

Schmitt, R. W.: Triangular and asymmetric salt fingers, J. Phys. Oceanogr., 24(4), 855–860, 1994.

Serra, N., Ambar, I., and Käse, R. H.: Observations and numerical modeling of the Mediterranean outflow splitting and eddy generation, Deep Sea Res. II, 52, 383–408, doi:10.1016/j.dsr2.2004.05.025, 2005.

Sallarès, V., Biescas, B., Buffett, G., Carbonell, R., Dañobeitia, J. J., and Pelegrí, J. L.: Relative contribution of temperature and salinity to ocean acoustic reflectivity, Geophys. Res. Lett., 36, L00D06, doi:10.1029/2009GL040187, 2009.

von Kármán, T.: Progress in the statistical theory of turbulence, J. Mar. Res., 7, 252–264, 1948.

Vsemirnova, E., Hobbs, R. W., and Bargagli, A.: Testing recovery of ocean properties using an emulation of internal wave surfaces, Geophys. Res. Abstracts, 11, EGU2009-1253, EGU General Assembly, Vienna, 2009.

Widess, M.: How thin is a thin bed?, Geophysics, 38, 1176–1180, 1973.

Yilmaz, O.: Seismic Data Processing, Society of Exploration Geophysicists, Tulsa, OK, USA, 1987.

CHAPTER 3

Near Real-Time Visualization of Oceanic Internal Waves Using Multi-Channel Seismic Reflection Profiling

For me, it is far better to grasp the Universe as it really is than to persist in delusion, however satisfying and reassuring.

— Carl Sagan

Note: This Chapter presents an unpublished work that has been submitted to a peer reviewed journal.

Abstract

Visualization of thermohaline finestructure is an important way of understanding ocean fluid dynamics. We present the first near real-time animation of the motion of internal waves from the analysis of seismic reflection data. Reflection 'seismic oceanography' images are created by the passage of a regularly repeating impulsive source and streamer (cable filled with hydrophones) on the surface of the ocean. Seismic images are created by summing together the signal reflected from temperature and salinity (acoustic impedance) contrasts within the ocean creating seismic 'stacked' sections. Due to the inherent redundancy of the method, random noise is attenuated, while signal is preserved. If the original signal-to-noise ratio is good, the whole streamer need not be stacked to create an interpretable image. A processing scheme has been devised such that a series of images, or "stacks", are obtained in order to build up a 7-frame "movie" of fluctuating internal waves over a period of just 20 minutes. Separate seismic stacked sections are created by partitioning the acquisition streamer into 7 groups thereby imaging the same seafloor-referenced location at progressively later times. As the streamer passes over this static geographical point, motions within the water column are observed. Each stack was created with a subset of the complete streamer. Therefore, each stack can be considered an image of the water column at a particular time step (movie frame). In this way each image shows a slightly different thermohaline fabric allowing us to create a striking visualization of the temporally evolving internal waves.

3.1 - Introduction

Visualization of otherwise unseen physical phenomena such as internal waves is an important step to a fuller understanding of these phenomena. Broadly, as a tool of remote sensing, visualization can come in the form of a one-time spatial illumination of

the body in question (for example, in the case of the specular reflection of light, a photo). Likewise, in the case of the specular reflection of sound waves, we are able to create a stacked seismic section providing us with information about the Earth or ocean that was previously unrealized.

Seismic reflection investigations have been common for delineating the gross structure of the Earth's crust mantle and core for several decades - first as two-dimensional transects, later as three-dimensional volumes. More recently, the repeated acquisition of seismic data over the same location in time-steps of several months or years has added the fourth dimension of time to the interpretation of such things as petroleum reservoir monitoring [Lumley, 2001], monitoring of CO_2 sequestration [Chadwick et al., 2005] and the active migration of faults [Cheng, 2009].

Holbrook et al. [2003] made the first modern analyses of seismic data acquired of ocean structure and found that the acoustic impedance boundaries, which give rise to seismic reflectivity, were the result of temperature and salinity fluctuations, or thermohaline finestructure, already known for some time by conventional oceanographic methods [Stommel and Federov, 1967] but not able to be visualized at high horizontal resolution (MCS method provides approximately 10 m horizontal resolution compared with typical 1 km CTD casts).

More recent physical oceanographic studies using seismic reflection profiling as a tool have imaged thermohaline finestructure. For example, Biescas et al [2008] imaged the finestructure of Meddies for the first time and Sallarès et al. [2009] identified the relative contributions of temperature and salinity to reflectivity. Further successful attempts to utilize seismic reflection in oceanography have imaged the Kuroshio Current, near Japan (Nakamura et al. [2006], Tsuji et al. [2005]), the Norwegian Sea (Nandi et al. [2004], Páramo and Holbrook [2005]), the Southern Ocean [Sheen et al., 2009] and the Caribbean Sea [Fer et al., 2010]. All these studies represented two spatial dimensions of the ocean: in depth and horizontally along the direction of acquisition. Blacic and Holbrook [2009] performed the first 3D study of seismic oceanography using two parallel acquisition swaths. From these data they were able to obtain the orientation of internal wave crests.

The dynamic nature of the ocean presents a challenge for the seismologist for two reasons: 1) the motion of ocean currents, and therefore thermohaline finestructure, is variable on the order of minutes or hours not months or years (e.g. Thorpe [2005], Géli et al. [2009]). Thus, any methods used to measure movement in the ocean on time scales approaching real-time need to be designed accordingly. 2) Surface currents and variable ship traffic logistically complicate repeated acquisition over the same seafloor-referenced location and require specialized, often expensive, acquisition schemes.

With these challenges in mind, we take advantage of seismic acquisition redundancy to introduce a processing scheme which separately processes seismic data from different offset groups. If acquisition signal quality is sufficient, only a subset of the full streamer is needed to represent a region of the ocean in two spatial dimensions, with each successive offset group passing over any given point at a later time, thus preserving temporal snapshots of a progressively changing ocean.

3.2 - Data acquisition

The seismic data were acquired in August 1993 as part of the tectonic study to image the Iberian-Atlantic Margin (IAM). Data showed strong reflections within the water column leading to multiple publications (e.g. Biescas et al. [2008], Krahmann et al. [2008], Buffett et al. [2009], Pinheiro et al. [2010]). Data for this analysis were acquired off the Western Iberian Margin (Figure 3.1, line IAM-11).

3.3 - Processing scheme

The methodology used in this experiment differs from most where one image is created from all the streamer's offsets, thus optimizing the signal-to-noise ratio. We use subsets of the data offsets to generate seven temporally spaced images of the same acoustic impedance interfaces as the streamer passes over it. The number of images possible to create depends on the data quality (signal-to-noise ratio) and the frequency of repetition of the source, as well as the more obvious streamer length and vessel speed. This is

because so-called seismic 'stacks' are the result of summing together all seismic traces within a given offset range. The inherent redundancy of this method means there are many traces that represent the same depth-points, but from different angles (Figure 3.2). The summing together (stacking) of these common-depth-point (CDP) traces improves the signal-to-noise ratio by constructively boosting signal content and deconstructively cancelling random noise. The longer the offset range, the better the statistics available for noise cancellation. We chose 500 m offsets for this study because they allowed us to create seven images, while preserving for the most part the signal integrity.

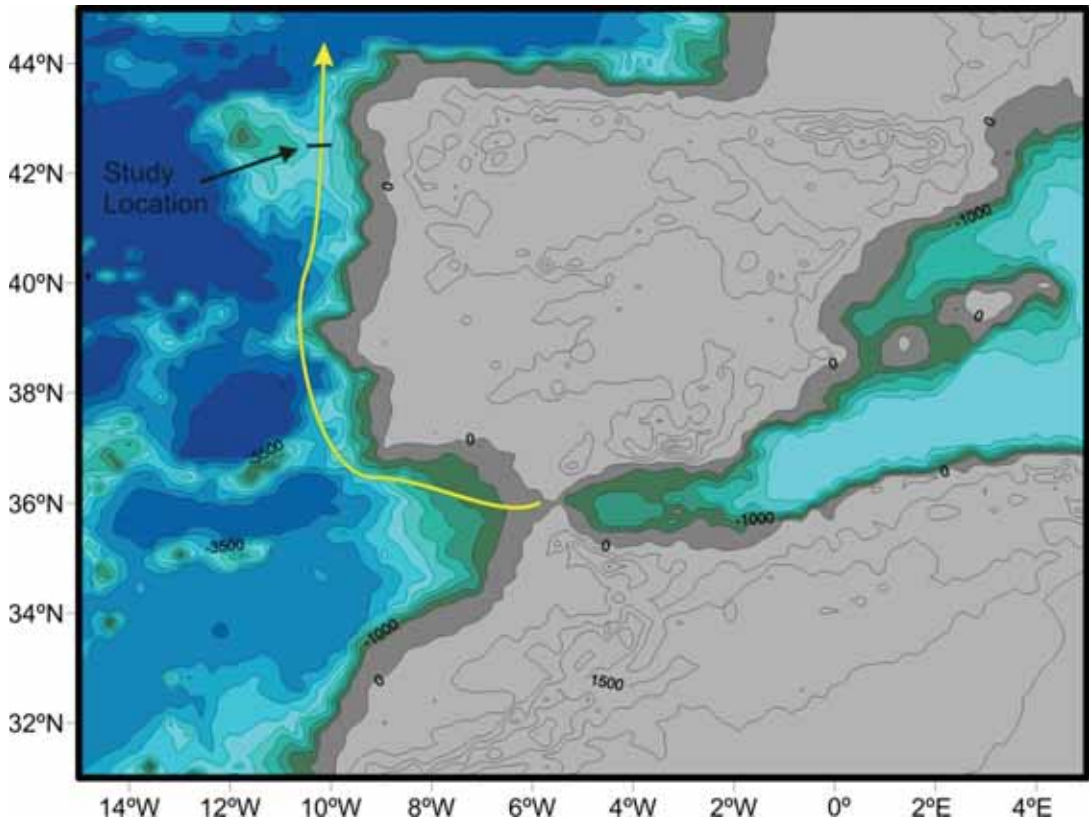

Figure 3.1 - Location of seismic section (small black line). Yellow line shows the approximate path of the Mediterranean Undercurrent

Considering the motion of the ship relative to the sea floor we re-sort the seismic data, first by CDP and secondarily by the appropriate 500 m offset range. Next we attempted to eliminate possible other factors that could account for apparent thermohaline

fluctuations. This consisted of compensation for frequency loss with offset, which permits each successive offset range a progressively lower dominant frequency due to the filtering effect of the receiver at large incident angles (thus, longer raypaths).

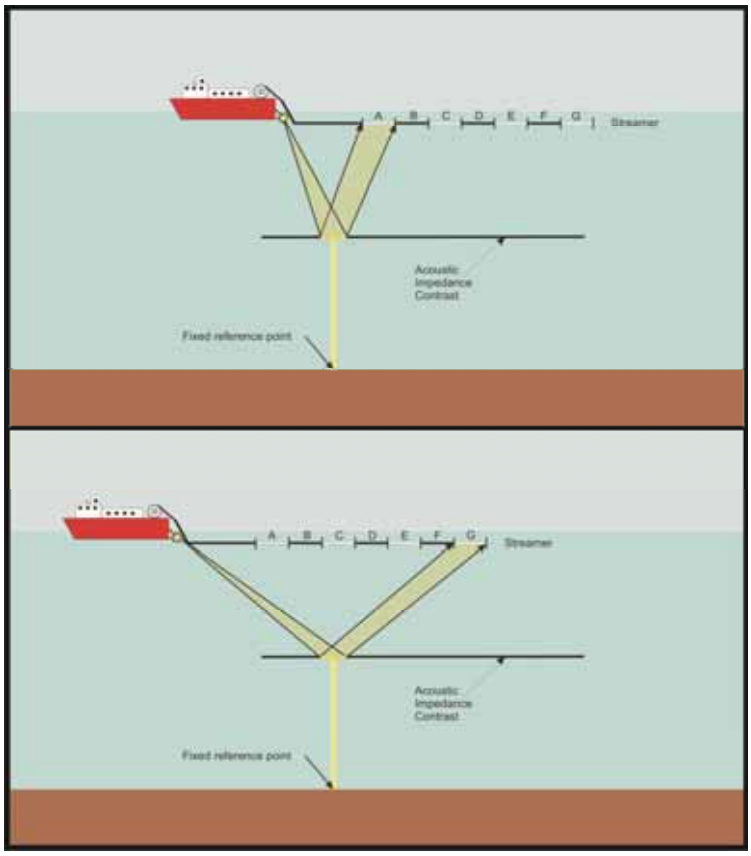

Figure 3.2 - Schematic diagram showing the first and last streamer offset group imaging the same oceanic structure over a fixed reference point.

3.4 - Results

The result is a series of seven images of the same water column, but at progressively later times, showing what we assert to be movement of thermohaline fine structure from frame to frame (Figure 3.3 and Appendix III). Two interpretation boxes are presented to emphasize some of the subtle fluctuation detail. Box 1 shows an M-shaped structure in panels A and B (500-1000 m; 1000-1500 m, offsets respectively), which becomes distorted in panels C and D (1500-2000 m; 2000-2500 m, offsets respectively), then appears to become restored in panels E, F and G (2500-3000 m; 3000-3500 m; 3500-

4000 m, offsets respectively). Box 2 displays a small layered structure. The lower-most undulating red reflector in panel A, begins to ramp-up in the centre of panels B and C, then becomes progressively flatter in panels D, E and F. In panel G, it shows an apparent sub-vertical discontinuity through its center.

3.5 - Verification against synthetic seismic data

The purpose of this test was to verify the processing scheme where there is zero fluctuation in thermohaline finestructure, namely, for synthetic data. The synthetic data were created using an explicit time-domain solver (called *ADER-DG*) based upon a discontinuous Galerkin method. Reflection coefficients for synthetic seismic data were generated from sound speed profiles derived from CTD (conductivity-temperature-depth) data collected during the GO (Geophysical Oceanography) project. Given that sound speed is by far the dominant factor influencing reflection coefficient [Sallarès et al., 2009] this provides a static representation of thermohaline finestructure at the location of the CTD casts. The solutions to generate the sections were obtained to a 4th order accuracy in space and time, on an unstructured triangular mesh of about 20,000 elements. The simulations were carried out on 10 processors of a Linux computing cluster. The synthetic data shot records were then processed using the same processing flow as the real data, but by creating five stacked sections from different offset groups.

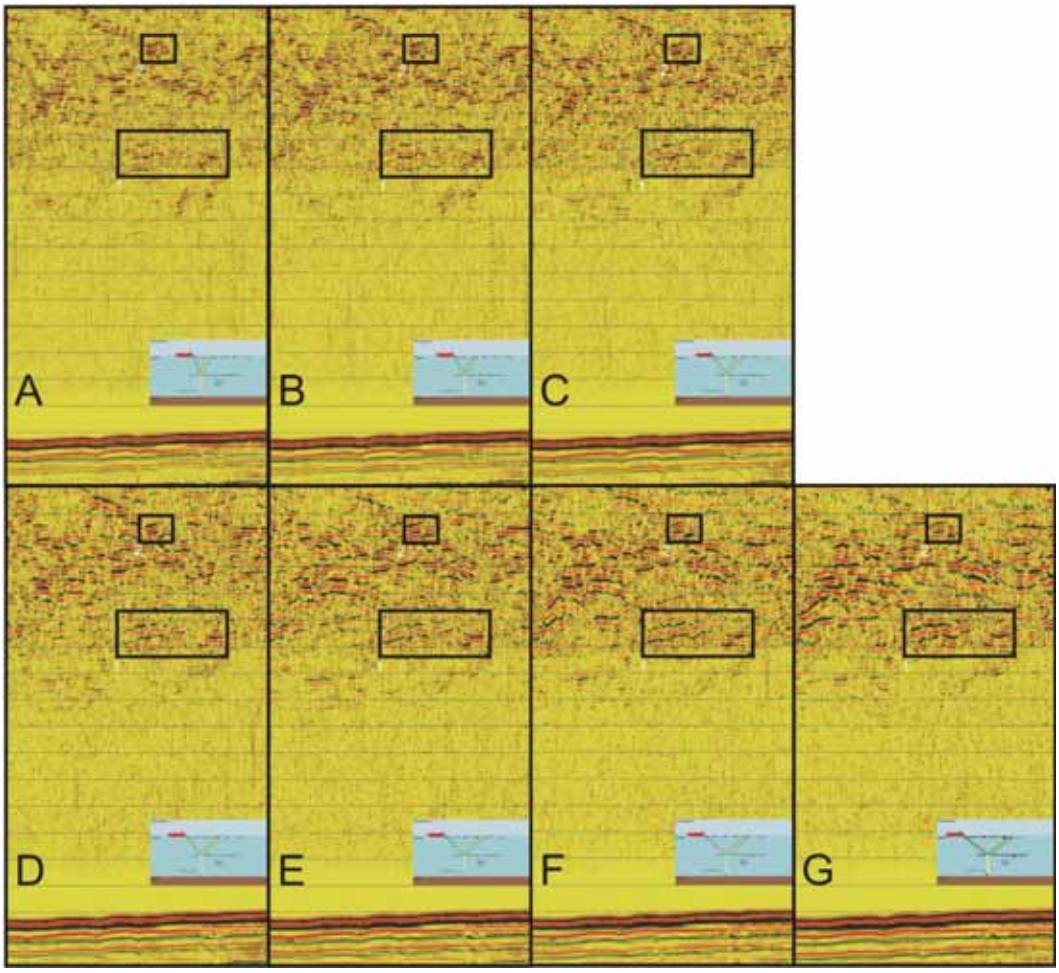

Figure 3.3 - Seismic stacks of the same geographical location (Figure 3.1) created with different sections of the recording streamer (see insets). Time step between animation frames based on ship velocity is approximately 3.5 min. Horizontal distance is 12.5 km and depth ranges from 800 m to 2000 m at the sea floor. Offset ranges are: A) 500-1000 m; B)1000-1500 m; C)1500-2000 m; D)2000-2500 m; E)2500-3000 m; F)3000-3500 m; G)3500-4000 m. This figure is available as a fold-out in Appendix III at a higher resolution

The effect of frequency loss with 'offset' can be seen in the synthetic data, where there are no real motions (Figure 3.4). This artifact causes an apparent shift from left to right of the seismic traces with each movie frame. Notice how the synthetic data grow progressively in wavelength, but show no intra-reflector variability like the real data.

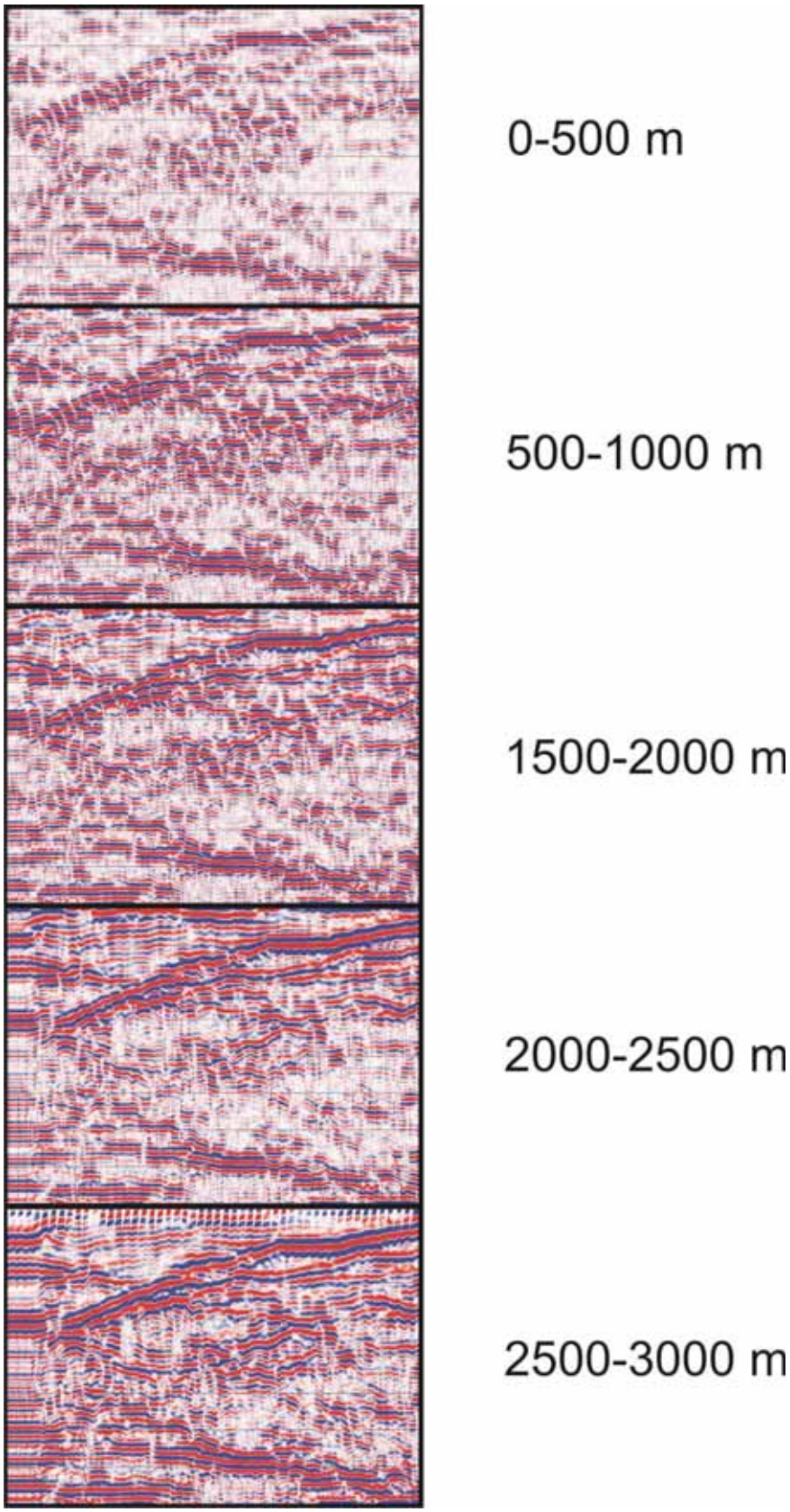

Figure 3.4 - Synthetic data generated from XBT/CTD sound speed model. Note the decrease in signal frequency content seen as the 'thickening' of reflectors. However, there are no intra-reflector motions as seen in the real data.

3.6 - Discussion − proof of concept

The method used in this paper employs the separation of data recorded at different offset groups of a seismic streamer to create unique stacked sections which are spaced temporally at 3.5 minute intervals. Each progressive section in time shows changes in the reflectivity pattern of thermohaline finestructure in a way which cannot be dismissed as simply an artifact of seismic data processing. This is true for two reasons: a) the synthetic data tested, as expected, show no changes in the reflectivity pattern other than the reduction of frequency content consistent with how higher frequencies are attenuated as a function of source-receiver distance (offset) (i.e. longer travel paths). Thus, frames 1-5 show an apparent steady 'motion' from left to right caused by each frame having lower frequency content and the wavelet shape growing accordingly. However, intra-reflector changes seen in the real seismic oceanography data are not present in the synthetic data. b) comparison of the seafloor reflectivity and the thermohaline reflectivity of the real data show the same difference as the synthetic: that is, the seafloor, being static on time scales of ocean dynamics, does not show the same reflectivity fluctuations as the ocean. These two independent observations indicate that it is most probable that the fluctuations observed in the real data are actual near real-time displacements of isopycnals such as those caused by internal waves, which travel at velocities of the order 1 ms^{-1} [Thorpe, 2005]. Considering a velocity of 1 ms^{-1} and for each 3.5 minute time step, it is plausible that fluctuations are on the order of 200 m, movements that are easily observable on seismic data which have typical resolutions on the order of 10 m.

However, it is virtually impossible given the limited dataset, to quantify the velocity of the observed internal waves using this method alone. This is because of a number of reasons. The motion of the ship at the surface leads to a Doppler-like effect. That is,

$$\lambda_{mod} = \frac{v_{ship}\lambda_{true}}{(v_{ship} - v_{water})} \quad , \qquad \text{eq. 3.1}$$

where v is velocity and λ is wavelength [Vsemirnova et al., 2009b]. Furthermore, in this dataset we do not have an independent measurement of the wavelength of internal waves (λ_{true}). Finally, the velocity vector of the internal wave does not likely point

conveniently in the direction of the acquisition, rather, it is highly likely to have an out-of-plane component. However, we can say that the real data processed in this research show fluctuations in thermohaline finestructure at depths between 800 m and the seafloor, while the same fluctuations are not observed in either the seafloor (which we assume to be static - Figure 3.3) or the synthetic data (which are by their nature, static - Figure 3.4).

In addition to the unknown velocities or wavelengths of the internal waves, one chief limitation of this method is the trade-off necessary between maximizing CDP fold and maximizing the number of stacks (frames) necessary to temporally image variable thermohaline fine structure. The data used in this study were of rather good signal quality and utilized a long streamer (5.5 km, of which 4.0 km was utilized). But a longer streamer would allow more stacks to be created without reducing the offset range needed to optimize the signal-to-noise ratio. This study, nonetheless shows proof-of-concept.

Potential falsification of the validity of this method could come about by acquiring coincident and simultaneous independent measurements of local internal waves (by using a lowered acoustic Doppler current profiler, for example), or, seismically, but designing an acquisition scheme such as using a buoyed and anchored streamer of a given length at a fixed depth while doing repeated passes of a conventional airgun source, similar in geometry to a roll-on, roll-off land seismic survey. This would position the streamer over a fixed seafloor position and thus enable higher-fold measurements of changing thermohaline finestructure. Ideally, this would be done in a region of minimal surface currents, but significant undercurrents, high temperature/salinity contrasts and low ship traffic, such as the area imaged herein (Figure 3.1). This area was chosen because of the good data set (Iberian Atlantic Margin data) and the observed decay in laminar finestructure and increased disturbance of isopycnals downstream of the Mediterranean Undercurrent [Buffett et al., 2009], indicating mixing, thus thermohaline finestructure variability. In areas where there are statically stable isopycnals (thermohaline staircases, for example), observing motion on the time scale of the passing of a streamer would be increasingly difficult.

3.7 - Conclusions

By devising a processing scheme to make use of a long streamer as it passes over a fixed geodetic point, we are able to generate sets of stacked seismic data from different offset groups. In theory, if thermohaline finestructure is sufficiently dynamic, each offset group would 'see' spatial and temporal changes to finestructure. The results of our analysis point to the observed thermohaline fluctuations as related to the motion of the oscillating internal wave field, although we have no independent or simultaneous observational data. Support for our deduction comes from two observations: a) that the sea floor reflectors in the same seismic section do not fluctuate in the same manner as the ocean, and b) that when the same processing scheme was applied to synthetic data, there were no noticeable intra-reflector motions. All three data sets (thermohaline, sea floor and synthetic) show a lowering of frequency content with offset. While this was partially compensated for in the processing flow, more work needs to be done to completely remove this effect as it masks somewhat the true movement of the dynamic ocean. Even so, this effect does not fatally flaw the methodology because while all three data sets show the offset effect, only the thermohaline finestructure varies in an apparent random manner. Both the sea floor and synthetic data show only the lowering of frequency content as a function of offset and are otherwise stable, as expected intuitively. These observations coupled with typical internal wave speeds, implicate the causality of the latter as the source of the fluctuations.

References

Blacic, T.M. and W.S. Holbrook, 2009. First images and orientation of fine structure from a 3-D seismic oceanography data set, *Ocean Sci.*, **6**, pp. 431-439.

Buffett, G.G., Biescas, B., Pelegrí, J.L., Machín, F., Sallarès, V., Carbonell, R., Klaeschen, D., and Hobbs, R.W., 2009. Seismic reflection along the path of the Mediterranean Undercurrent, *Cont. Shelf Res.*, **29**, pp. 1848–1860, doi:10.1016/j.csr.2009.05.017.

Buffett, G.G., C.A. Hurich, E.A. Vsemirnova, R.W. Hobbs, V. Sallarès, R. Carbonell, D. Klaeschen, and B. Biescas, 2010. Stochastic Heterogeneity Mapping around a Mediterranean salt lens, *Ocean Sci.*, **6**, pp. 423-429.

Chadwick, R.A., Arts, R. & Eiken, O. 2005. 4D seismic imaging of a CO_2 plume. In: Doré, A. G. & Vining, B.A. (eds) Petroleum Geology: North-West Europe and Global Perspectives—Proceedings of the 6th Petroleum Geology Conference, 1385–1399. Petroleum Geology Conferences Ltd.

Cheng, X., Time-lapse imaging of fault properties at seismogenic depth using repeating earthquakes, active sources and seismic ambient noise, *Ph.D. thesis*, ISBN: 9781109217353.

Géli, L., E. Cosquer, R.W. Hobbs, D. Klaeschen, C. Papenberg, Y. Thomas, C. Menesguen, and B.L. Hua, 2009. High resolution seismic imaging of the ocean structure using a small volume airgun source array in the Gulf of Cadiz, *Geophys. Res. Lett.*, **36**, L00D09, doi:10.1029/2009GL040820.

Holbrook, W.S., P. Páramo, S. Pearse, and R.W. Schmitt, 2003. Thermohaline fine structure in an oceanographic front from seismic reflection profiling, *Science*, **301**, pp. 821–824.

Lumley, D., 2001. Time-lapse seismic reservoir monitoring, *Geophysics*, **66**(1), pp. 50–53.

Pinheiro, L., H. Song, B. Ruddick, J. Dubert, I. Ambar, K. Mustafa, R. Bezerra, 2010. Detailed 2-d imaging of the Mediterranean outflow and meddies off w Iberia from multichannel seismic data. *J. Mar. Sys.*, **79**, pp. 89–100.

Stommel, H. and K.N. Federov, 1967. Small scale structure in temperature and salinity near Timor and Mindanao, *Tellus* **19**, pp. 306-325.

CHAPTER 4

Research Letters

Pouring forth its seas everywhere, then, the ocean envelops the earth and fills its deeper chasms.

-- Nicolaus Copernicus

4.1

Imaging meddy finestructure using multichannel seismic reflection data

Imaging meddy finestructure using multichannel seismic reflection data

B. Biescas,[1] V. Sallarès,[1] J. L. Pelegrí,[2] F. Machín,[2] R. Carbonell,[3] G. Buffett,[3] J. J. Dañobeitia,[1] and A. Calahorrano[2]

Received 13 March 2008; revised 16 April 2008; accepted 2 May 2008; published 14 June 2008.

[1] This work illustrates the great potential of multichannel seismic reflection data to extract information from the finestructure of meddies with exceptional lateral resolution (10–15 m). We present seismic images of three meddies acquired in the Gulf of Cadiz (SW Iberian Peninsula), which consist of concentric reflectors forming oval shapes that sharply contrast with the background oceanic structure. The seismic images reveal the presence of different regions within the meddies that are consistent with those observed in historical temperature (T) and salinity (S) data. The core region, characterized by smooth T and S variations, is weakly reflective. The double-diffusive upper and lower boundaries and the lateral-interleaving outer edges, characterized by stronger T and S contrasts, display strong reflectivity bands. These new observations clearly show differences between layers developed at the upper and lower boundaries that can contribute to the knowledge of mixing processes and layering formation in oceans. **Citation:** Biescas, B., V. Sallarès, J. L. Pelegrí, F. Machín, R. Carbonell, G. Buffett, J. J. Dañobeitia, and A. Calahorrano (2008), Imaging meddy finestructure using multichannel seismic reflection data, *Geophys. Res. Lett.*, *35*, L11609, doi:10.1029/2008GL033971.

1. Introduction

[2] The warm and salty Mediterranean water spills over the Strait of Gibraltar (Figure 1), sinks and flows westwards along the continental slope of the South Iberian margin, forming the so-called Mediterranean Undercurrent (MU) [*Ambar et al.*, 2002]. During its journey along the margin, the MU experiences abrupt topographic changes like major canyons, causing boluses of Mediterranean water to separate from the MU in the form of ~40–100 km wide, ~1 km thick, vertically extending between ~500 and 1500 m depth, coherent clockwise-rotating lenses called meddies [*Richardson et al.*, 2000]. Generally, meddies translate first to the west and then drift southwestwards near Cape St Vincent towards the Canary basin with translation speeds of a few cm/s and anti-cyclonic rotation periods of 4 to 6 days [*Richardson et al.*, 2000]. During the life of a lens, the Mediterranean water slowly mixes with the surrounding Atlantic water and salt anomalies progressively weaken until the meddy dissipates. Meddies may last for about 2 years and cover distances up to one thousand km [*Armi et al.*, 1989; *Richardson et al.*, 1989, 2000].

[1]Unitat de Tecnologia Marina CSIC, Barcelona, Spain.
[2]Institut de Ciències del Mar CSIC, Barcelona, Spain.
[3]Institut de Ciències de la Terra Jaume Almera CSIC, Barcelona, Spain.

0094-8276/08/2008GL033971$05.00

[3] The existing information on the internal structure and dynamic processes taking place within meddies is mainly based on data acquired using classical oceanographic instrumentation with a lateral resolution of $\mathcal{O}$(1 km). In their pioneering work, *Holbrook et al.* [2003] showed that marine multichannel seismic (MCS) data, designed and used to obtain structural images of the Earth's subsurface, also display coherent reflections from within the water layer. Thanks to signal redundancy provided by the multiple fold of a single reflector point, MCS systems enhance coherent signals over noise, resulting in clear acoustic images of the oceanic thermohaline structure with a lateral resolution of $\mathcal{O}$(10 m). Based on Holbrook and coworkers' images, as well as on his own results, *Ruddick* [2003] pointed at the potential of MCS data to image the finestructure that is likely to develop at the bounds of meddies owing to double-diffusion vertical mixing (upper and lower bounds) and interleaving (lateral bounds).

[4] In this work we confirm the potential of MCS data to locate meddies and to image their internal structure with great detail by showing three spectacular MCS images of complete meddies that reveal a number of significant features, including the distribution of finestructure with lateral and vertical resolution of 10–15 m.

2. Data Acquisition and Processing

[5] The MCS data used in this work were acquired in the Gulf of Cadiz in the framework of the Iberian-Atlantic Margin (IAM) survey [*Torné et al.*, 1995] that took place in August–September 1993 (Figure 1a). IAM data were recorded using a 4800 m long HSSQ/GX600 analogue streamer with 192, 25 m-spaced channels, giving a common depth point (cdp) spacing (i.e., a lateral sampling) of 12.5 m. The seismic source was an airgun array composed of 36 BOLT guns with a total volume of 7524 cu. in. and a peak energy in the frequency band of 20–50 Hz that were fired with a pop interval of 75 m. The theoretical vertical resolution of seismic reflection systems is considered to be a quarter of wavelength [*Yilmaz*, 2001], although this resolution is rarely achieved since it is affected by factors such as the thickness of the reflecting horizon and the sharpness of the boundary between the media. Therefore the vertical resolution is more realistically on the order of one half of wavelength, i.e., ~15 m for the highest IAM's source frequency.

[6] We fully reprocessed some of the IAM profiles with the aim of obtaining the best possible images of the water column. The processing sequence consisted of the following six steps [*Yilmaz*, 2001]: (1) Bandpass frequency filter between 5 and 120 Hz and spherical divergence gain

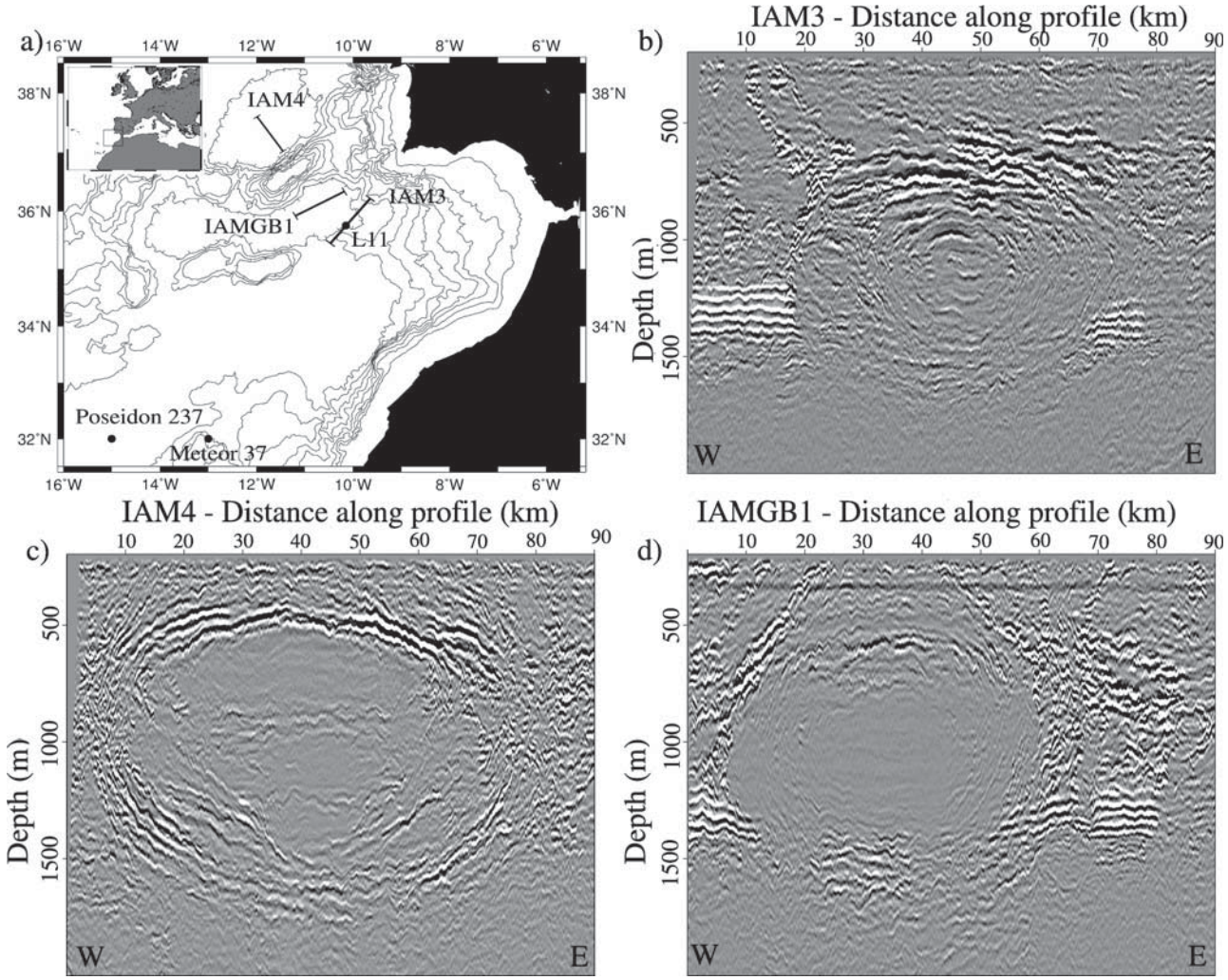

Figure 1. (a) Map showing the geographical location of the study zone. Lines indicate the position of the MCS profiles that were reprocessed in the present work, acquired during the IAM survey in autumn 1993. Black dots correspond to the location of CTD probes acquired in the framework of the CANIGO project during winter 1997 (Meteor 37), spring 1998 (Poseidon 237) and autumn 1997 (L11). MCS images of profiles (b) IAM3 on August 31st, (c) IAM4 on August 29th and (d) IAMGB1 on September 7th.

correction. (2) Median subtraction-filter to remove the direct wave. The direct wave, which travels from source to receiver without being reflected is, by far, the most energetic one and masks shallow-water reflections. It is thus important to eliminate this phase without removing the reflected ones. (3) Velocity analysis. (4) High order normal moveout correction. (5) Stacking of cdp-sorted traces with offsets larger than 600 m to mitigate the direct wave in the near-offset field, where median filtering is less efficient. And (6) Post-stack Kirchhoff time migration.

[7] Seismic data (Figures 1b, 1c, and 1d) contain indirect information on magnitudes of oceanographic interest other than purely morphological. The seismic reflection coefficient, or amplitude ratio of the reflected vs. incident waves, is proportional to the contrast in acoustic impedance (sound speed times density) between two contacting media (thicker than ~15 m in our case) [*Sheriff and Geldart*, 1982]. Insofar as density and velocity are primarily a function of temperature and salinity [*Munk et al.*, 2003], seismic reflectors and their amplitudes must be coherent with, and provide information on, the finestructure in terms of salinity and temperature contrasts [*Nandi et al.*, 2004]. With the purpose of exploring the correspondences between seismic and oceanographic data, we compiled a number of existing conductivity-temperature-depth (CTD) profiles that sampled meddies (Figure 1a). These CTDs were acquired during the Canary Islands, Azores and Gibraltar Observations (CANIGO) project [*Parrilla et al.*, 2002], and the meddies are thus other than the seismically imaged ones.

3. Results: Imaging Meddy Finestructure

[8] Three out of ten IAM MCS profiles reprocessed in the course of this work show prominent meddy-like features, i.e., large oval-shaped structures outlined by a series of concentric seismic reflectors with lateral diameters of some 50–80 km and vertical thickness of 1000–1500 m, centered at a depth of ~1000 m, which sharply contrast with the background acoustic ocean's structure (Figure 1). Table 1 displays some properties of the upper and lower reflectors,

Table 1. Number of Digitized Reflectors, Mean Length, Maximum Length, Maximum and Minimum Amplitudes of Acoustic Reflectors in the Upper and Lower Boundaries of Meddies IAM3, IAM4 and the Lower Boundary of IAMGB1

Meddy	Num. Digitized Reflectors	Mean Length (km)	Max. Length (km)	Max. Amp. Counts	Mean Amp. Counts
IAM3 [500–1000]m	18	8.8	19	20	1.5
IAM3 [1400–1700]m	30	2	5.1	4.5	0.5
IAM4 [400–600]m	10	15.1	32.7	20	1
IAM4 [1200–1800]m	76	2.9	10.6	5.5	0.5
IAMGB1 [1200–1800]m	60	2.6	7.1	7	0.5

such as their maximum and mean lengths and seismic signal amplitudes.

[9] The meddy found along profile IAM3 (Figure 1b) is the smallest. Considering dimensions based on the concentric seismic reflectors, this meddy is ~50 km wide and spreads between 700 m and 1600 m. It is noteworthy that IAM3 is the only one of the three meddies in which seismic reflectors are observed throughout the whole structure, from the boundary zone to the central region. The reflective bands that delineate the upper boundary show maximum length of ~19 km and vertical separations between single reflectors of ~40–60 m, while the lower ones show shorter lateral lengths (~5 km) and more variable vertical separations (20–50 m). The meddy seismic imaged in the IAM4 profile (Figure 1c) has a diameter of 80 km and extends from 400 m to 1800 m depth. The concentric reflectors outlining the meddy are located on the perimeter and do not extend toward the core region. The center of the meddy shows a band of horizontal reflectors at about 900 m depth, which appear to separate two nearly acoustically invisible cores. The reflective layers on the upper edge spread over a ~100 m thick band, with maximum length of ~32 km and vertical separations of about 40–50 m between single reflectors, while in the lower edge the high-reflectivity band is ~400 m thick, reflectors have much shorter lateral lengths and more variable vertical separation (20–50 m). Finally, the seismic image of the meddy in the IAMGB1 line (Figure 1d) has a diameter of ~60 km and a vertical thickness of 1500 m. The geometry of the lateral layers suggests that the top of the meddy could be located in the shallowest ~100 m depth, where we do not have good quality acoustic data because of the direct wave distortion. However, there is no observation of a meddy T and S anomaly extending to the surface, thus there might be another process that accounts for these lateral and shallow reflections. Some strong reflectors can be observed at ~600 m depth; nevertheless, it is difficult to determine if they distinguish two different cores or they actually form the upper boundary of a single core that has a dome-shaped structure on top. The lower boundary is ~400 m thick and shows relatively short reflective layers with vertical separation of ~20–40 m. The flat line observed at ~400 m depth along all the seismic image corresponds to the direct wave, which could not be totally removed by the median filter.

4. Discussion

[10] The presence of differentiated, well-defined, temporally-evolving regions within meddies was first suggested based on data acquired during the repeated sampling of a meddy called Sharon that was tracked for two years in the eastern North Atlantic subtropical gyre [*Armi et al.*, 1989; *Richardson et al.*, 1989; *Ruddick*, 1992; *Hebert et al.*, 1999]. Sharon was characterized by a single central core with very weak spatial thermohaline gradients, that was surrounded by well-developed finestructure. The structure above and below the core was suggested to be caused by double-diffusive vertical mixing while the layering on its lateral bounds was attributed to double-diffusive intrusions.

[11] The seismic snapshots of meddies IAM4 and IAMGB1 are in relative agreement with the oceanographic description in what concerns the core region, since they clearly show a central region with very weak reflectivity. Meddy IAM4 has two cores that are located at the two levels of the Mediterranean outflow water (800 and 1200 m) [*Ambar et al.*, 2002]. Both cores are separated by the reflection layers visible at about 950 m, the shallow one being dome-shaped and the deep core having an inverted dome-shaped. Meddy IAMGB1 could have a single or double-core, actually indistinguishable in the seismic image because of the lateral reflectors extend towards the surface. In contrast, meddy IAM3 does not show an acoustically transparent core. It appears rather to have quite well developed finestructure that reaches almost to its center. This feature, together with the relatively small apparent radius of meddy IAM3 (~25 km), suggests two possible explanations: that the seismic snapshot may have crossed it quite away from its center, at a position in the outer intrusively-mixed region, or that it is an old meddy so that lateral intrusions had worked their way into its center.

[12] Seismic data (Figure 1 and Table 1) reveal that both the upper and lower boundary layers have strong reflectivity, consistent with the existence of finestructure, but suggest significant differences between these regions. The upper boundary zone is relatively thin (~100–200 m), has a few layers that show high lateral coherence and high reflection amplitudes. The vertical separation between layers are slightly longer (~40–60 m) than those observed in the lower boundary. The lower boundary is relatively thick (~300–400 m) and has many, relatively short, layers with a vertical spacing of ~20–50 m and low reflection amplitudes.

[13] Besides MCS data, we have also analyzed available historical oceanographic CTD data that sampled three meddies during different surveys carried out in the Gulf of Cadiz and Canary Basin. To allow qualitative comparison, Figure 2 displays the oceanographic data calculated from the CTD L11 station and the seismic reflections recorded through the center of meddy IAM3. Temperature and salinity data (Figures 2a and 2b) display the main regions of the meddy, which can also be recognized from the acoustic reflectors (Figure 2e). The CTD-L11 data show a double-core meddy with an upper core between 800 and 1000 m depth and a lower core between 1000 and 1300 m depth. Within the core regions, where temperature and

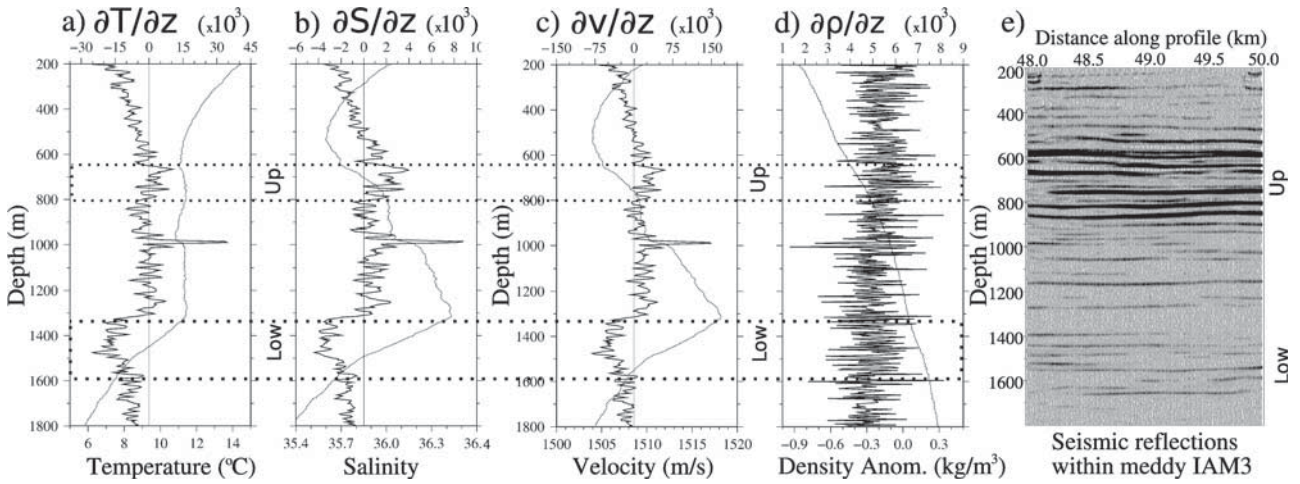

Figure 2. The 5-m smoothed profiles of (a) temperature (dotted line) and temperature gradient (black line), (b) salinity (dotted line) and salinity gradient (black line), (c) sound speed (dotted line) and sound speed gradient (black line), and (d) density anomaly (here defined as in situ density minus density of standard meddy water, i.e., $\rho(S, T, p) - \rho(S = 35, T = 10°C, p)$ (dotted line) and density gradient (black line) obtained from the CTD probes through the meddy observed during L11. (e) Seismic reflections recorded through the center of meddy IAM3. Geographical locations of the data are shown in Figure 1a.

salinity reach maximum values (T > 15°C, S > 36.4), gradients become weaker, while in the intrusive regions, where acoustic reflectors become stronger, temperature and salinity gradients reach maximum values. Since acoustic impedance of a media is the product of sound speed and density, we have calculated these magnitudes from CTD data using *Fofonoff and Millard* [1983] and *Millero et al.* [1980] algorithms. The differences between the upper and lower meddy reflectors are consistent with observed differences in the sound speed profiles (Figure 2c). The relatively thin (∼150 m) upper boundary is characterized as having just a few large peaks in the sound speed gradient (>±50 · 10^3 s^{-1}), with large vertical spacing between peaks (∼30–40 m). The relatively thick lower boundary (∼300 m), on the contrary, has many more large sound speed gradient peaks, and the vertical spacing between peaks is small (∼10–30 m). Velocity gradients dominate the acoustic signal since $\rho\partial v/\partial z$ is typically one order of magnitude greater than $v\partial\rho/\partial z$. However, results show that density gradients (Figure 2d) are slightly higher on the core boundaries, where acoustic signal is stronger.

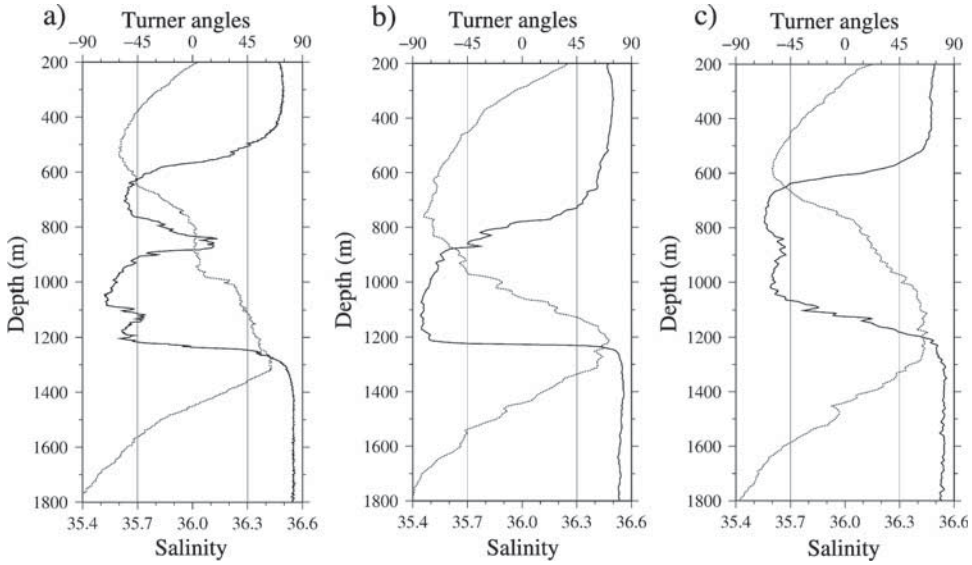

Figure 3. Turner angles (black lines) and salinity profiles (grey lines) as obtained from the CTD through the meddies observed during (a) L11, (b) Meteor 37, and (c) Poseidon 237. Turner angles are practical indicators that differentiate regions prone to diffusive convection ($-90° < Tu < -45°$) and salt finger instability ($45° < Tu < 90°$) from stable regions ($|Tu| < 45°$). Turner angles were calculated, after smoothing the data with a 50 m running vertical window, using the method proposed by *Ruddick* [1983]. Geographical locations are shown in Figure 1a.

[14] One likely explanation for the observed differences between the upper and lower intrusive regions is the different dynamical processes that control their formation and development. Double-diffusive fluxes, base on the molecular heat diffusion being much greater than molecular salt diffusion, can break relatively smooth thermohaline gradients into steps and layers [*Ruddick and Gargett*, 2003]. *Ruddick* [1992] actually suggested that the upper boundary of meddies is dominated by diffusive convection, whereas the lower one is prone to salt fingering. Turner angles (Tu) [*Ruddick*, 1983] calculated from the CTD data, indeed show that the upper and lower bounds of all three CANIGO meddies are prone to diffusive-convection and salt-fingers, respectively, while their core regions are double-diffusively stable (Figures 3a, 3b, and 3c). The seismic images provide thus a very valuable two-dimensional view of the patterns that result from different regimes and should contribute to improve both phenomenological and numerical models of mixing and layering formation in geophysical fluids.

5. Conclusions

[15] Seismic oceanography is becoming a useful tool to investigate the internal structure of the water column. Multichannel seismic (MCS) data presented in this work corroborate the great potential of this method for studying oceanic processes. Focusing on meddy research, we may now affirm that the MCS method allows to detect these rotating salty lenses, while giving information on their dimensions, as well as the detailed vertical and lateral distribution and characteristics of finestructure. The main regions within a meddy, detected by classical oceanographic instrumentation are clearly observed in the seismic snapshots: (1) the upper boundary zone, characterized by the presence of a few, strong, laterally continuous reflectors, (2) the lower boundary zone, with more numerous shorter and 3–4 times weaker reflectors distributed into a thicker region, and (3) a very weakly reflective central core region. Our results show that powerful 36 BOLT guns array with a total volume of 7524 cu and low frequency (20–50 Hz) sources, such as those used in deep seismic surveys (DSS), are well-suited to image the oceanic finestructure. The unprecedented horizontal resolution of MCS data, two orders of magnitude better than typical oceanographic data, reveal lateral coherence characteristics of the finestructure that should considerably contribute to improving the models of ocean dynamic processes.

[16] **Acknowledgments.** This work was supported by the GEOCEAN Intramural Project (200530f081) funded by the Consejo Superior de Investigaciones Científicas. We are deeply grateful to Dirk Klaeschen for his help on the seismic processing. We also acknowledge the support of the GO Research Group (NEST-2003-1- Adventure FP6-015603) and the constructive suggestions of two anonymous reviewers.

References

Ambar, I., N. Serra, M. Brogueira, G. Cabeçadas, F. Abrantes, P. Freitas, C. Gonçalves, and N. González (2002), Physical, chemical and sedimentological aspects of the Mediterranean outflow off Iberia, *Deep Sea Res., Part II*, *49*, 4163–4177.

Armi, L., D. Herbert, N. Oakey, J. Price, P. Richardson, H. Rossby, and B. Ruddick (1989), Two years in the life of a Mediterranean salt lens, *J. Phys. Oceanogr.*, *19*, 354–370.

Fofonoff, P., and R. Millard (1983), Algorithms for computation of fundamental properties of seawater, *UNESCO Tech. Pap. Mar.*, *44*.

Hebert, D., N. Oakey, and B. Ruddick (1999), Evolution of a Mediterranean salt lens: Scalar properties, *J. Phys. Oceanogr.*, *20*, 1468–1483.

Holbrook, W., P. Páramo, S. Pearse, and W. Schmitt (2003), Thermohaline fine structure in an oceanographic front from seismic reflection profiling, *Science*, *301*, 821–824.

Millero, F., C. Chen, A. Bradshaw, and K. Schleicher (1980), A new high pressure equation of state for seawater, *Deep Sea Res., Part A*, *27*, 255–264.

Munk, W., P. Worcester, and C. Wunsch (2003), *Ocean Acoustic Tomography*, *Cambridge Monogr. Mech.*, vol. 56, 570 pp., Cambridge Univ. Press, Cambridge, U. K.

Nandi, P., W. Holbrook, S. Pearse, P. Páramo, and R. Schmitt (2004), Seismic reflection imaging of water mass boundaries in the Norwegian Sea, *Geophys. Res. Lett.*, *31*, L23311, doi:10.1029/2004GL021325.

Parrilla, G., S. Neuer, P. Le Traon, and E. Fernández-Suárez (2002), Canary Islands Azores Gibraltar Observations (CANIGO): Studies in the northern Canary Islands basin, *Deep Sea Res.* Part II, *49*, 3409–3413.

Richardson, P., D. Walsh, L. Armi, M. Schröder, and J. Price (1989), Tracking three meddies with SOFAR floats, *J. Phys. Oceanogr.*, *19*, 371–383.

Richardson, P., A. Bower, and W. Zenk (2000), A census of meddies tracked by floats, *Prog. Oceanogr.*, *45*, 209–250.

Ruddick, B. (1983), A practical indicator of the stability of the water column to double-diffusive activity, *Deep Sea Res., Part A*, *30*, 1105–1107.

Ruddick, B. (1992), Intrusive mixing in a Mediterranean salt lens: Intrusion slopes and dynamical mechanisms, *J. Phys. Oceanogr.*, *22*, 1274–1285.

Ruddick, B. (2003), Sounding out ocean fine structure, *Science*, *301*, 772–777.

Ruddick, B., and A. Gargett (2003), Oceanic double-infusion: Introduction, *Prog. Oceanogr.*, *56*, 381–393.

Sheriff, R., and L. Geldart (1982), *Exploration Seismology: History, Theory and Data Acquisition*, 253 pp., Cambridge Univ. Press, Cambridge, U. K.

Torné, M., M. Fernández, J. Carbonell, and E. Banda (1995), Lithospheric transition from continental to oceanic in the West Iberia Atlantic Margin, in *Rifted Ocean-Continent Boundaries*, *NATO ASI Ser. C*, vol. 463, edited by E. Banda, M. Torn, and M. Talwani, pp. 247–263, Springer, New York.

Yilmaz, O. (2001), *Seismic Data Analysis: Processing, Inversion, and Interpretation of Seismic Data*, vol. II, *Invest. Geophys.*, vol. 10, 2nd ed., 2027 pp., Soc. Explor. Geophys., Tulsa, Okla.

B. Biescas, J. J. Dañobeitia, and V. Sallarès, Unitat de Tecnologia Marina, Passeig Marítim de la Barceloneta 37-49, E-08003 Barcelona, Spain. (biescas@cmima.csic.es)

G. Buffett and R. Carbonell, Institut de Ciències de la Terra Jaume Almera CSIC, Lluís Sole Sabaris s/n, E-08028 Barcelona, Spain.

A. Calahorrano, F. Machín, and J. L. Pelegrí, Institut de Ciències del Mar CSIC, Passeig Marítim de la Barceloneta 37-49, E-08003 Barcelona, Spain.

4.2

Relative Contribution of Temperature and Salinity to Ocean Acoustic Reflectivity

Relative contribution of temperature and salinity to ocean acoustic reflectivity

V. Sallarès,[1] B. Biescas,[1] G. Buffett,[2] R. Carbonell,[2] J. J. Dañobeitia,[1] and J. L. Pelegrí[3]

Received 22 July 2009; revised 2 September 2009; accepted 23 September 2009; published 23 October 2009.

[1] Marine seismic data display laterally coherent reflectivity from the water column that is attributed to fine-scale oceanic layering. The amplitude of the different reflections is the expression of acoustic impedance contrasts between neighbouring water masses, and therefore water reflectivity maps the ocean's vertical sound speed and density (i.e., temperature and salinity) variations. Here we determine the relative contribution of each parameter by computing the temperature and salinity partial derivatives of sound speed and density, and using them to estimate reflection coefficients from a real oceanographic dataset. The results show that the mean contribution of density variations is 5–10%, while 90–95% is due to sound speed variations. On average, 80% of reflectivity comes from temperature contrasts. Salinity contribution averages 20%, but it is highly variable and reaches up to 40% in regions prone to diffusive convection such as the top of the Mediterranean Undercurrent in the Gulf of Cadiz. **Citation:** Sallarès, V., B. Biescas, G. Buffett, R. Carbonell, J. J. Dañobeitia, and J. L. Pelegrí (2009), Relative contribution of temperature and salinity to ocean acoustic reflectivity, *Geophys. Res. Lett.*, *36*, L00D06, doi:10.1029/2009GL040187.

1. Introduction

[2] Multichannel seismics (MCS) is a widely used tool for geological prospection of the Earth's subsurface. Marine MCS systems are constituted of a source, generally an airgun array, and a line of closely spaced hydrophones, or channels, called a streamer that are towed behind a vessel. The airguns are fired at constant intervals, the seismic wavefield propagates through the medium, scatters back, and is recorded by the streamer. The seismograms recorded in the different channels are then ordered, processed and stacked to generate laterally coherent images of the different reflecting discontinuities, whose amplitude is proportional to the impedance (sound speed × density) contrast across the discontinuity. The basic ''convolutional model'' for seismic reflection data shows that seismic traces can be interpreted as the convolution of the source wavelet with the medium's elementary reflection coefficients [e.g., *Sheriff and Geldart*, 1995]. The vertical resolution of the seismic data depends therefore on the source used, and its capacity to distinguish between two adjoining layers is given by the Rayleigh criterion of a quarter of the dominant wavelength [*Widess*, 1973].

[3] *Holbrook et al.* [2003] showed that marine MCS data display reflectivity not only from solid Earth interfaces but also from within the water column. Practically, this indicates that the seismic systems are sensitive to the vertical sound speed and/or density variations of the ocean's interior. This observation has in the recent years given rise to a number of studies showing seismic images of water mass fronts and currents [e.g., *Tsuji et al.*, 2005], and mesoscale features such as Meddies [*Biescas et al.*, 2008] or the Mediterranean Undercurrent [*Buffett et al.*, 2009]. The central frequency of the seismic sources used in most of these experiments range between ∼20 Hz and ∼100 Hz, so its effective vertical resolution is on the order of ∼10 m. This is the approximate vertical dimension of oceanic fine structure, present in most of the world's oceans and whose origin has been attributed to a variety of physical phenomena such as double-diffusion [e.g., *Ruddick and Gargett*, 2003]. In parallel, it has been shown that there is a good correlation between ocean's reflectivity and vertical temperature gradient [*Nandi et al.*, 2004; *Nakamura et al.*, 2006], and that wave number spectra of ocean seismic reflectors agrees with Garrett-Munk model spectra of internal wave displacements [*Holbrook and Fer*, 2005; *Krahmann et al.*, 2008]. All these observations have sparked interest in the technique within the physical oceanographic community.

[4] Although it is now clear that the ocean's seismic reflectivity is due to acoustic impedance contrasts associated with oceanic fine structure, there is an ongoing debate concerning the relative contribution of the water's physical properties to this reflectivity, key to understand what is the information of oceanographic interest that can be extracted from seismic data. Most estimations made to date are based on waveform analysis of isolated XBT (expandable bathythermograph)-derived hydrographic profiles, suggesting that the contribution of sound speed (v) is the major factor as compared with that of density (ρ) [e.g., *Nandi et al.*, 2004; *Krahmann et al.*, 2008], and changes in temperature dominate in turn those of salinity. A first attempt to calculate this relative contribution was made by *Ruddick et al.* [2009], who used the expressions of *Lavery et al.* [2003] for the partial derivatives of v and ρ with respect to temperature (T) and salinity (S) at a given T (12°C), S (35.4) and pressure (P, 1000 dbar) to determine the relative contribution of T and S to impedance contrasts. For these particular T, S, P values, they found that the contribution of T is almost five-fold that of S. There has however been no formal attempt to date to generalize these conclusions by calculating the complete expressions of the partial derivatives, which significantly change with T, S, and P, and apply them to a real oceanographic data set in order to determine

[1]Unitat de Tecnologia Marina, Consejo Superior de Investigaciones Científicas, Barcelona, Spain.
[2]Institut of Earth Sciences ''Jaume Almera,'' Consejo Superior de Investigaciones Científicas, Barcelona, Spain.
[3]Institut de Ciencies del Mar, Consejo Superior de Investigaciones Científicas, Barcelona, Spain.

0094-8276/09/2009GL040187$05.00

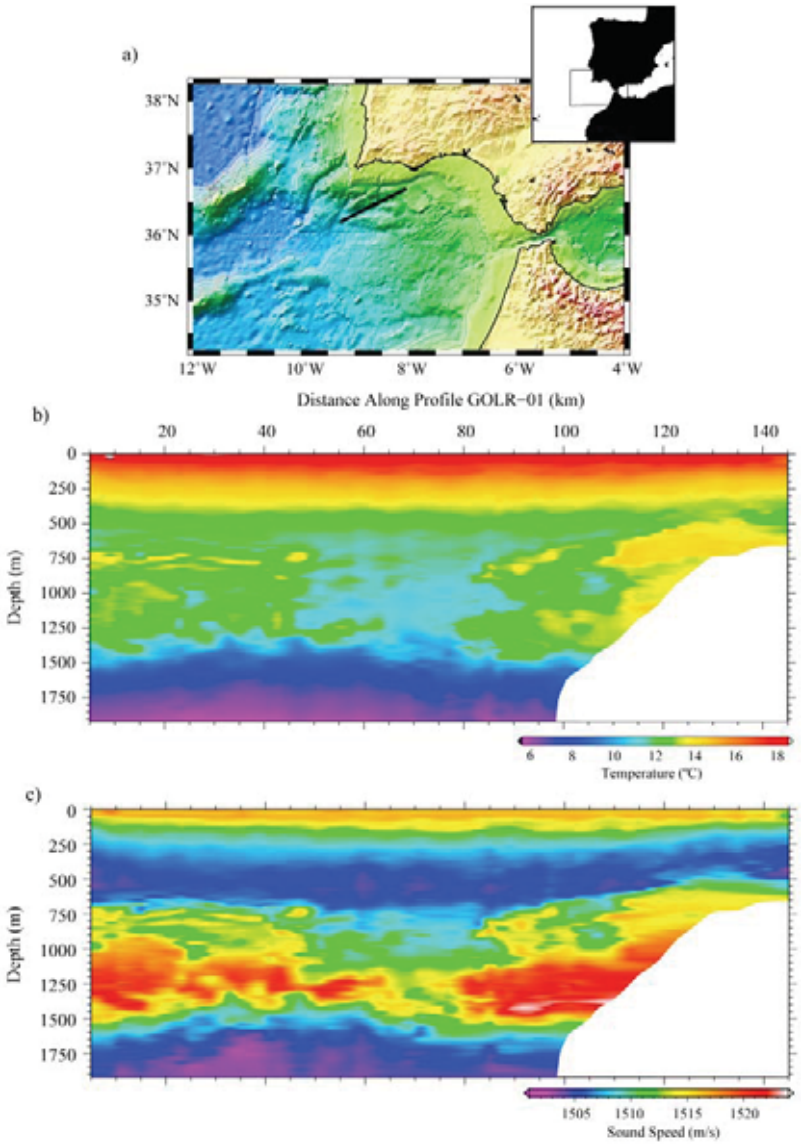

Figure 1. (a) Location map of the D318B-GO survey study zone. The thick line indicates the location of the coincident seismic and hydrographic profile GO-LR-01. (b) 2-D temperature-depth map obtained from XBT and CTD data acquired during the D318-GO survey along the profile GO-LR-01. The data have been interpolated for imaging purposes using the minimum curvature surface algorithm of *Smith and Wessel* [1990]. (c) 2-D sound speed-depth map along the same profile obtained using *Chen and Millero*'s [1976] empirical relationship. The temperature is that measured with XBT and CTD (Figure 2a) and the salinity has been inferred based on CTD data.

the actual range of variation of the different contributions. This is what we do in this work: we first calculate the partial derivatives of sound speed and density with respect to T and S based on UNESCO formulas [*Chen and Millero*, 1976; *Millero et al.*, 1980], then incorporate the expressions into linearized Zoeppritz equations of reflection coefficients [*Aki and Richards*, 1980], and finally apply the resulting expressions to real, high-resolution, T and S data recently acquired in the Gulf of Cadiz [*Hobbs et al.*, 2007].

2. Data

[5] The hydrographic data used in this study were collected in April, 2007 during the coincident seismic and oceanographic NERC-318B survey made on-board British RRS Discovery and German FS Poseidon in the SW Iberian margin, as part of the EU project "Geophysical Oceanography: A new tool to understand the thermal structure and dynamics of oceans (GO)" [*Hobbs et al.*, 2007]. During the survey, 1200 km of MCS lines and coincident, high-resolution XBT and XCTD stations were acquired by RRS Discovery, while simultaneous XBT and CTD casts were made by FS Poseidon [*Hobbs et al.*, 2007]. XBT-profiles were quality controlled, and anomalous data were removed. Depth was corrected according to the fall-rate equations of *Boyd and Linzell* [1993] for Sippican T-5. The error in depth with respect to adjoining CTDs was typically less than 5 m over the 1800 m depth range. From among the available hydrographic data, we have selected those acquired along profile GO-LR-01 (Figure 1a). It is 145 km-long and runs

NE–SW offshore Portimao crossing the core of the Mediterranean Undercurrent, which transports Mediterranean water (MW) west from the Strait of Gibraltar as it sinks along the continental slope of the Iberian margin. Figure 1b shows the 2D temperature map obtained by merging together all the XBT and CTD data (49 and 5 profiles, respectively) acquired along line GO-LR-01. The mean separation between adjoining casts is ~2.5 km.

[6] Simultaneous temperature and salinity values, measured during the whole GO survey (40 in total) have been used to assign S-values to the XBT-derived T, depth (z) pairs. The corresponding S-values have been calculated following a statistical approach that consisted of: 1) computing all the CTD-measured T, z (and S) values that fall within ΔT, Δz of each XBT-measured T, z pair; and 2) assigning S to XBT-measured T, z pairs as a Gaussian-weighted average of all the selected CTD-measured S values. We have tested different values for ΔT, Δz as well as for the Gaussian's standard deviations σ_T and σ_z, and found that a set of parameters giving a good compromise between data accuracy and data density are $\Delta T = 0.02°C$, $\sigma_T = 0.002°C$, and $\Delta z = 5$ m, $\sigma_z = 0.5$ m. The accuracy was evaluated by comparing the salinity obtained with that measured with a CTD cast made during the GO survey but not used in the assignment. The mean difference obtained is less than 1.5×10^{-3}.

[7] The locally measured temperature and pressure values, together with the statistically inferred salinities, have been used to calculate density and sound speed. Density has been computed using the empirical UNESCO's International Equation of Seawater from 1980 (EOS80), which is claimed to be valid for S = 0–42, T = −2–40°C, and P = 0–1000 bars. Details on the fitting procedure and the different terms of the polynomial regressions are available from *Millero et al.* [1980]. Sound speed (Figure 1c) has been calculated using the empirical relationship of *Chen and Millero* [1976], which is also compliant with the practical salinity scale and is the one giving the best agreement with values computed from EOS80. The temperature and sound speed maps of Figures 1b and 1c clearly show the presence of the relatively warm, salty and fast MW mass between 700 m and 1500 m depth along the whole profile.

3. Method

[8] The strategy to estimate the relative contribution of sound speed vs. density and temperature vs. salinity on reflectivity at the seismic source wavelength consists of three main steps, namely (1) the computation of the T and S partial derivatives using the UNESCO formulas for density and sound speed on a scale one order of magnitude smaller to the source wavelength, (2) the incorporation of the resulting expressions into the Zoeppritz equations for the reflection coefficients, (3) the calculation of the relative significance of the different properties to the reflection coefficients along the hydrographic profile shown in Figure 1a, and (4) the convolution with the source wavelet.

[9] There are many works dealing with the Zoeppritz equations for the transmission/reflection coefficients of plane waves in layered media. Since Zoeppritz equations are highly nonlinear with respect to speed and density, many approximations have been attempted in order to linearize them. Here we follow that proposed by *Aki and Richards* [1980], which is suitable for elastic media having weak property contrasts. When the two adjoining layers have similar properties; that is, if there is, over a vertical distance Δz, a jump in magnitudes of $\Delta\rho = \rho_2 - \rho_1$, $\Delta\alpha = \alpha_2 - \alpha_1$ and $\Delta\beta = \beta_2 - \beta_1$ that is very small so the ratios $\Delta\rho/\rho$, $\Delta\alpha/\alpha$, and $\Delta\beta/\beta$ (where ρ, α, and β are the mean value of density, compressional, and shear waves speed of the two media) are much lower than unity, then transmission will largely dominate reflection (i.e., the reflection coefficient, R, will be close to zero). In this case it makes sense to derive the first-order effect of small jumps in density and sound speed because the resulting expressions are remarkably accurate [e.g., *Aki and Richards*, 1980] and, at the same time, give good insight into the separate contributions made by $\Delta\alpha$, $\Delta\beta$ and $\Delta\rho$. For acoustic media such as the water column, where $\beta = 0$, $\Delta\alpha/\alpha$ is on the order of 10^{-3}–10^{-4}, and $\Delta\rho/\rho$ is even smaller, the resulting expression for the reflection coefficient depend on the angle of incidence (i) and the density and sound speed (v) contrasts only. It is given as $R = R_v + R_\rho$, where

$$R_v = \frac{\Delta v}{2v \cdot \cos^2 i} \tag{1}$$

and

$$R_\rho = \frac{\Delta\rho}{2\rho} \tag{2}$$

correspond respectively to the contribution to R made by Δv and $\Delta\rho$. The relative contribution of $\Delta\rho$ and Δv to R is then calculated as R_v/R and R_ρ/R.

[10] Without considering the effect of pressure variations, $\Delta\rho$ and Δv can be expressed as a function of the temperature and salinity variations, ΔT and ΔS, as

$$\Delta\rho_{TS} \cong \frac{\partial\rho}{\partial T}\Delta T + \frac{\partial\rho}{\partial S}\Delta S \tag{3}$$

and

$$\Delta v_{TS} \cong \frac{\partial v}{\partial T}\Delta T + \frac{\partial v}{\partial S}\Delta S \tag{4}$$

where $\partial\rho/\partial$T, $\partial\rho/\partial$S, ∂v/∂T, ∂v/∂S are the partial derivatives of density and sound speed with respect to T and S. Combining (1), (2), (3) and (4) we obtain $R_{TS} = R_T + R_S$, where

$$R_T = \frac{\Delta T}{2} \cdot \left[\frac{\partial\rho/\partial T}{\rho} + \frac{\partial v/\partial T}{v \cdot \cos^2 i}\right] \tag{5}$$

and

$$R_S = \frac{\Delta S}{2} \cdot \left[\frac{\partial\rho/\partial S}{\rho} + \frac{\partial v/\partial S}{v \cdot \cos^2 i}\right] \tag{6}$$

correspond to the contribution to the reflection coefficient made by ΔT and ΔS, respectively. We can then estimate the relative contribution of ΔT and ΔS as R_T/R_{TS} and R_S/R_{TS} (R_T/R and R_S/R from here on).

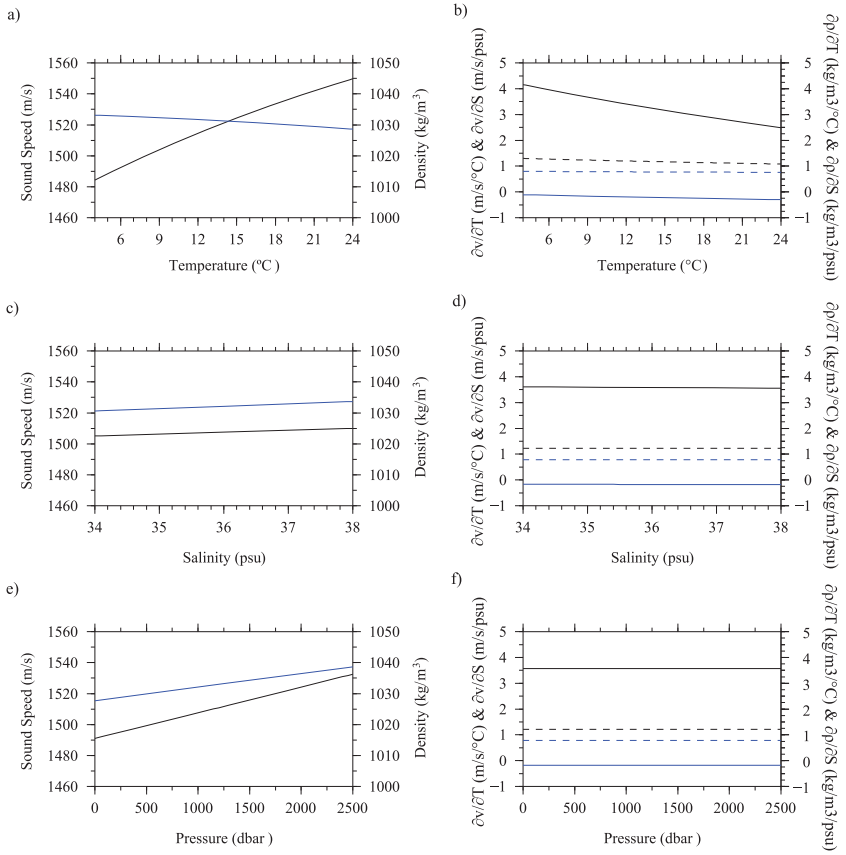

Figure 2. Diagrams of physical properties and their T, S partial derivatives obtained using the EOS80 expressions for sound speed and density. Sound speed (black line) and density (blue line) vs. (a) temperature, (c) salinity and (e) pressure. $\partial v/\partial T$ (solid black line), $\partial v/\partial S$ (dashed black line), $\partial \rho/\partial T$ (solid blue line), $\partial \rho/\partial S$ (dashed blue line) vs. (b) temperature, (d) salinity and (f) pressure.

[11] Figure 2 shows diagrams of v, ρ and their T and S partial derivatives as a function of T, S and P calculated with the EOS80 relationships referred to above. Note that sound speed increases with increasing T, S and P, whereas density increases with increasing S and P but decreases with increasing T. Regarding the partial derivatives, $\partial v/\partial T$ decreases substantially with increasing T and very slightly with increasing S, whereas $\partial \rho/\partial T$ decreases with increasing T and S. Both $\partial v/\partial S$ and $\partial \rho/\partial S$ decrease slightly with increasing T and hardly vary with S.

[12] R_v, R_ρ and R_T, R_S have been computed for all XBTs using the v, ρ, $\partial v/\partial T$, $\partial v/\partial S$, $\partial \rho/\partial T$, $\partial \rho/\partial S$ values obtained along the whole profile and calculating Δv, $\Delta \rho$, ΔT, ΔS as a sample-by-sample difference from top to bottom of each profile, which corresponds to a vertical distance of Δz = 65 cm. The resulting values are then convolved with a Ricker wavelet of 50 Hz, adequate to characterize fine structure. Given that temperature and salinity are highly correlated, the relative T, S contribution is basically independent of the vertical smoothing made in the range of 25–50 Hz.

4. Discussion of Results

[13] The results obtained for R_v/R, R_ρ/R and R_T/R, R_S/R along profile GO-LR-01, expressed as a percentage of the relative contribution for normal incidence after convolution with the source wavelet, are shown in Figure 3. It is clear that the mean contribution to the water reflectivity comes, as expected, from Δv through ΔT, in agreement with previous works confirming that the influence of Δv and ΔT is major compared to $\Delta \rho$ and ΔS [e.g., *Nandi et al.*, 2004; *Krahmann et al.*, 2008]. On one hand, the mean value of R_v/R along GO-LR-01 is 90%, whereas R_ρ/R accounts for the remaining 10%. The standard deviation of both R_v and R_ρ is 11%. These values agree with those estimated by *Krahmann et al.* [2008] based on waveform analysis of XBT data in the same area (~90%), and are smaller to those proposed by *Ruddick et al.* [2009] using the expressions derived by *Lavery et al.* [2003] for scattering of high-frequency acoustic waves at constant T, P and S (~99%). In the case of non-normal incidence, the contribution of Δv increases by a factor of $1/\cos^2 i$ and that of $\Delta \rho$ remains constant. On the other hand, the mean value of R_T/R is 80%, while that of R_S/R is 20%, with a standard deviation of 12%. R_S/R is somewhat larger than that estimated by *Ruddick et al.* [2009] (17%). Overall these results illustrate that while R_ρ/R is, on average, one-to-two orders of magnitude smaller than R_v/R, and it could thus be safely neglected when inferring sound speed from seismic data, R_S/R is only four-fold weaker than R_T/R, so it should not be ignored. Given that $\partial v/\partial T$ is two- to four-fold larger than $\partial v/\partial S$, the influence of non-normal incidence to R_S/R is smaller than to R_T/R, so the relative contribution of S decreases with

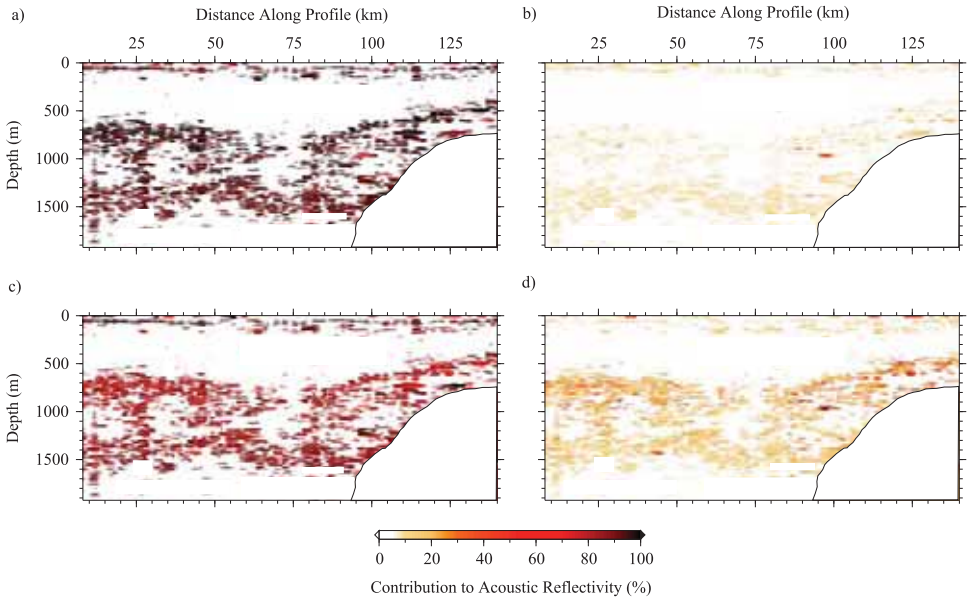

Figure 3. 2-D maps representing the percentage of the partial contribution of (a) sound speed (R_v/R) vs. (b) density (R_ρ/R), and (c) temperature (R_T/R) vs. (d) salinity (R_S/R) to the reflectivity of the water column along profile GO-LR-01 (Figure 1). These maps have been obtained convolving the reflection coefficients with a 50 Hz Ricker wavelet. In order to concentrate the information on the brightest reflectors, only points exceeding the mean R value are displayed. As in Figure 1, data interpolation has been made using the minimum curvature surface algorithm of *Smith and Wessel* [1990].

increasing i. It is interesting to note, however, that the relative contribution of the different properties strongly varies within the water column along the whole profile (Figure 3). The highest R_S/R (and lowest R_T/R) is systematically found at the top of the MW (i.e., 700–900 m deep), whereas the lowest R_S/R (and highest R_T/R) is found at the bottom of the MW (i.e., 1200–1400 m deep). R_S/R is 27% on average, and locally achieves 35–40% at the top of the MW. At the bottom of the MW, R_S/R is 16% on average. The contribution of salinity to seismic reflectivity is therefore considerably larger at the top than at the bottom of the MW. This large R_T/R, R_S/R variability prevents one from univocally determining T and S based on seismic data alone. R_v/R and R_ρ/R show a trend similar to that of R_S/R and R_T/R, in being that the mean R_ρ/R value is two-times larger at the bottom (12%) than at the top (6%) of the MW.

[14] It is noteworthy that the regions showing the largest contribution of salinity contrasts to reflectivity are found in areas of unstable temperature gradients, with dominant thermal flux and prone to mixing by diffusive convection such as the top of the MW, whereas the smallest salinity (and largest density) contribution occurs in places of unstable salt gradients, presumed to be dominated by salt fingering, such as the bottom of the MW [*Schmitt*, 1994].

5. Conclusions

[15] Marine MCS systems are well-adapted to image oceanic fine-structure. The strength of the reflectivity associated with a given water boundary layer is proportional to the acoustic impedance contrast between the two neighbouring water masses, which is in turn a function of sound speed and density (i.e., temperature and salinity) changes across the layer at the seismic source frequency bandwidth. The main contribution to seismic reflectivity is that of sound speed variations, which is, on average, one-to-two-orders of magnitude larger than that of density (90–95% vs. 5–10%). Likewise, temperature contrasts account on average for ~80% of the reflectivity, and salinity for the remaining ~20%. The partial contribution of the different properties is however highly variable. Interestingly, salinity contribution can be as high as 40% in the top of MW features, but only around 15% in other regions such as at the base of the MW. This variability makes it virtually impossible to derive temperature and salinity from seismic data alone. In the region under study, the areas showing the largest salinity contribution correspond to areas prone to diffusive convection such as at the top of MW features, whereas those showing the smallest salinity contribution are those prone to salt fingering.

[16] **Acknowledgments.** This work is part of the EU-FP6 funded GO project (NEST-2003-1 FP6015603), and the data set used here was acquired in the framework of this project. It has also been supported by the Consejo Superior de Investigaciones Científicas (CSIC) through GEOCEAN PIF Project 200530f081. CSIC is also funding the second author's work by means of a JaeDoc contract. Constructive reviews made by R. Hobbs and two anonymous reviewers are acknowledged.

References

Aki, K., and P. G. Richards (1980), *Quantitative Seismology: Theory and Methods*, W. H. Freeman, San Francisco, Calif.

Biescas, B., V. Sallarès, J. L. Pelegrí, F. Machín, R. Carbonell, G. Buffett, J. J. Dañobeitia, and A. Calahorrano (2008), Imaging meddy fine structure using multichannel seismic data, *Geophys. Res. Lett.*, *35*, L11609, doi:10.1029/2008GL033971.

Boyd, J. D., and R. S. Linzell (1993), The temperature and depth accuracy of Sippican T-5 XBTs, *J. Atmos. Oceanic Technol.*, *10*, 128–136, doi:10.1175/1520-0426(1993)010<0128:TTADAO>2.0.CO;2.

Buffett, G., B. Biescas, J. L. Pelegrí, F. Machín, V. Sallarès, R. Carbonell, D. Klaeschen, and R. Hobbs (2009), Seismic reflection along the path of the Mediterranean Undercurrent, *Cont. Shelf Res.*, *29*, 1848–1860, doi:10.1016/j.csr.2009.05.017.

Chen, C. T., and F. J. Millero (1976), Speed of sound in seawater at high pressures, *J. Acoust. Soc. Am.*, *60*, 1270–1273, doi:10.1121/1.381240.

Hobbs, R., et al. (2007), GO—Geophysical Oceanography: A new tool to understand the thermal structure and dynamics of oceans, *D318 Cruise Rep.*, Durham Univ., Durham, U. K. (Available at http://www.dur.ac.uk/eu.go/cruise/report.html)

Holbrook, W. S., and I. Fer (2005), Ocean internal wave spectra inferred from seismic reflection transects, *Geophys. Res. Lett.*, *32*, L15604, doi:10.1029/2005GL023733.

Holbrook, W. S., P. Paramo, S. Pearse, and R. W. Schmitt (2003), Thermohaline fine structure in an oceanographic front from seismic reflection profiling, *Science*, *301*, 821–824, doi:10.1126/science.1085116.

Krahmann, G., P. Brandt, D. Klaeschen, and T. Reston (2008), Mid-depth internal wave energy off the Iberian Peninsula estimated from seismic reflection data, *J. Geophys. Res.*, *113*, C12016, doi:10.1029/2007JC004678.

Lavery, A., R. W. Schmitt, and T. K. Stanton (2003), High-frequency acoustic scattering from turbulent oceanic microstructure: The importance of density fluctuations, *J. Acoust. Soc. Am.*, *114*, 2685–2697.

Millero, F. J., C. T. Chen, A. Bradshaw, and K. Schleicher (1980), A new high pressure equation of state for seawater, *Deep Sea Res., Part A*, *27*, 255–264, doi:10.1016/0198-0149(80)90016-3.

Nakamura, Y., T. Noguchi, T. Tsuji, S. Itoh, H. Niino, and T. Matsuoka (2006), Simultaneous seismic reflection and physical oceanographic observations of oceanic fine structure in the Kuroshio extension front, *Geophys. Res. Lett.*, *33*, L23605, doi:10.1029/2006GL027437.

Nandi, P., S. Holbrook, S. Pearse, P. Paramo, and R. Schmitt (2004), Seismic reflection imaging of water mass boundaries in the Norwegian Sea, *Geophys. Res. Lett.*, *31*, L23311, doi:10.1029/2004GL021325.

Ruddick, B., and A. Gargett (2003), Oceanic double-diffusion: Introduction, *Prog. Oceanogr.*, *56*, 381–393, doi:10.1016/S0079-6611(03)00024-7.

Ruddick, B., H. Song, C. Dong, and L. Pinheiro (2009), Water column seismic images as maps of temperature gradient, *Oceanography*, *22*, 192–205.

Schmitt, R. W. (1994), Double diffusion in oceanography, *Annu. Rev. Fluid Mech.*, *26*, 255–285, doi:10.1146/annurev.fl.26.010194.001351.

Sheriff, R. E., and L. P. Geldart (1995), *Exploration Seismology*, 2nd ed., 592 pp., Cambridge Univ. Press, Cambridge, U. K.

Smith, W. H. F., and P. Wessel (1990), Gridding with continuous curvature splines in tension, *Geophysics*, *55*, 293–305, doi:10.1190/1.1442837.

Tsuji, T., T. Noguchi, H. Niino, T. Matsuoka, Y. Nakamura, H. Tokuyama, S. Kuramoto, and N. Bangs (2005), Two-dimensional mapping of fine structures in the Kuroshio Current using seismic reflection data, *Geophys. Res. Lett.*, *32*, L14609, doi:10.1029/2005GL023095.

Widess, M. (1973), How thin is a thin bed?, *Geophysics*, *38*, 1176–1180, doi:10.1190/1.1440403.

B. Biescas, J. J. Dañobeitia, and V. Sallarès, Unitat de Tecnologia Marina, Consejo Superior de Investigaciones Científicas, Passeig Marítim de la Barceloneta, 37-49, E-08003 Barcelona, Spain. (vsallares@cmima.csic.es)

G. Buffett and R. Carbonell, Institut of Earth Sciences "Jaume Almera," Consejo Superior de Investigaciones Científicas, Lluis Solé i Sabarís, s/n, E-08028 Barcelona, Spain.

J. L. Pelegrí, Institut de Ciencies del Mar, Consejo Superior de Investigaciones Científicas, Passeig Marítim de la Barceloneta, 37-49, E-08003 Barcelona, Spain.